

STARQUAKES, HEATING ANOMALIES, AND NUCLEAR REACTIONS IN THE
NEUTRON STAR CRUST

By

Alex Thomas Deibel

A DISSERTATION

Submitted to
Michigan State University
in partial fulfillment of the requirements
for the degree of

Astrophysics and Astronomy — Doctor of Philosophy

2017

ABSTRACT

STARQUAKES, HEATING ANOMALIES, AND NUCLEAR REACTIONS IN THE NEUTRON STAR CRUST

By

Alex Thomas Deibel

When the most massive stars perish, their cores may remain intact in the form of extremely dense and compact stars. These stellar remnants, called *neutron stars*, are on the cusp of becoming black holes and reach mass densities greater than an atomic nucleus in their centers. Although the interiors of neutron stars were difficult to investigate at the time of their discovery, the advent of modern space-based telescopes (e.g., *Chandra* X-ray Observatory) has pushed our understanding of the neutron star interior into exciting new realms. It has been shown that the neutron star interior spans an enormous range of densities and contains many phases of matter, and further theoretical progress must rely on numerical calculations of neutron star phenomena built with detailed nuclear physics input.

To further investigate the properties of the neutron star interior, this dissertation constructs numerical models of neutron stars, applies models to various observations of neutron star high-energy phenomena, and draws new conclusions about the neutron star interior from these analyses. In particular, we model the neutron star's outermost ≈ 1 km that encompasses the neutron star's envelope, ocean, and crust. The model must implement detailed nuclear physics to properly simulate the hydrostatic and thermal structure of the neutron star. We then apply our model to phenomena that occur in these layers, such as: thermonuclear bursts in the envelope, *g*-modes in the ocean, torsional oscillations of the crust, and crust cooling of neutron star transients.

A comparison of models to observations provides new insights on the properties of dense matter that are often difficult to probe through terrestrial experiments. For example, models of the

quiescent cooling of neutron stars, such as the accreting transient MAXI J0556-332, at late times into quiescence probe the thermal transport properties of the deep neutron star crust. This modeling provides independent data from astronomical observations on the nature of neutron superfluidity and the thermal conductivity of nuclear pasta.

Our neutron star modeling efforts also pose new questions. For instance, reaction networks find that neutrino emission from cycling nuclear reactions is present in the neutron star ocean and crust, and potentially cools an accreting neutron star. This is a theory we attempt to verify using observations of neutron star transients and thermonuclear bursts, although it remains unclear if this cooling occurs. Furthermore, on some accreting neutron stars, more heat than supplied by nuclear reactions is needed to explain their high temperatures at the outset of quiescence. Although the presence of heating anomalies seems common, the source of extra heating is difficult to determine.

To Carol

ACKNOWLEDGMENTS

Throughout my journey to become an astrophysicist many people have inspired me and have generously given me their time. I would like to thank my undergraduate research advisor Monica Valluri, who patiently guided me through my first research project and sparked my interest in numerical models. It is a pleasure to thank Andrew W. Steiner for being my research mentor early in my graduate career as we navigated the complicated landscape of the magnetar interior. I am especially grateful for the guidance and encouragement of my doctoral supervisor Edward F. Brown, which has been vital to my success.

There are many others I would like to thank that over the course of my graduate career have offered their guidance, support, and collaboration. I thank Andrew Cumming for his collaboration on neutron star thermal evolution and superburst ignition models. I thank Hendrik Schatz and Zach Meisel for expanding my knowledge of nuclear physics. I thank Sanjay Reddy and Bob Rutledge for useful advice. I thank Dany Page and Duncan Galloway for their invitations to the International Space Science Institute teams on neutron stars. I also thank the International Space Science Institute for supporting me as a young scientist at their international meetings. I also thank the Joint Institute for Nuclear Astrophysics Center for the Evolution of the Elements whose support allowed me to present my research around the world. I would like to thank members of my guidance committee: Laura Chomiuk, Sean Couch, and Jim Linnemann, for their perspective and guidance.

During the course of my research for this dissertation I received support from the National Aeronautics and Space Administration through Chandra Award Number TM5-16003X issued by the *Chandra X-ray Observatory* Center, which is operated by the Smithsonian Astrophysical Observatory for and on behalf of the National Aeronautics and Space Administration under contract

NAS8-03060. Much of this work was supported by the National Science Foundation under grant No. PHY-1430152 (Joint Institute for Nuclear Astrophysics - Center for the Evolution of the Elements) and grant No. AST-1516969. I also received support from the Michigan State University College of Nature Science Dissertation Completion Fellowship.

TABLE OF CONTENTS

LIST OF TABLES	ix
LIST OF FIGURES	x
Chapter 1 Introduction	1
Chapter 2 The Neutron Star Ocean and Crust	7
2.1 Structure	7
2.2 Low-density Equation of State	11
2.2.1 Nuclei and the Ion-lattice	12
2.2.2 Quasi-free Neutrons	15
2.3 Composition	16
2.3.1 Equilibrium	16
2.3.2 Accreted	17
2.4 Thermal Transport	20
2.4.1 Outer Crust	21
2.4.2 Inner Crust	24
2.4.3 Heat Sources and Sinks	30
Chapter 3 Magnetar Starquakes	32
3.1 A Magnetized Crust	33
3.1.1 Electron Quantization	33
3.1.2 Composition	35
3.2 Crust Torsional Modes	37
3.3 Constraints from Observations	42
3.3.1 Nuclear Symmetry Energy	42
3.3.2 Neutron Entrainment	45
3.3.3 Crust-core Transition Depth	49
3.3.4 Crust Magnetic Field	49
Chapter 4 Neutron Star Transient Thermal Evolution	52
4.1 A Cooling Slab	53
4.2 Realistic Cooling Models	55
4.2.1 Heating Anomalies in MAXI J0556-332	58
4.2.2 The Reflare in MAXI J0556-332	64
4.3 Observational Tests for Ocean g -modes	66
4.3.1 Neutron Star Ocean Thermal Evolution	69
4.3.2 g -mode Spectrum of the Neutron Star Ocean	72
4.4 Late Time Cooling and Nuclear Pasta	78

Chapter 5	Urca Cooling Nuclei Pairs	85
5.1	Urca Pair Formation	86
5.2	Crust Urca Pairs	89
5.2.1	Impact on Neutron Star Transients	90
5.2.2	Impact on Neutron Star Superbursts	92
5.3	Ocean Urca Pairs	99
5.3.1	Observational Signatures	103
Chapter 6	Conclusion	110
APPENDICES		114
	Appendix A: Local Stability of Non-equilibrium Nuclear Reactions	115
	Appendix B: Thermal Diffusion	117
	Appendix C: Axial Perturbations	120
REFERENCES		122

LIST OF TABLES

Table 2.1:	Parameters of the mass model.	15
Table 3.1:	Equilibrium nuclei below the crust-core transition in a magnetized crust. .	36
Table 5.1:	Urca pairs in the neutron star crust (Schatz et al., 2014).	90
Table 5.2:	Properties of the strongest Urca e^- -capture parents identified in Meisel & Deibel (2017) and in Schatz et al. (2014), absent even- A nuclides, excluded by Meisel et al. (2015); Deibel et al. (2016).	96
Table 5.3:	Urca pairs active in the neutron star ocean.	102

LIST OF FIGURES

Figure 2.1:	Schematic of a neutron star’s structure. Degenerate electrons provide the primary pressure support in the outer crust and overlying layers. In the inner crust, the dripped neutrons begin providing the primary pressure support.	9
Figure 2.2:	Ocean-crust transition density as a function of temperature for a neutron star with $g_{14} = 1.85$ and using the crust equation of state from Haensel & Zdunik (1990).	10
Figure 2.3:	Equilibrium crust composition in the neutron star for the SLy4 crust equation of state. The panels are (a) the crust composition without shell corrections and (b) the crust composition with shell corrections. The shell correction to the binding energy is shown in Equation (2.14). This figure is reproduced from Deibel et al. (2014).	18
Figure 2.4:	Nuclear landscape in the inner crust at $\rho = 6 \times 10^{12} \text{ g cm}^{-3}$. Black squares indicate locally stable nuclei that satisfy the stability condition in Equation 2.24. Nuclei are colored according to the binding energy per nucleon.	20
Figure 2.5:	Nuclear landscape in the inner crust at $\rho = 2 \times 10^{13} \text{ g cm}^{-3}$. Black squares indicate locally stable nuclei that satisfy the stability condition in Equation 2.24. Nuclei are colored according to the binding energy per nucleon.	21
Figure 2.6:	Superfluid critical temperature models for the neutron star inner crust as function of mass density. The three solid gray curves are from Gandolfi et al. (2008). The solid black curve is from Schwenk et al. (2003). The dashed black curve is from Gezerlis & Carlson (2011). The red curve is from Chen et al. (1993). The blue curve is from Wambach et al. (1993).	25
Figure 3.1:	Equilibrium composition of the neutron star crust in a strong magnetic field $B = 2 \times 10^{15} \text{ G}$. (<i>Left panel</i>): Equilibrium crust composition without a magnetic field. (<i>Right panel</i>): The black arrow indicates the first transition between equilibrium nuclei, which has moved to a greater depth as a consequence of the strong magnetic field when compared to the left panel.	37
Figure 3.2:	Schematic of a torsional oscillation mode in the magnetar crust. Crust oscillation frequencies are found using Equation 3.14, using the boundary condition $\xi' = 0$ (loss of traction) at the base and top of the crust.	38

Figure 3.3:	Alfvén velocity (blue curve) and shear velocity (black curve) in the crust as a function of mass density. The composition is that of a $1.4 M_{\odot}$ neutron star using the SLy4 crust EOS.	40
Figure 3.4:	Frequency of the fundamental $l = 2$ mode as a function of the magnetar mass for the core EOS probability distribution (centroid and $\pm 2\sigma$) from Steiner et al. (2013) and an SLy4 crust EOS. The dashed black line indicates the observed 29 Hz QPO of SGR 1806-20. The frequencies are evaluated for a crust-core transition density of 0.12 fm^{-3} with $B = 0 \text{ G}$	41
Figure 3.5:	Magnetar mass as a function of radius for the core EOS probability distribution from Steiner et al. (2013). Frequencies are evaluated using the SLy4 crust EOS ($L = 46 \text{ MeV}$) for $n_t = 0.12 \text{ fm}^{-3}$. The thick red solid line indicates masses and radii for which the fundamental mode has a frequency of 29 Hz in the case of SLy4 and 18 Hz in the case of Rs. The black short-dashed line indicates masses and radii for a 626 Hz harmonic mode and $B = 0 \text{ G}$. Masses and radii from 626 Hz harmonic modes with magnetized crusts are labeled accordingly. Arrows indicate masses and radii that match both the fundamental and the harmonic modes for the field-free case and the case with the magnetic field of SGR 1806-20 ($B = 2.4 \times 10^{15} \text{ G}$).	43
Figure 3.6:	Magnetar mass as a function of radius for the core EOS probability distribution from Steiner et al. (2013). Frequencies are evaluated using the Rs crust EOS ($L = 86 \text{ MeV}$) for $n_t = 0.12 \text{ fm}^{-3}$. The thick red solid line indicates masses and radii for which the fundamental mode has a frequency of 29 Hz in the case of SLy4 and 18 Hz in the case of Rs. The black short-dashed line indicates masses and radii for a 626 Hz harmonic mode and $B = 0 \text{ G}$. Masses and radii from 626 Hz harmonic modes with magnetized crusts are labeled accordingly. Arrows indicate masses and radii that match both the fundamental and the harmonic modes for the field-free case and the case with the magnetic field of SGR 1806-20 ($B = 2.4 \times 10^{15} \text{ G}$).	44
Figure 3.7:	Magnetar mass as a function of radius for EOS probability distribution from Steiner et al. (2013). Frequencies are evaluated using the SLy4 crust EOS with $B = 0 \text{ G}$ and $n_t = 0.12 \text{ fm}^{-3}$. The red dot-dashed, blue dotted, and black dashed lines indicate masses and radii from fundamental modes of frequency 29 Hz for different free neutron entrainment fractions f_{ent} . The shaded band indicates masses and radii from 626 Hz harmonic modes as f_{ent} is varied from 0.50 to 1.0. Arrows indicate the masses and radii that match both the fundamental and the harmonic modes for $f_{\text{ent}} = 1.0, 0.75,$ and 0.50	47

Figure 3.8:	The same as Fig. 3.7, but for the Rs crust EOS with $B = 0$ G. Here the free neutron entrainment fraction f_{ent} is varied from 0.20 to 0.30, with f_{ent} labeled next to the corresponding curves. The red dot-dashed, blue dotted, and black dashed lines indicate masses and radii from the 29 Hz fundamental mode. The shaded band indicates masses and radii from the 626 Hz harmonic mode. Arrows indicate the masses and radii for $f_{\text{ent}} = 0.30, 0.25,$ and 0.20 that match both the fundamental and harmonic modes.	48
Figure 3.9:	The same as Fig. 3.5, but for the SLy4 crust EOS with $n_t = 0.08 \text{ fm}^{-3}$. The thick red solid line indicates masses and radii determined from a fundamental mode of 29 Hz. Masses and radii from harmonic modes with magnetized crusts are labeled accordingly. Arrows indicate masses and radii that match both the fundamental and the harmonic modes for the field-free case and the case with the magnetic field of SGR 1806-20 ($B = 2.4 \times 10^{15}$ G).	50
Figure 4.1:	Quiescent light curve of the neutron star MXB 1659-29. The model uses a neutron star mass of $M = 1.6 M_{\odot}$, a neutron star radius of $R = 11.2$ km, a shallow heat source of $Q_{\text{shallow}} = 1.0$ MeV per accreted nucleon, and a core temperature of $T_{\text{core}} = 4 \times 10^7$ K. The model also uses an impurity parameter of $Q_{\text{imp}} = 2.5$ for the entire crust as done in Brown & Cumming (2009).	56
Figure 4.2:	Location of the ocean-crust transition as a function of temperature at the base of the ocean. The black solid curve is for the one-component accreted composition (Haensel & Zdunik, 1990) and the black dotted curve is for a multi-component accreted composition (Steiner, 2012). The crystallization density is given by Equation (2).	57
Figure 4.3:	Quiescent lightcurve of the neutron star MAXI J0556-332. The solid black curve corresponds to a model with $M = 1.5 M_{\odot}$, $R = 11$ km, $Q_{\text{shallow}} = 6.0$ MeV, and $T_{\text{core}} = 10^8$ K; the dashed black curve is for the same model with $T_{\text{core}} = 3 \times 10^7$ K. The black dotted curves are light curves with a reheating event ≈ 170 days into quiescence for $Q_{\text{shallow}} = 6.0$ MeV (upper curve) and $Q_{\text{shallow}} = 3.0$ MeV (lower curve). The blue dashed curve is for a $M = 2.1 M_{\odot}$, $R = 12$ km neutron star fit to the observations by changing the shallow heating depth and strength. The data above the light curve are contamination from residual accretion. Note that $T_{\text{eff}}^{\infty} \propto g^{1/4}/(1+z)$ which leads to different observed core temperatures for different gravities.	60
Figure 4.4:	Schematic of the neutron star's outer layers and the location of the anomalous shallow heating in MAXI J0556-332.	61

Figure 4.5:	<p>Quiescent temperature evolution of the neutron star MAXI J0556-332. Solid black curves indicate the evolution of the crust temperature during quiescence for the $M = 1.5 M_{\odot}$ and $R = 11$ km model, shown in Figure 4.3. The red dotted curve is the melting line of the crust ($\Gamma = 175$) for the crust composition in Haensel & Zdunik (1990), the black dotted curve is the transition from an electron-dominated heat capacity to an ion-dominated heat capacity ($C_V^e = C_V^{\text{ion}}$), and the blue dotted curve is where the local neutrino cooling time is equal to the thermal diffusion time ($\tau_{\nu} = \tau_{\text{therm}}$). The gray dashed curve shows the lattice Debye temperature Θ_D; when $T \ll \Theta_D$ electron-impurity scattering influences the thermal conductivity.</p>	63
Figure 4.6:	<p>Markov chain Monte Carlo fits to the quiescent light curve of MAXI J0556-332 using the crust relaxation code <i>crustcool</i>. The contours show the isodensity surfaces of the likelihood \mathcal{L}, corresponding to $\sqrt{-2\ln\mathcal{L}} = 0.5, 1, 1.5, 2$, for the neutron star mass M, radius R, pressure at the shallow heating depth P_h, and the shallow heating strength Q_{shallow}.</p>	65
Figure 4.7:	<p>Schematic of the neutron star’s outer layers and the location of g-modes.</p>	68
Figure 4.8:	<p>Thermal evolution as a function of time during outburst/quiescence for MAXI J0556-332 (solid curves), MXB 1659-29 (dashed curves), and XTE J1701-462 (dot-dashed curves). <i>Panel (a)</i>: Fundamental $n = 1, l = 2$ g-mode frequencies in the ocean (Equation 4.10). <i>Panel (b)</i>: The ocean-crust transition density (Equation 2.5). <i>Panel (c)</i>: Temperature at the ocean-crust transition.</p>	71
Figure 4.9:	<p>Thermal evolution as a function of time during outburst/quiescence for neutron star transients with $\langle \dot{M} \rangle = 0.1\text{--}1.0 \dot{M}_{\text{Edd}}$. <i>Panel (a)</i>: Fundamental $n = 1, l = 2$ g-mode frequencies in the ocean (Equation 4). <i>Panel (b)</i>: The ocean-crust transition density (Equation 2). <i>Panel (c)</i>: Temperature at the ocean-crust transition.</p>	73
Figure 4.10:	<p>Characteristic timescales in the neutron star ocean. The upper curves are the thermal time for an equilibrium composition (solid curve) and accreted composition (dotted curve). The lower curves are for the timescale for changes in ρ_t for an equilibrium composition (solid curve) and an accreted composition (dotted curve).</p>	77

Figure 4.11: Crust cooling models of the late time cooling of MXB 1659-29. The solid gray curve is a model that uses $Q_{\text{imp}} = 2.5$ throughout the entire crust and $T_{\text{core}} = 4 \times 10^7$ K. The solid blue curve is a model with $Q_{\text{imp}} = 20$ for $\rho > 8 \times 10^{13}$ g cm $^{-3}$, $Q_{\text{imp}} = 1$ for $\rho < 8 \times 10^{13}$ g cm $^{-3}$, $T_{\text{core}} = 3.25 \times 10^7$ K, and using the G08 pairing gap. The dashed red curve uses the same Q_{imp} as the solid blue curve, but with the S03 pairing gap. The dotted blue curve is a model with the G08 pairing gap and $Q_{\text{imp}} = 1$ throughout the crust, but without a low thermal conductivity pasta layer. 79

Figure 4.12: Thermal transport in the inner crust of MXB 1659-29 at the start of quiescence. The gray vertical lines indicate the neutron drip density and the transition to nuclear pasta. *Panel (a)*: The temperature profile (solid curve) corresponding to the cooling model in Figure 4.11 with a $Q_{\text{imp}} = 20$ pasta layer and the G08 pairing gap. The dashed curves show two choices for $T_c(\rho)$; the blue dashed curve corresponds to G08 and the red dotted curve is S03. *Panel (b)*: The heat capacity profiles for the same models as Figure 4.11. Solid black curve: $Q_{\text{imp}} = 3.7$ throughout the inner crust. Dashed blue curve: $Q_{\text{imp}} = 20$ for $\rho > 8 \times 10^{13}$ g cm $^{-3}$ and $Q_{\text{imp}} = 1$ for $\rho < 8 \times 10^{13}$ g cm $^{-3}$ using the G08 pairing gap that closes in the crust. Dotted red curve: same as dashed curve, but with a different choice for $T_c(\rho)$ from the S03 pairing gap that closes in the core. *Panel (c)*: Thermal conductivity profiles for the same models. 81

Figure 4.13: Scattering frequencies for electrons and neutrons in the inner crust at the beginning of quiescence for the model with $Q_{\text{imp}} = 20$ at $\rho > 8 \times 10^{13}$ g cm $^{-3}$, $Q_{\text{imp}} = 1$ at $\rho < 8 \times 10^{13}$ g cm $^{-3}$, and the pairing gap that closes in the crust (Gandolfi et al., 2008). *Subplot*: Thermal conductivity K from electron scattering (dotted red curve), neutron scattering (dashed blue curve), and from both electrons and neutrons (solid black curve). The mass density ρ is given in units of 10^{14} g cm $^{-3}$. The region containing nuclear pasta is to the right of the vertical black dotted line. 83

Figure 5.1: Schematic of an Urca reaction shell. The red colored region is composed of the parent nucleus, which electron captures into the daughter nucleus represented by the blue colored region. The Urca reaction layer has a thermal width $Q_{\text{EC}} \pm k_B T$, where $\mu_e \approx Q_{\text{EC}}$ is the center of the Urca shell. 88

Figure 5.2: Luminosity sources in the neutron star crust as a function of crust temperature. The red curves indicate the neutrino luminosities from Urca pairs. Blue curves indicate neutrino cooling from other processes in the neutron star crust. The gray shaded region indicates the heating luminosity from crustal heating. 91

Figure 5.3:	Quiescent lightcurve of the neutron star MAXI J0556-332. The crust model is for a $M = 1.5 M_{\odot}$, $R = 11$ km neutron star with $Q_{\text{shallow}} = 6.0$ MeV. The light curve without Urca cooling is shown as a red dashed curve. Model light curves with Urca pairs, with $L_{\nu} = 10^{36}$ ergs s^{-1} , are shown as black curves. From left to right, shell depths are $y/y_h = 3.4, 6.7, 17, 43, 140$, that correspond to $\rho_{10} = 3, 5, 10, 20, 50$, respectively.	93
Figure 5.4:	Quiescent lightcurve of the neutron star MAXI J0556-332 with an ^{33}Al Urca shell. The crust model is for a $M = 1.5 M_{\odot}$, $R = 11$ km neutron star with $Q_{\text{shallow}} = 6.0$ MeV.	94
Figure 5.5:	Schematic of the neutron star’s outer layers and the location of superburst ignition and Urca cooling pairs.	95
Figure 5.6:	Ocean temperature profiles during steady state with Urca pairs in the crust for various values of Q_b . <i>Panel (a)</i> : Abundances of Urca pairs calculated from X-ray burst ashes. <i>Panel (b)</i> : Abundances of Urca pairs calculated from superburst ashes. <i>Panel (c)</i> : Ocean temperature profiles without Urca cooling in the crust.	98
Figure 5.7:	Ocean temperature profiles during steady state with Urca pairs in the crust for uncertainties in ft -values. We test the values $Q_b = 0.1, 0.25, 1, 2$ MeV per accreted nucleon. <i>Panels (a)–(d)</i> : Abundances of crust Urca pairs calculated from X-ray burst ashes. <i>Panels (e)–(h)</i> : Abundances of crust Urca pairs calculated from superburst ashes. The upper red-dashed curves are with ft -values enhanced by a factor of 10 and the lower blue-dashed curves are for ft -values reduced by a factor of 10.	100
Figure 5.8:	Depth of Urca cooling pairs of a given mass number A . The size of data points corresponds to the coefficient L_{34} given in Equation 5.8, and can be found in Table 1. Urca pairs with $L_{34} \geq 10$ are colored in red. The gray band indicates empirical constraints on the superburst ignition depth between $y_{\text{ign}} \approx 0.5\text{--}3 \times 10^{12}$ g cm^{-2} (Cumming et al., 2006).	102
Figure 5.9:	Temperature in the ocean as a function of column depth for a neutron star model with: $\dot{m} = 0.3 \dot{m}_{\text{Edd}}$, $M = 1.4 M_{\odot}$, $R = 10$ km, and core temperature $T_{\text{core}} = 3 \times 10^7$ K. The dashed-black curves indicate the ignition of unstable carbon burning in a mixed iron-carbon ocean with $X_{\text{Fe}} = 0.8$ and $X_{\text{C}} = 0.2$. The solid-black curves indicate ocean’s without Urca cooling layers. In each panel, the lower dotted-blue curve is for $L_{34} = 100$ and the upper dotted-blue curve is for $L_{34} = 10$, for Urca pairs located at: <i>Panel (a)</i> : $y = 1.2 \times 10^{13}$ g cm^{-2} , <i>Panel (b)</i> : $y = 1.2 \times 10^{12}$ g cm^{-2} , and <i>Panel (c)</i> : $y = 1.2 \times 10^{10}$ g cm^{-2}	105

Figure 5.10: Cooling light curves for superbursts with $E_{18} = 0.2$, $\alpha = 0.25$, $g_{14} = 1.6$, and ignition depths $y_{\text{ign}} = 3.2 \times 10^{11} \text{ g cm}^{-2}$ and $y_{\text{ign}} = 3.2 \times 10^{12} \text{ g cm}^{-2}$. The red dotted curves are models without Urca cooling. The solid curves are for a cooling source at $y = 0.4 y_{\text{ign}}$ with $X \cdot L_{34} = 100, 1000$ 106

Figure 5.11: Steady state ocean temperature as a function of column depth for a neutron star model with: $\dot{m} = 0.3 \dot{m}_{\text{Edd}}$, $M = 1.4 M_{\odot}$, $R = 10 \text{ km}$, and core temperature $T_{\text{core}} = 3 \times 10^7 \text{ K}$. Solid black curves are steady state temperature profiles for the heating strengths $Q_{\text{shallow}} = 1, 2, 4$. The dashed black curve indicates the ignition of unstable carbon burning in a mixed iron-carbon ocean with $X_{\text{Fe}} = 0.8$ and $X_{\text{C}} = 0.2$ 108

Chapter 1

Introduction

The theoretical prediction (Rutherford, 1920) and discovery (Chadwick, 1932) of a neutral atomic particle, the neutron, had far reaching consequences for astronomy. It was soon proposed that supernovae mark the transition of ordinary stars into compact stars made primarily of neutrons (Baade & Zwicky, 1934). The properties of the neutron in concert with the equations of stellar structure, form a theoretical foundation for *neutron stars* (Tolman, 1934; Oppenheimer & Volkoff, 1939). On the cusp of becoming black holes, neutron stars reach densities greater than an atomic nucleus in their cores and epitomize the fascinating nature of matter under the most extreme conditions. Decades after their conception, neutron stars were discovered at X-ray wavelengths (Giacconi et al., 1962) and radio wavelengths (Hewish et al., 1968), and with the advent of modern space-based telescopes (e.g., *Chandra* X-ray Observatory) it was discovered that neutron stars produce a diverse array of high-energy phenomena.

Of particular interest to the study of the neutron star interior is the X-ray emission from low-mass X-ray binaries, where a neutron star primary orbits with a low-mass companion. An accretion disk forms around the neutron star as a result of mass transfer from the low-mass companion. Neutron stars with accretion disks undergo sporadic accretion outburst episodes that may last for weeks to years; for example, accretion outbursts are observed on the accretion neutron star KS 1731-260 (Sunyaev & Kwant Team, 1989; Wijnands et al., 2001). The accumulating material during an accretion outburst triggers non-equilibrium reactions in the neutron star's outer layers (Sato, 1979; Bisnovatyĭ-Kogan & Chechetkin, 1979) which may heat the crust out of thermal equilibrium with

the core (Brown & Bildsten, 1998; Brown, 2000). When the accretion outburst ends, stored heat from accretion-driven reactions diffuses toward the neutron star's surface where it powers the quiescent light curve (Eichler & Cheng, 1989; Ushomirsky & Rutledge, 2001; Rutledge et al., 2002). Reproducing the observed quiescent light curve with numerical models reveals new clues about the physics of the interior.

For instance, the cooling behavior of neutron star transients reveals the thermal properties of nuclear pasta. Deep in the neutron star's crust, nuclei are deformed into various complex shapes in the high density environment (Ravenhall et al., 1983; Hashimoto et al., 1984). Nuclear pasta has been studied extensively using molecular dynamics simulations (e.g., Horowitz et al. 2004a), but the thermal and electrical conductivities remain difficult to determine (Horowitz et al., 2015). The late time cooling of quiescent neutron star transients, however, is sensitive to the thermal transport properties of the deep inner crust. As a result, late time cooling light curves may reveal the thermal conductivity of pasta (Horowitz et al., 2015; Deibel et al., 2017). Furthermore, the late time cooling is also sensitive to the thermal properties of normal and superfluid neutrons that coexist with the pasta at high densities.

Models of cooling neutron stars also pose new questions. For example, the large quiescent luminosities of some neutron star transients, such as the hottest transient MAXI J0556-332 (Homan et al., 2014), can not be explained by accretion-driven heating alone (Deibel et al., 2015). Interestingly, reconciling neutron star superburst observations with superburst ignition models also requires extra heating in the neutron star's outer layers (Cumming et al., 2006). The source of extra heating is unknown, but may be connected to the deposition of rotational energy in the neutron star ocean by a spreading boundary layer of accreted material (Inogamov & Sunyaev, 1999, 2010; Philippov et al., 2016).

Thermonuclear bursts from accretion neutron stars also provide an avenue to examine the

physics of the neutron star interior. For example, X-ray bursts observed from neutron star transients are well fit by unstable ignition of hydrogen and helium in the neutron stars envelope (Woosley et al., 2004). Long type-I X-ray bursts, or superbursts, are even more energetic explosions in the neutron star envelope (Woosley & Taam, 1976; Taam & Picklum, 1978). Superbursts are thought to be triggered by the unstable ignition of the $^{12}\text{C} + ^{12}\text{C}$ fusion reaction (Cumming & Bildsten, 2001; Strohmayer & Brown, 2002a). Much like the crust cooling models of neutron star transients, superburst ignition models require anomalous extra heating to ignite carbon at the depths inferred from superburst cooling light curves (Cumming et al., 2006). The source of extra heating in these models is unknown, but is required to match observed ignition depths for all superbursts.

The physics of the neutron star interior may be altered by bygone nuclear burning in the neutron star envelope. Nuclear burning during X-ray bursts and superbursts produces an array of proton-rich nuclei (Wallace & Woosley, 1981; Woosley et al., 2004; Keek & Heger, 2011). The ashes of nuclear burning are compressed to greater depths in the neutron star's ocean and crust by subsequent accretion outbursts. Not only does compression deposit heat via nuclear reactions (Haensel & Zdunik, 1990, 2008), but advances in accretion-driven nuclear reaction studies (Schatz et al., 2014) have revealed that neutrino cooling may occur in nuclear burning ashes. Some nuclei form e^- -capture / β^- -decay cycles, known as Urca cycles, that emit neutrinos and effectively cool the neutron star's outer layers (Gamow & Schoenberg, 1941; Bahcall & Wolf, 1965). Neutrino cooling will in turn impact thermal evolution models of neutron star transients (Meisel & Deibel, 2017) and carbon ignition depths in superburst ignition models (Deibel et al., 2016).

Isolated and highly-magnetized neutron stars, or magnetars, produce energetic γ -ray flares (Barat et al., 1983) which may offer a glimpse of the neutron star's interior. These giant flares may be triggered by a reconfiguration of the magnetic field which fractures the crystalline crust and induces oscillations in the crust, or starquakes (Duncan, 1998). Quasi-periodic oscillations

in the γ -ray flare emission (Israel et al., 2005; Strohmayer & Watts, 2005; Watts & Strohmayer, 2006) may be modes of the oscillating crust. Because crust oscillation modes are uniquely determined by neutron star properties, a study of these oscillations may lead to constraints on the interior physics (Piro, 2005; Steiner & Watts, 2009; Deibel et al., 2014). Although quasi-periodic oscillations originate from accretion disks around accreting black holes and neutron stars (e.g., Lewin & van der Klis 2006), surface oscillations are a compelling explanation for the observed quasi-periodic oscillations in magnetars; magnetars are isolated and do not have an accretion disk due to mass transfer from a companion. Furthermore, matching observed oscillation frequencies to crust oscillation frequencies can produce constraints relevant for nuclear theory because crust oscillation frequencies are sensitive to the highest density regions of the neutron star crust.

We begin in Chapter 2 by constructing a model of the neutron star's outer layers. This model draws from nuclear theory and uses energetic arguments to calculate a ground-state composition for the neutron star's outer layers. A model of the equilibrium composition is a necessary starting point when studying the dynamical, compositional, and thermal evolution of the neutron star's outer layers. We also discuss a calculation for the accreted composition by following nuclear reactions in accreted material using energetic arguments. The thermal transport properties of the interior, such as the specific heat and thermal conductivity of various layers, are also discussed.

In Chapter 3, the crust model is applied to calculating crust oscillation frequencies for starquaking magnetars. The large magnetic fields of magnetars $\gtrsim 10^{14}$ G alter the crust composition by quantizing electrons. Furthermore, magnetic driven Alfvén waves in the crust must be incorporated into solutions for crust oscillations. We match crust oscillation frequencies to the observed giant flare quasi-periodic oscillations in the magnetars SGR 1806-20 and SGR 1900+14 to draw constraints on the structure of these stars and nuclear physics at high mass densities.

Moving away from isolated neutron stars, we examine the observable phenomena of neutron

stars in accreting systems. Chapter 4 demonstrates that not only can crust models reproduce observations, but they can probe the neutron star interior in an intuitive manner. By implementing the thermal transport properties of dense matter into the crust model, we follow the thermal evolution of cooling neutron star transients (Chapter 4). Such a calculation is applicable to low-mass X-ray binaries where a neutron star primary orbits with a low-mass companion. During an accretion outburst onto the neutron star primary, the continual compression of the neutron star's outer layers induces non-equilibrium reactions in the crust; reactions that heat the neutron star crust out of thermal equilibrium with the core. We model the thermal relaxation of the crust when accretion halts and accurately reproduce quiescent light curves of neutron star transients. These fits reveal, for example, that powerful heating during outburst is required to fit the quiescent observations of the neutron star MAXI J0556-332 and the source of this extra heating remains unknown.

Being confident in our knowledge of thermal transport in the crust, we outline an observational test to answer an open question in neutron star transient observations. Observed quasi-periodic oscillations in the transient neutron star Z-sources, such as Sco X-1, are of unknown origin. Curiously, some observed frequencies are close to the neutron star ocean's thermal g-mode frequencies. Reproducing thermal g-modes in our model, we investigate if observed oscillations originate in the ocean. In particular, we show that as the ocean heats up during accretion, thermal g-mode frequencies increase, and we predict that observed oscillation frequencies should be larger in hotter neutron star transients.

We then incorporate nuclear reactions into the crust model and demonstrate that light curve fits to neutron star transients constrain nuclear processes (Chapter 5). Specifically, we use the quiescent light curve of MAXI J0556-332 to determine if Urca cooling reaction layers, rapid back-and-forth cycles of e^- -capture and β^- -decay, are active in the accreting neutron star crust. We demonstrate that a crust thermal relaxation model with Urca cooling layers does not produce a

light curve consistent with the quiescent observations of MAXI J0556-332. This work motivates subgrid models of Urca cooling reactions to further resolve the reaction's properties and delineate its impact on X-ray bursts, superbursts, and crust thermal relaxation.

Lastly, we discuss the prospects of future research. A high priority is determining the origin of the anomalous extra heating in neutron star transients, such as the hottest transient MAXI J0556-332. Extra heating, from an unknown origin, is also required in superburst ignition models. Preliminary studies suggest that the extra heating may be from friction at the base of the neutron star ocean, as the ocean is spun up to higher rotation velocities during accretion.

Chapter 2

The Neutron Star Ocean and Crust

In this chapter we outline the physics input for numerical models of a neutron star's outer layers. In particular, the numerical model includes a calculation of the composition from the low-density equation of state and the thermal transport properties of the neutron star's outer layers. The equilibrium composition will then be used in the context of highly-magnetized neutron stars in Chapter 3. In Chapter 4, the thermal transport properties of the outer layers are used to investigate the thermal evolution of neutron star transients.

2.1 Structure

An accreted fluid element will first enter the neutron star atmosphere which is rarified hydrogen. A schematic of neutron star structure can be seen in Figure 2.1. Nuclei heavier than hydrogen gravitationally settle to the bottom of the atmosphere and form a boundary layer between the atmosphere and the ocean beneath. The ocean is a plasma of ions and electrons, and contains nuclear burning shells that alter the ocean's composition. For example, hydrogen-rich and helium-rich material burn to iron-group elements (Taam et al., 1996). The electrons are partially degenerate and relativistic, and provide the majority of the pressure support. Moving deeper into the ocean, the electron gas becomes degenerate and highly relativistic near $\rho \gtrsim 10^6 \text{ g cm}^{-3}$ and the pressure

is (see Chapter 2, Shapiro & Teukolsky 1983)

$$P = P_e \approx \frac{p_{F,e}^4 c}{12\pi^2 \hbar^3}, \quad (2.1)$$

where $p_{F,e} = \hbar(3\pi^2 n_e)^{1/3}$ is the electron Fermi momentum and n_e is the number density of electrons. When scaled to typical values of the ocean the pressure is

$$P \approx 3.6 \times 10^{26} \text{ ergs cm}^{-3} \rho_9^{4/3} (Y_e/0.4)^{4/3}, \quad (2.2)$$

where Y_e is the electron fraction and $\rho_9 \equiv \rho/(10^9 \text{ g cm}^{-3})$. Now we can define column depth ($y \approx P/g$) as

$$y \approx 3.6 \times 10^{12} \text{ g cm}^{-2} \rho_9^{4/3} (Y_e/0.4)^{4/3} g_{14}^{-1}, \quad (2.3)$$

where the surface gravity is $g_{14} = g/(10^{14} \text{ cm s}^{-2})$.

A phase transition occurs at the bottom of the ocean where the ion density becomes high, and the ocean nuclei crystallize into a solid *crust* (Baym et al., 1971b; Horowitz & Berry, 2009) due to Coulomb repulsion of the constituent ions (Wigner, 1934). The point at which the ion-liquid ocean crystallizes into an ion-lattice is determined by the plasma coupling parameter of a composition with average proton number $\langle Z \rangle$,

$$\Gamma = \frac{\langle Z \rangle^2 e^2}{ak_B T}, \quad (2.4)$$

where $a = (3\langle Z \rangle/4\pi n_e)^{1/3}$ is the radius of the Wigner-Seitz cell (i.e., the inter-ionic spacing). The ocean's crystallization point (or the crust's melting point) occurs when $\Gamma = 175$ (Farouki & Hamaguchi, 1993; Potekhin & Chabrier, 2000; Horowitz et al., 2010). Therefore, rearranging

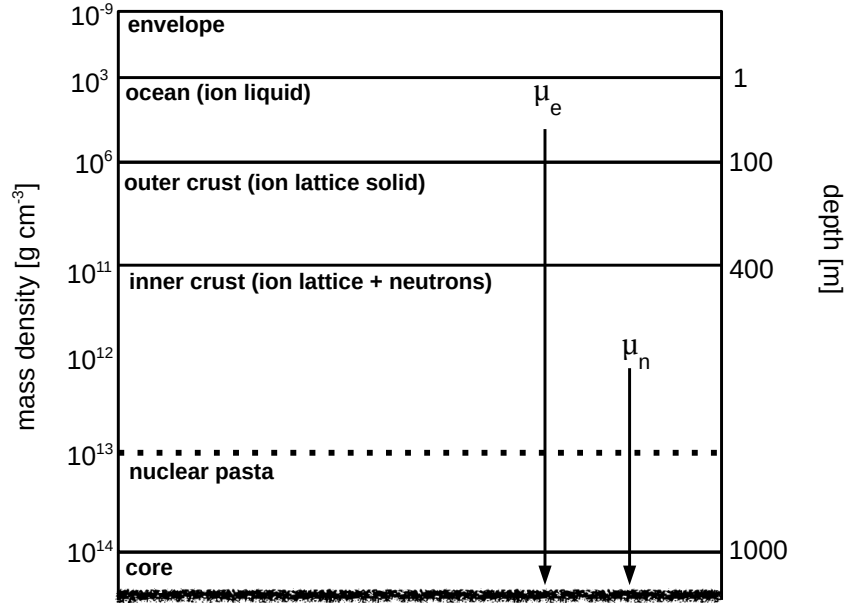


Figure 2.1: Schematic of a neutron star's structure. Degenerate electrons provide the primary pressure support in the outer crust and overlying layers. In the inner crust, the dripped neutrons begin providing the primary pressure support.

Equation 2.4, the ocean-crust transition density can be expressed as

$$\rho_t \approx 2.2 \times 10^6 \text{ g cm}^{-3} \left(\frac{T}{3 \times 10^7 \text{ K}} \right)^3 \left(\frac{26}{\langle Z \rangle} \right)^6 \left(\frac{\langle A \rangle}{56} \right). \quad (2.5)$$

where $\langle A \rangle$ is the average mass number of the composition. The ocean-crust transition density as a function of crust temperature can be seen in Figure 2.2. At mass densities $\rho > \rho_t$ the liquid ion-ocean crystallizes into a body-centered cubic nuclear lattice known as the *outer crust*. The pressure in the outer crust is primarily supported by the degenerate and relativistic electron gas with a small pressure contribution from the nuclear lattice (Baym et al., 1971a,b).

The crust is composed of a nuclear crystal lattice embedded in an degenerate electron gas at lower densities ($\rho_t \lesssim \rho \lesssim \rho_{\text{drip}} \approx 4 \times 10^{11} \text{ g cm}^{-3}$). A quasi-free neutron gas appears at higher densities $\rho \gtrsim \rho_{\text{drip}}$; The neutron-drip point, the point at which it becomes energetically favorable for neutrons to drip out of nuclei, marks the beginning of the *inner crust*. The inner

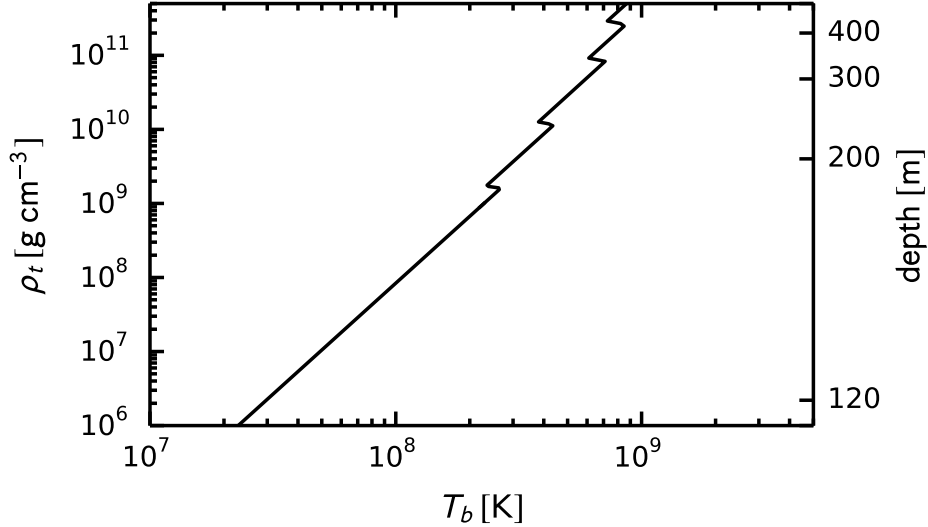


Figure 2.2: Ocean-crust transition density as a function of temperature for a neutron star with $g_{14} = 1.85$ and using the crust equation of state from Haensel & Zdunik (1990).

crust can then be described as a nuclear lattice embedded in both a degenerate electron gas and a quasi-free neutron gas (Baym et al., 1971a), so the total pressure has three contributions, from the electrons, lattice, and quasi-free neutrons. The neutron pressure becomes the primary pressure support at mass densities near $\rho \gtrsim 4 \times 10^{12} \text{ g cm}^{-3}$ in the inner crust (Shapiro & Teukolsky, 1983), though the electron gas still has a non-negligible pressure contribution. In the deep inner crust at mass densities near $\rho \gtrsim 6 \times 10^{13} \text{ g cm}^{-3}$ the nuclei deform in an attempt to minimize their energy at such extreme pressures. These deformed nuclei are called *nuclear pasta* (Ravenhall et al., 1983; Pethick & Ravenhall, 1995; Pethick & Potekhin, 1998) and have been studied through semi-classical molecular dynamics simulations (Horowitz et al., 2004b; Horowitz & Berry, 2008; Schneider et al., 2013). The thermal transport properties of the nuclear pasta phase, however, remains unknown (Horowitz et al., 2015). We will discuss the possibility of constraining the thermal conductivity of pasta using late time observations of cooling neutron stars in Section 4.4.

The crust dissolves into a nucleon liquid near a mass density $\rho \approx 2.8 \times 10^{14} \text{ g cm}^{-3}$ (Baym et al., 1971a) via a first order phase transition which marks the beginning of the outer core. The crust-

core transition occurs slightly above the nuclear saturation density $\rho_0 \approx 2 \times 10^{14} \text{ g cm}^{-3}$ (Baym et al., 1971a; Pethick et al., 1995) — the density of an atomic nucleus. The outer core contains μ, e, n, p matter because the electron chemical potential μ_e approaches the rest-mass energy of the muon ($m_\mu c^2 \approx 105 \text{ MeV}$). The pressure support comes from the repulsive core of the nuclear force because nucleons are packed to densities $\rho \gg \rho_0$.

2.2 Low-density Equation of State

The crust composition at a given mass density is calculated by examining the total energy density of the system. The crust is imagined as a series of “drops” of nuclear matter, each inside an identical Wigner-Seitz cell. The energetics of a single cell, how a nucleus interacts with the electron and neutron gases sharing the cell, is assumed to represent the entire crust at the mass density considered. The nucleus occupies a volume fraction χ of the cell and the average baryon density in the nucleus is $n_l = n_n + n_p$, where n_n is the density of neutrons and n_p the density of protons inside the nucleus. The number density of baryons per unit volume is $n = \chi(n_n + n_p) + (1 - \chi)n_{\text{drip}}$, where n_{drip} represents the density of quasi-free dripped neutrons. The total energy density of the crust is

$$w(Z, A, n) = \chi \left[n_n m_n + n_p m_p + n_l \frac{E_{\text{bind}}(Z, A)}{A} \right] + (1 - \chi) \epsilon(n_n = n_{\text{drip}}, n_p = 0) + w_e(n_e), \quad (2.6)$$

where w_e and n_e are the energy density and number density of electrons, respectively. Note that $w_e = 3P_e$ where P_e is the degenerate electron pressure given in Equation 2.1. We use a liquid drop mass model (Baym et al., 1971a,b; Ravenhall et al., 1983; Steiner, 2008) for the nucleus binding energy E_{bind} that contains the energy density contributions from the nucleus and the lattice: the

Coulomb energy ($w_{\text{Coul.}}$), the surface energy (E_{surf}), the shell energy (E_{shell}), and pairing energy (E_{pair}) corrections to the homogeneous bulk matter Hamiltonian (ϵ) of bulk n, p, e matter.

2.2.1 Nuclei and the Ion-lattice

In both the inner and outer crust the nuclear contribution to the energy density will be that of the equilibrium nucleus at the given baryon density. The lattice contribution will be that of a crystal lattice composed of equilibrium nuclei. For these contributions to the energy density we use a liquid-drop mass model which includes the lattice contribution (Baym et al., 1971a,b; Ravenhall et al., 1983; Steiner, 2008). We also add shell corrections to the mass model as described in Dieperink & van Isacker (2009) and an updated neutron-drip line to better predict the neutron rich nuclei beyond the neutron-drip point. The first term on the right-hand side of Equation 2.6 represents the energy density of the nucleus and the lattice;

$$n_n m_n + n_p m_p + n_l \frac{E_{\text{bind}}(Z, A)}{A} = \epsilon(n_n, n_p) + \frac{n_l}{A} (E_{\text{surf}} + E_{\text{shell}} + E_{\text{pair}}) + w_{\text{Coul.}} \quad (2.7)$$

where n_n , n_p , and n_l are respectively the average neutron, proton, and baryon number densities inside the nucleus with a given proton number Z and baryon number A . The parameters m_n and m_p are the neutron and proton masses. The above parameters will be determined from

$$n_l = n_n + n_p = n_0 + n_1 I^2, \quad (2.8)$$

where $I = 1 - 2Z/A$ is the isospin asymmetry. The quantity n_0 is the nuclear saturation density and n_1 is a negative quantity that allows for the decrease in saturation density based on the isospin asymmetry and the increase of saturation density due to the Coulomb interaction (Steiner, 2008).

The average neutron and proton densities within the nucleus are

$$n_n = n_l(1 + \delta)/2 ,$$

and

$$n_p = n_l(1 - \delta)/2 , \tag{2.9}$$

where $\delta = 1 - 2n_p/(n_n + n_p)$ is the density asymmetry and $\eta = \delta/I = 0.92$ is a constant of our model that will determine the thickness of a neutron skin (i.e., the difference between neutron and proton radii; Steiner 2008). The bulk matter binding energy is

$$E_{\text{bulk}} = \frac{A}{n_l} [\epsilon(n_n, n_p) - n_n m_n - n_p m_p] , \tag{2.10}$$

where $\epsilon(n_n, n_p)$ is the energy density of homogeneous bulk matter at a given neutron and proton number density, for which we use the bulk matter Hamiltonian in the Skyrme model (Skyrme, 1959) with SLy4 coefficients (Chabanat et al., 1995). The surface energy goes as

$$E_{\text{surf}} = \sigma F(n_n, n_p) \left(\frac{36\pi}{n_l^2 A} \right)^{1/3} , \tag{2.11}$$

where the unitless function F that is proportional to the surface tension σ is

$$F(n_n, n_p) = 1 - \sigma_\delta \delta^2 , \tag{2.12}$$

where σ_δ represents the surface energy density (Myers & Swiatecki, 1969; Steiner et al., 2005).

The Coulomb energy density is

$$w_{\text{Coul.}} = \frac{2\pi}{5} n_p^2 e^2 R_p^2 (2 - 3\chi^{1/3} + \chi) , \quad (2.13)$$

where e^2 is the Coulomb coupling and R_p is the proton radius ($3Z = 4\pi n_p R_p^3$). The respective χ terms in parenthesis correspond to the Coulomb contribution, the lattice contribution, and a high density correction as χ approaches unity. The shell corrections to the binding energy per baryon (Sato, 1979; Dieperink & van Isacker, 2009) are

$$E_{\text{shell}}(Z, N) = a_1 S_2 + a_2 (S_2)^2 + a_3 S_3 + a_{np} S_{np} , \quad (2.14)$$

where

$$S_2 = \frac{n_v \bar{n}_v}{D_n} + \frac{z_v \bar{z}_v}{D_z} , \quad (2.15)$$

$$S_3 = \frac{n_v \bar{n}_v (n_v - \bar{n}_v)}{D_n} + \frac{z_v \bar{z}_v (z_v - \bar{z}_v)}{D_z} , \quad (2.16)$$

$$S_{np} = \frac{n_v \bar{n}_v z_v \bar{z}_v}{D_n D_z} , \quad (2.17)$$

and

$$\bar{n}_v \equiv D_n - n_v ,$$

$$\bar{z}_v \equiv D_z - z_v . \quad (2.18)$$

The parameters D_n and D_z correspond to the degeneracy of the neutron and proton shells, i.e., the difference between the magic numbers enclosing the current amount of neutrons or protons. The quantities n_v and z_v are the number of valence neutrons and protons, i.e., the difference between the current number of protons or neutrons and the preceding magic number. The effect of the

Table 2.1: Parameters of the mass model.

Parameter	SLy4	Rs
n_0	0.1740 fm^{-3}	0.1597 fm^{-3}
n_2	-0.0157 fm^{-3}	0.0244 fm^{-3}
η	0.9208	0.9043
σ_δ	1.964	1.465
σ	1.164 MeV	1.041 MeV
a_1	-1.217 MeV	-1.298 MeV
a_2	0.0256 MeV	0.0311 MeV
a_3	0.00387 MeV	0.00349 MeV
a_{np}	0.0357 MeV	0.0287 MeV
a_p	5.277 MeV	5.265 MeV

shell corrections on the composition of the crust can be seen in Figure 2.3. The pairing contribution to the energy density taken from Brehm (1989) with updated coefficients is

$$E_{\text{pair}} = \begin{cases} -a_p A^{-1/3}, & \text{even-even,} \\ +a_p A^{-1/3}, & \text{odd-odd,} \\ 0, & \text{even-odd,} \end{cases} \quad (2.19)$$

where a_p is a constant of our model. The combined contributions of nuclear matter and the nuclei crystal lattice result in the expression,

$$w_{\text{nuc}} + w_l = (n_n + n_p)\chi B(Z, A)/A. \quad (2.20)$$

The coefficients used in the mass model above are listed in Table 2.1.

2.2.2 Quasi-free Neutrons

The energy density of dripped neutrons is that of bulk neutron matter,

$$\epsilon_{n,\text{drip}} = (1 - \chi)\epsilon(n_{n,\text{drip}}, n_p = 0), \quad (2.21)$$

where we use the SLy4 bulk matter energy density (Skyrme, 1959) with SLy4 coefficients (Chabanat et al., 1995). The number density of dripped neutrons is determined from (Baym et al., 1971a)

$$n = \chi(n_n + n_p) + n_{n,\text{drip}}(1 - \chi), \quad (2.22)$$

where n is the number density of baryons. The approach accounts for the filling of space with dripped neutrons, as opposed to nucleic matter, at depths greater than the neutron-drip point $\rho \gtrsim \rho_{\text{drip}} \approx 4 \times 10^{11} \text{ g cm}^{-3}$. As the density approaches nuclear saturation the fraction of space filled by the neutron gas approaches unity, that is, the filling fraction of nuclei χ goes to zero.

2.3 Composition

The crust equation of state discussed in Section 2.2 can be used to calculate the composition of the neutron star crust. In a cold-catalyzed crust, a crust made of nuclei frozen in from the neutron star's birth, the composition is in its most energetically favorable configuration. A cold-catalyzed composition is typically adequate when modeling neutron star observables. Accreting neutron stars, however, have crusts polluted by compressed accreted material and thermonuclear burning ashes. A calculation of the accreted neutron star crust must account for the nuclear reactions that take place in an accreted fluid element as it is compressed through the electron gas of the outer crust and the quasi-free neutron gas of the inner crust.

2.3.1 Equilibrium

The ocean and crust of an isolated neutron star are composed of cold-catalyzed matter remaining from when the neutron star was first formed. During the hot post-supernova conditions all nuclear

reactions are assumed possible and the composition will find the most energetically favorable configuration. The most energetically favorable configuration is found by minimizing the total energy density (Equation 2.6) at a given mass density. The nucleus that minimizes the total energy density is called the *equilibrium nucleus*.

We now use the formulae outlined in the previous section to calculate the equilibrium composition of the ocean and crust of an isolated neutron star. The equilibrium composition for the SLy4 crust equation of state is shown in Figure 2.3. In the neutron star ocean, at mass densities $\rho < 10^6 \text{ g cm}^{-3}$, the equilibrium nucleus is ^{56}Fe as it has the minimum binding energy per baryon in our mass model. At mass densities $\rho \gtrsim 10^6 \text{ g cm}^{-3}$ electrons are degenerate and relativistic, and the electron chemical potential μ_e increases monotonically with mass density. As a consequence, the equilibrium nucleus must be increasingly neutron-rich, otherwise it would energetically favor the nucleus to undergo e^- -capture .

2.3.2 Accreted

On accreting neutron stars, the accumulation of accreted material in the envelope compresses deeper layers and replaces the existing composition. In fact, the entirety of the ocean and crust are replaced by accreted material over a timescale of $\sim 10^6$ years. Although an accretion outburst initially deposits hydrogen-rich and helium-rich material into the envelope, the accreted material eventually burns to heavier elements via the 3α , αp , and rp -processes (Wallace & Woosley, 1981). For example, unstable burning during type-I X-ray bursts produces range of nuclei with $A \sim 60\text{--}100$ (Schatz et al., 1998, 2001; Brown et al., 2002; Schatz et al., 2003; Woosley et al., 2004; Cyburt et al., 2010), which are pushed deeper into the neutron star by subsequent accretion outbursts. A neutron star crust composed of cold-catalyzed matter, that is, a crust of entirely equilibrium nuclei, is ultimately replaced by ashes compressed by accretion.

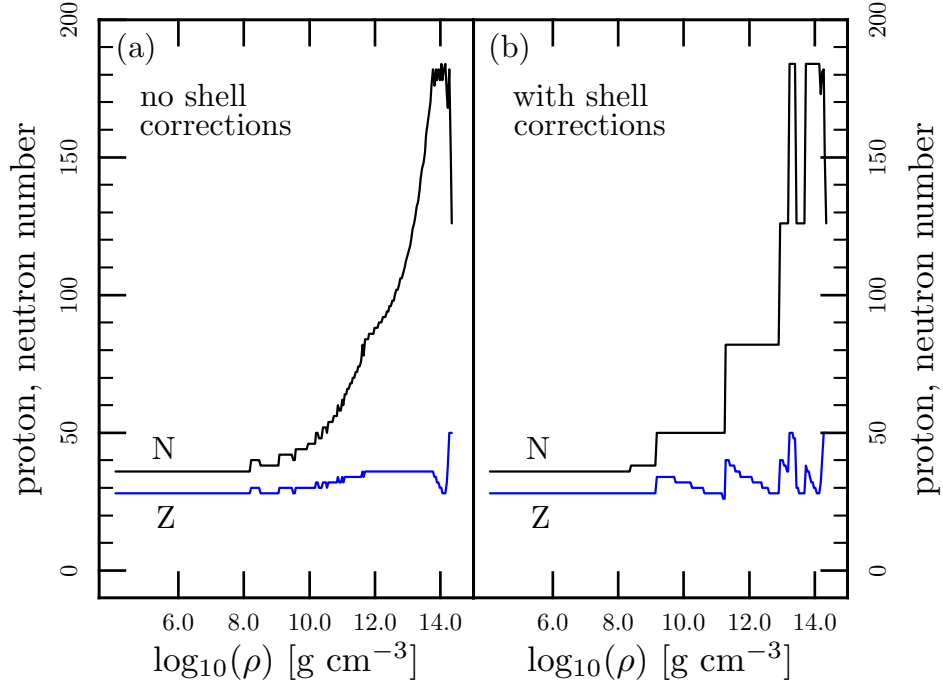


Figure 2.3: Equilibrium crust composition in the neutron star for the SLy4 crust equation of state. The panels are (a) the crust composition without shell corrections and (b) the crust composition with shell corrections. The shell correction to the binding energy is shown in Equation (2.14). This figure is reproduced from Deibel et al. (2014).

In addition to replacing the pristine crust, accreted material undergoes non-equilibrium processes that deposit heat (Bisnovatyĭ-Kogan & Chechetkin, 1979; Sato, 1979; Haensel & Zdunik, 1990). More recent studies of non-equilibrium processes, the excited states of nuclei, and pycnonuclear reactions, have refined our understanding of the amount of heat deposited in the crust during accretion as well as the final composition of the accreted crust (Haensel & Zdunik, 2003, 2008; Gupta et al., 2007; Gupta et al., 2008; Steiner, 2012; Lau, 2012). The accreted crust composition is thought to have a low impurity parameter (Equation 2.32), a result that is further supported by observations of neutron star crust cooling in quasi-persistent transients (Brown & Cumming, 2009).

The energetics of the electron and neutron gases in the crust determine the allowed reactions in an accreted element. The accreted material at a given depth in the crust must be composed of

nuclei that stably co-exist with the electron and neutron gas at that depth. The stability criterion for nuclei in the crust is outlined in Appendix 6.

An accreting neutron star will have a crust composition set by the composition of initially accreted material and how that material is altered by the subsequent non-equilibrium reactions (Bisnovatyĭ-Kogan & Chechetkin, 1979; Sato, 1979) that take place as it is compressed deeper in the star by ongoing accretion. An example of a non-equilibrium reaction is an electron capture, which occurs in the crust when

$$\mu_e - B(Z, A) > \Delta_n - B(Z - 1, A) \quad (2.23)$$

where $B(Z, A)$ is the binding energy of the nucleus and $\Delta_n \equiv m_n - m_p - m_e$ is the binding energy of the neutron. As μ_e increases with depth in the outer crust, e^- -capture reactions occur that push the composition to neutron-rich isotopes. In addition to changing the crust composition, non-equilibrium reactions deposit $\approx 1\text{--}2$ MeV per accreted nucleon of heat into crust (Haensel & Zdunik, 1990, 2003; Gupta et al., 2007; Gupta et al., 2008; Haensel & Zdunik, 2008; Lau, 2012).

The condition for *local* stability against non-equilibrium reactions is (derived in Appendix 6)

$$\frac{\partial^2 B}{\partial Z^2} + \frac{\partial^2 B}{\partial A^2} < 0, \quad (2.24)$$

which holds for all combinations of e^- -capture, β^- -decay, n -capture, and n -emission. The chemical potential of electrons μ_e and the chemical potential of neutrons μ_n determine the non-equilibrium nuclear reactions that will take place in accreted material during compression.

In the outer crust electron captures make the composition more neutron-rich until the neutron-drip point is reached. In the inner crust neutron emissions make nuclei lighter and contribute neu-

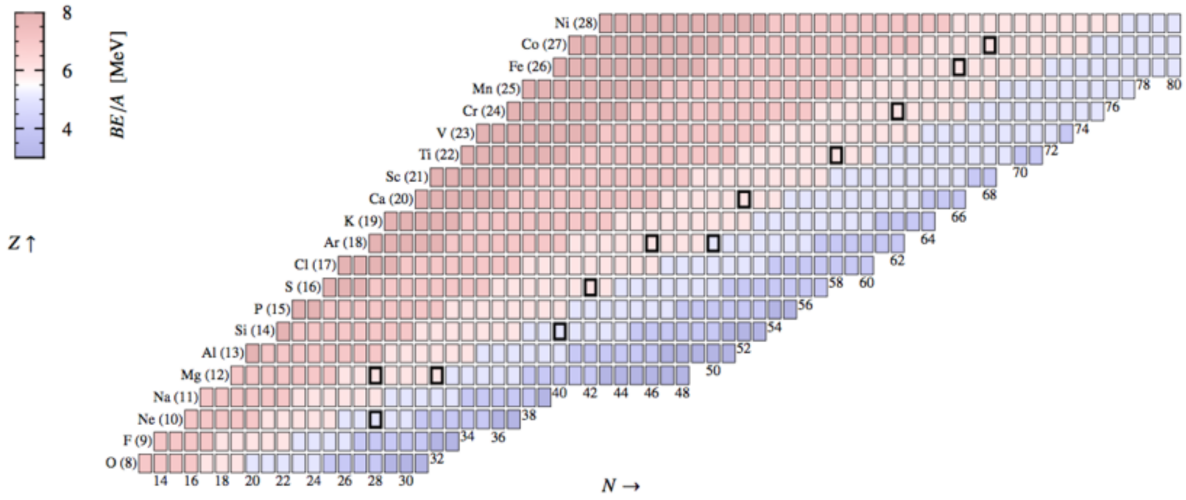


Figure 2.4: Nuclear landscape in the inner crust at $\rho = 6 \times 10^{12} \text{ g cm}^{-3}$. Black squares indicate locally stable nuclei that satisfy the stability condition in Equation 2.24. Nuclei are colored according to the binding energy per nucleon.

trons to the quasi-free neutron gas until the crust-core transition is reached. Using only energetic arguments, the nuclei in the accreted element are forced to “land” on stable nuclei at each depth. In other words, the stable nuclei that make up the composition at a given density are nuclei which can stably co-exist with the electron and neutron gases at their respective chemical potentials. The accreted crust is composed of stable isotopes that may or may not be equilibrium nuclei.

2.4 Thermal Transport

For studies of the thermal evolution of accreting neutron stars (discussed in Chapter 4) it is necessary to formulate expressions for the thermal transport properties of the neutron star’s outer layers. Heat diffuses throughout the entire crust through electron conduction and the evolution of temperature with time follows the thermal diffusion equation

$$\frac{\partial T}{\partial t} = \frac{\epsilon_{\text{nuc}} - \epsilon_{\nu}}{C_V} - \frac{1}{4\pi r^2 \rho C_V} \frac{\partial}{\partial r} \left(-4\pi r^2 K \frac{\partial T}{\partial r} \right), \quad (2.25)$$

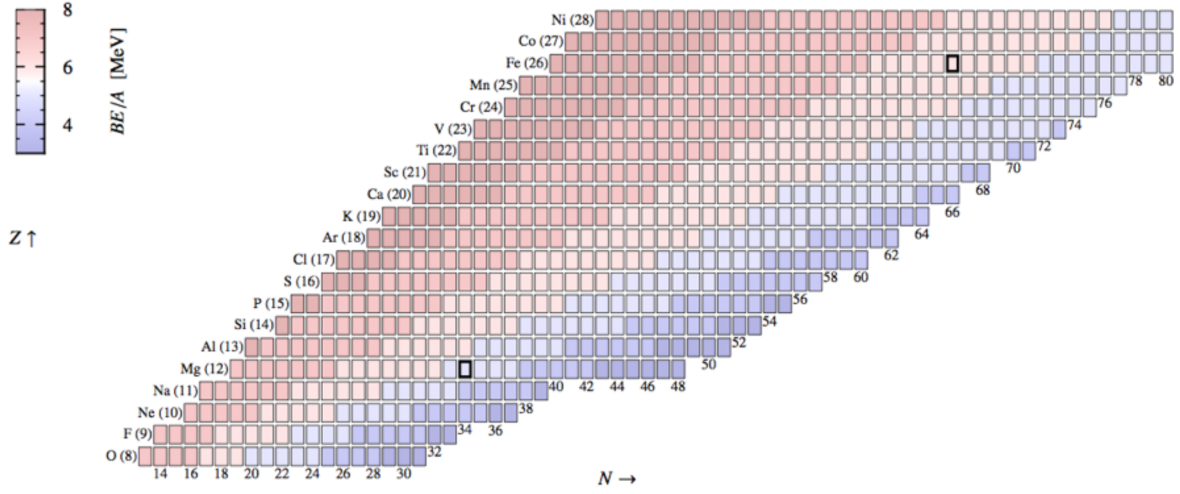


Figure 2.5: Nuclear landscape in the inner crust at $\rho = 2 \times 10^{13} \text{ g cm}^{-3}$. Black squares indicate locally stable nuclei that satisfy the stability condition in Equation 2.24. Nuclei are colored according to the binding energy per nucleon.

where C_V is the specific heat, ϵ_ν is the specific neutrino emissivity, ϵ_{nuc} is the specific nuclear heating emissivity, K is the thermal conductivity and we have ignored general relativistic corrections over a thin shell. The derivation of the expression in Equation 2.25 can be found in Appendix 6.

2.4.1 Outer Crust

In the outer crust, the degenerate electron gas mediates the thermal transport. The thermal conductivity of the electrons is

$$K_e = \frac{\pi^2 n_e c^2 k_B^2 T}{3 E_{F,e} \nu}, \quad (2.26)$$

where $\nu = \sum_j 1/\tau_j$ is the total electron scattering frequency from j sources, τ is the relaxation time of electron scattering off of scatterer j , and $E_{F,e}$ is the electron Fermi energy. The dominant contribution to the electron scattering frequency depends on the electron temperature relative to the plasma temperature, $T_P = (\hbar/k_B)\omega_P$ and the electron plasma frequency is $\omega_P = (\hbar/k_B)(4\pi Z^2 e^2 n / Am_u)^{1/2}$.

In the ocean, the contributions to the total electron scattering frequency are $1/\tau = 1/\tau_{ee} + 1/\tau_{ei}$, where $\nu_{ee} = 1/\tau_{ee}$ is the electron-electron scattering frequency and $\nu_{ei} = 1/\tau_{ei}$ is the electron-ion scattering frequency. Because the electrons are degenerate at densities of interest $\gtrsim 10^6 \text{ g cm}^{-3}$ in the ocean, only electron-ion scattering is important. If the crust temperature is $T > \Theta_D$, where the Debye temperature is $\Theta_D \approx 0.45T_p$, the specific heat is set by the electrons

$$C_V^e = \pi^2 \frac{Zk_B^2 T}{Am_p E_{F,e}}, \quad (2.27)$$

and the thermal conductivity is set by electron-ion scattering (Yakovlev & Urpin, 1980; Potekhin et al., 1997, 1999),

$$\nu_{ei} = \frac{4E_{F,e} Z \alpha^2 \Lambda_{ei}}{3\pi\hbar}, \quad (2.28)$$

where $\alpha = e^2/\hbar c$ is the fine structure constant and Λ_{ei} is the Coulomb logarithm for electron-ion scattering. This treatment of electron-ion scattering is a good approximation for one-component compositions, but accreted crusts with multi-component compositions have a lower thermal conductivity than found using this method (Roggero & Reddy, 2016). At mass densities above the ocean-crust transition (Equation 2.5), the specific heat is set by the ions

$$C_V^{\text{ion}} \approx \frac{3k_B}{Am_u} \quad (2.29)$$

and the thermal conductivity is also set by electron-ion scattering. When the crust temperature is $T \lesssim \Theta_D$, however, the thermal conductivity is set by electron-phonon scattering (Yakovlev & Urpin, 1980; Baiko & Yakovlev, 1995, 1996),

$$\nu_{ep} \approx 13\alpha \frac{k_B T}{\hbar}, \quad (2.30)$$

where $\alpha = e^2/\hbar c \approx 1/137$ is the fine structure constant. In this same temperature regime ($T \lesssim \Theta_D$), if impurities exist in the crust then electron-impurity scattering becomes important, with scattering frequency (Flowers & Itoh, 1976; Brown & Cumming, 2009),

$$v_e Q = \frac{4\pi Q_{\text{imp}} e^4 n_{\text{nuc}} \Lambda_{\text{imp}}}{p_{\text{F},e}^2 v_{\text{F},e}}, \quad (2.31)$$

where n_{nuc} is the number density of nuclei, $p_{\text{F},e}$ is the electron Fermi momentum, and $v_{\text{F},e}$ is the electron Fermi velocity. The impurity parameter is given by

$$Q_{\text{imp}} \equiv \frac{1}{n} \sum_i n_i (Z_i - \langle Z \rangle)^2, \quad (2.32)$$

where n_i is the number density of the nuclear species with Z_i number of protons and $\langle Z \rangle$ is the average proton number of the composition. A value of $Q_{\text{imp}} = 0$ implies a pure crust and $Q_{\text{imp}} > 0$ contains impurities. The impurity parameter has been constrained from crust cooling models of quiescent neutron star transients (Brown & Cumming, 2009). For example, Brown & Cumming (2009) find that the quiescent light curve in MXB 1659-29 is best fit with $Q_{\text{imp}} \approx 4$ and the light curve of KS 1731-260 is best fit with $Q_{\text{imp}} \approx 1.5$. The similar Q_{imp} parameters in these sources, despite their different accretion histories, would suggest that accreted material is relatively free of impurities once compressed into the inner crust (as suggested by calculations of nuclear reactions in accreted material done in Section 2.3.2). By contrast, more recently accreted material in the outer crust that has yet to be processed completely by non-equilibrium nuclear reactions has a large impurity parameter. Models of superburst ignition (to be discussed in more detail in Section 5.2.2) need $Q_{\text{imp}} \approx 100$ to have a sufficiently large heat flux into the ocean from crustal heating to ignite superbursts (Cumming et al., 2006).

2.4.2 Inner Crust

In the inner crust the electron thermal conductivity is primarily set by electron-impurity scattering, with scattering frequency (Itoh & Kohyama, 1993; Potekhin et al., 1999)

$$\nu_{eQ} = \frac{4\pi e^4 n_e}{p_{F,e}^2 \nu_{F,e}} \frac{Q_{\text{imp}}}{\langle Z \rangle} \Lambda_{eQ} \quad (2.33)$$

$$\approx 3 \times 10^{18} \text{ s}^{-1} \left[\left(\frac{\rho_{14} Y_e}{0.05} \right)^{1/3} \left(\frac{Q_{\text{imp}} \Lambda_{eQ}}{\langle Z \rangle} \right) \right]. \quad (2.34)$$

scaled to typical values of the inner crust. Here $p_{F,e}$ and $\nu_{F,e}$ are the Fermi momentum and velocity of the electrons, respectively, Λ_{eQ} is the Coulomb logarithm, Y_e is the electron fraction, and $\rho_{14} \equiv \rho/(10^{14} \text{ g cm}^{-3})$. The quantity $Q_{\text{imp}} \Lambda_{eQ}/\langle Z \rangle$ is of order unity in the inner crust. The resulting thermal conductivity is

$$K_e = \frac{\pi}{12} \frac{E_{F,e} k_B^2 T_c}{e^4} \frac{\langle Z \rangle}{Q_{\text{imp}} \Lambda_{eQ}} \approx 4 \times 10^{19} \text{ erg s}^{-1} \text{ cm}^{-1} \text{ K}^{-1} \left[T_8 \left(\frac{\rho_{14} Y_e}{0.05} \right)^{1/3} \frac{\langle Z \rangle}{Q_{\text{imp}} \Lambda_{eQ}} \right], \quad (2.35)$$

where $T_8 \equiv T/(10^8 \text{ K})$.

In the inner crust the temperature is $T \ll 10^9 \text{ K}$ and typically below the critical temperature for neutron superfluidity and the free neutron gas is superfluid. The presence of a neutron superfluid in the neutron star crust is an idea predating the discovery of neutron stars (Migdal, 1959), and there is both theoretical (see, e.g., Gezerlis & Carlson, 2010) and observational evidence (e.g., Shternin et al. 2007) that the neutrons are below their superfluid critical temperature in the deep crust. The critical temperature T_c of the $^1\text{S}_0$ neutron singlet pairing gap is expected to increase from zero near the neutron drip density $\rho \approx 4 \times 10^{11} \text{ g cm}^{-3}$ to a maximum value near $T_c \gtrsim 10^9 \text{ K}$

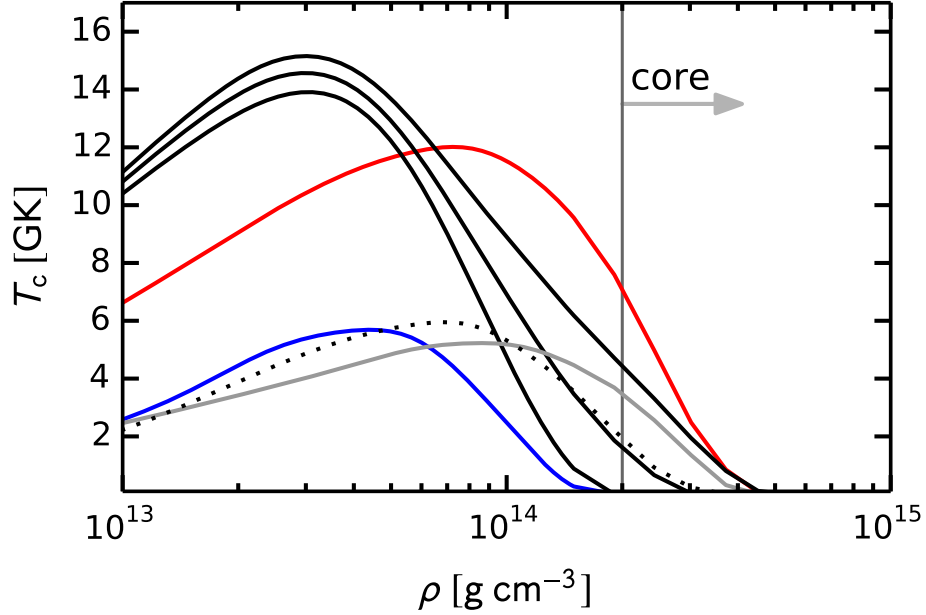


Figure 2.6: Superfluid critical temperature models for the neutron star inner crust as function of mass density. The three solid gray curves are from Gandolfi et al. (2008). The solid black curve is from Schwenk et al. (2003). The dashed black curve is from Gezerlis & Carlson (2011). The red curve is from Chen et al. (1993). The blue curve is from Wambach et al. (1993).

before decreasing again at high mass densities near $\rho \approx 10^{14} \text{ g cm}^{-3}$ where the repulsive core of the neutron interaction removes the tendency to form pairs. Theoretical models for the superfluid critical temperature $T_c(\rho)$ are shown in Figure 2.6.

The density range spanned by the neutron superfluid is an important input for pulsar glitch models; for example, a recent study of pulsar glitches suggests that the neutron superfluid extends from the crust into the core continuously in order to supply adequate inertia for pulsar glitches (Andersson et al., 2012). Furthermore, the neutron superfluid plays a role in relaxation times of pulsar glitches (e.g., Baym et al. 1969; Link 2012) and the dissipation of rotational energy through the coupling of the crust to the neutron superfluid is important for pulsar timing models (e.g., Pines & Alpar 1984).

If the 1S_0 neutron singlet pairing gap closes in the crust, a layer of normal neutrons forms before the crust-core transition. The thermal conductivity of the normal neutrons may become

comparable to the electron thermal conductivity which will impact the cooling of neutron star transients (to be discussed in Chapter 4). The neutron thermal conductivity is

$$K_n = \frac{\pi^2 n_n k_B^2 T}{3m_n^\star \nu_n} \quad (2.36)$$

where m_n^\star is the neutron effective mass and ν_n is the scattering frequency from neutron-neutron and neutron-cluster scattering. We can derive the neutron scattering frequencies in the relaxation time approximation where the scattering frequency can be expressed as (Flowers & Itoh, 1976; Potekhin et al., 1999)

$$\nu_n = \frac{m_n^\star}{12\pi^3 \hbar^3} \frac{n_{\text{ion}}}{n_n} \int_0^{2k_{F,n}} dq q^3 |V(q)|^2 S_\kappa(q), \quad (2.37)$$

where $\hbar q$ is the momentum transfer, $p_{F,n} = \hbar(3\pi^2 n_n)^{1/3} \equiv \hbar k_{F,n}$ is the neutron Fermi momentum, and $V(q)$ is the the Fourier transform of the scattering potential. The scattering medium is described by the structure function

$$S_\kappa(q) = \int_{-\infty}^{\infty} \frac{d\omega}{2\pi} \frac{\hbar\omega}{k_B T} \frac{S(q, \omega)}{1 - \exp(-\hbar\omega/k_B T)} \left[1 + \left(\frac{\hbar\omega}{k_B T} \right)^2 \left(3 \frac{k_{F,n}^2}{q^2} - \frac{1}{2} \right) \right], \quad (2.38)$$

which is written in terms of the dynamical structure factor $S(q, \omega)$.

To describe neutron-nucleus scattering in the inner crust, we assume that the nuclei are spherical and that the surface thickness is negligible compared to the size of the nucleus. Although the nuclei in the pasta phase are certainly non-spherical, a description of scattering in non-spherical geometries is beyond the scope of this work. Under these assumptions, the potential seen by the neutrons can be modeled as a square well with $V(r < R_A) = V_0$, where R_A is the radius of the scattering center. The depth of the potential $V_0 \approx V_{\text{in}} - V_{\text{out}}$, where V_{in} and V_{out} are the neu-

tron single particle potentials inside and outside the scattering structures, respectively. In the pasta phase, the density contrast between the scattering structure and the background rapidly decreases with increasing density, implying a correspondingly rapid decrease in V_0 and reduced neutron scattering.

With the spherical assumption, the effective neutron-nucleus potential in momentum space is

$$V_{n,A}(q) = V_0 \frac{4\pi R_A^3}{3} F_A(qR_A), \quad (2.39)$$

with a form factor (Flowers & Itoh, 1976)

$$F_A(x) = \frac{3[\sin(x) - x \cos(x)]}{x^3}. \quad (2.40)$$

The form factor $F_A \rightarrow 1$ in the limit that momentum transfers are small ($x = qR_A \ll 1$) and is suppressed when momentum transfers are large. Inserting Equation 2.39 into Equation 2.37, we find the neutron-phonon scattering frequency

$$\nu_{n,\text{phn}} = \frac{4}{27\pi} \frac{m_n^* c^2}{\hbar} \frac{n_{\text{ion}}}{n_n} \left(\frac{V_0 R_A}{\hbar c} \right)^2 \Lambda_{n,\text{phn}}, \quad (2.41)$$

where the Coulomb logarithm is given by

$$\Lambda_{n,\text{phn}} = \int_0^{2k_{\text{F},n} R_A} dx x^3 F_A^2(x) S_k^{\text{phn}}(q = x/R_A). \quad (2.42)$$

We evaluate the integral in Equation 2.42 using a Runge-Kutta scheme of order 8(5,3) (Hairer et al., 1993) and fitting formulae for $S_k^{\text{phn}}(q)$ (Potekhin et al. 1999; Equations 21 and 22) that were developed in the context of electron-phonon scattering.

We find the frequency of neutron-impurity scattering using a similar approach. We assume that the impurities are uncorrelated elastic scatterers, and write the scattering frequency as a sum over all impurity species. The neutron-impurity potential for an impurity of species j with radius R_j is

$$V_{n,j} = V_0 \frac{4\pi\bar{R}^3}{3} F_A(q\bar{R}) \left(\frac{R_j^3}{\bar{R}^3} \frac{F_A(qR_j)}{F_A(q\bar{R})} - 1 \right), \quad (2.43)$$

where \bar{R} is the radius of the average ion in the lattice. With this assumption, the dynamical structure factor for impurity scattering is (Flowers & Itoh, 1976)

$$S^{\text{imp}}(q, \omega) = \frac{1}{n_{\text{ion}}} \sum_j 2\pi n_j \delta(\omega), \quad (2.44)$$

where j is the sum over impurity species and n_j is the number density of impurities.

Upon using Equations (2.44) and (2.38) to obtain $S_{\kappa}^{\text{imp}}(q) = \sum_j n_j / n_{\text{ion}}$, and inserting $S_{\kappa}^{\text{imp}}(q)$ and $V_{n,j}$ (Equation 2.43) into Equation (2.37), we find the neutron-impurity scattering frequency

$$\nu_{nQ} = \frac{4}{27\pi} \frac{m_n^* c^2}{\hbar} \frac{n_{\text{ion}}}{n_n} \left(\frac{V_0 \bar{R}}{\hbar c} \right)^2 \Lambda_{nQ} \bar{Q}. \quad (2.45)$$

Here we define the Coulomb logarithm for neutron-impurity scattering,

$$\Lambda_{nQ} = \int_0^{2k_{\text{F},n\bar{R}}} dx x^3 F_A^2(x), \quad (2.46)$$

and the impurity parameter for neutron scattering,

$$\bar{Q} = \frac{1}{\Lambda_{nQ}} \int_0^{2k_{\text{F},n\bar{R}}} dx x^3 F_A^2(x) \sum_j \frac{n_j}{n_{\text{ion}}} \left(\frac{R_j^3}{\bar{R}^3} \frac{F_A(xR_j/\bar{R})}{F_A(x)} - 1 \right)^2. \quad (2.47)$$

For scattering involving momentum transfers $q \lesssim 1/R_j$ the ratio $F_A(qR_j)/F_A(q\bar{R}) \approx 1$. Taking $R_j^3 \propto Z_j$ and $\bar{R}^3 \propto \langle Z \rangle$ then gives $\tilde{Q} \approx Q_{\text{imp}}/\langle Z \rangle^2$ where Q_{imp} (Equation 2.32) is the impurity parameter for electron scattering. The neutron-impurity scattering frequency is therefore

$$\nu_{nQ} \approx \frac{4}{27\pi} \frac{m_n^* c^2}{\hbar} \frac{n_{\text{ion}}}{n_n} \left(\frac{V_0 \bar{R}}{\hbar c} \right)^2 \frac{Q_{\text{imp}}}{\langle Z \rangle^2} \Lambda_{nQ}. \quad (2.48)$$

Since the neutron chemical potentials inside and outside the nucleus are required to be equal in Gibbs equilibrium, we can estimate V_0 as the difference in the single particle kinetic energies inside and outside the nucleus,

$$V_0 \approx \frac{\hbar^2 (3\pi^2 n_{\text{in}})^{2/3}}{2m_n} \left(1 - \left(\frac{n_n}{n_{\text{in}}} \right)^{2/3} \right), \quad (2.49)$$

where n_{in} is the neutron number density inside the nucleus. We take R_A to be the proton radius of the nucleus given by $(4\pi/3)R_A^3 n_{\text{in}} = Z$, where Z is the proton number of the nucleus. We therefore expect that $V_0 R_A / \hbar c \sim O(1)$ in the inner crust. The total scattering frequency is

$$\begin{aligned} \nu_n = \nu_{n,\text{phn}} + \nu_{nQ} &\approx \frac{4}{27\pi} \frac{m_n^* c^2}{\hbar} \frac{n_{\text{ion}}}{n_n} \left(\frac{V_0 R_A}{\hbar c} \right)^2 \left[\Lambda_{n,\text{phn}} + \frac{Q_{\text{imp}}}{\langle Z \rangle^2} \Lambda_{nQ} \right] \\ &= 6.7 \times 10^{20} \text{ s}^{-1} \left(\frac{m_n^*}{m_n} \right) \left(\frac{n_{\text{ion}}/n_n}{0.01} \right) \left(\frac{V_0 R_A}{\hbar c} \right)^2 \left[\Lambda_{n,\text{phn}} + \frac{Q_{\text{imp}}}{\langle Z \rangle^2} \Lambda_{nQ} \right] \end{aligned} \quad (2.50)$$

The ratio of the phonon and impurity scattering frequencies is

$$\frac{\nu_{n,\text{phn}}}{\nu_{nQ}} = \frac{\langle Z \rangle^2}{Q_{\text{imp}}} \frac{\Lambda_{n,\text{phn}}}{\Lambda_{nQ}} \quad (2.51)$$

and is typically of order unity for $Q_{\text{imp}} \simeq 10$.

Scaling the thermal conductivity of normal neutron to typical values in the inner crust,

$$\begin{aligned}
K_n &= \frac{9\pi^3 n_n k_B^2 T}{4 m_n^\star} \frac{\hbar}{m_n^\star c^2} \frac{n_n}{n_{\text{ion}}} \left(\frac{\hbar c}{V_0 R_A} \right)^2 \left[\Lambda_{n,\text{phn}} + \frac{Q_{\text{imp}}}{\langle Z \rangle^2} \Lambda_n Q \right]^{-1} \\
&\approx 3 \times 10^{17} \text{ erg s}^{-1} \text{ cm}^{-1} \text{ K}^{-1} T_8 Y_n \rho_{14} \left(\frac{m_n^\star}{m_n} \right)^{-2} \left(\frac{n_n/n_{\text{ion}}}{100} \right) \\
&\quad \times \left(\frac{\hbar c}{V_0 R_A} \right)^2 \left[\Lambda_{n,\text{phn}} + \frac{Q_{\text{imp}}}{\langle Z \rangle^2} \Lambda_n Q \right]^{-1}. \tag{2.52}
\end{aligned}$$

In this expression $m_n^\star = p_{F,n} [\partial \varepsilon(p) / \partial p]_{p=p_{F,n}}^{-1}$ is the Landau effective mass and $\varepsilon(p)$ is the neutron single particle energy including the rest mass (see, e.g., Baym & Chin, 1976). The dimensionless quantity $V_0 R_A / \hbar c$ is of order unity and measures the strength of the neutron–nucleus interaction; R_A is the typical size of the scattering structure and energy V_0 is the magnitude of the scattering potential.

The specific heat capacity of normal neutrons is

$$\begin{aligned}
C_V^n &= \frac{\pi^2 n_n k_B^2 T}{\rho p_{F,n} v_{F,n}} \\
&\approx 3 \times 10^4 \text{ erg g}^{-1} \text{ K}^{-1} \left[Y_n^{1/3} \rho_{14}^{-2/3} \left(\frac{T_7}{3} \right) \right], \tag{2.53}
\end{aligned}$$

scaled to typical values of the inner crust, where n_n is the number density of normal neutrons, $p_{F,n}$ is the neutron Fermi momentum, and $v_{F,n}$ is the neutron Fermi velocity.

2.4.3 Heat Sources and Sinks

The emissivity terms ϵ_ν and ϵ_{nuc} in Equation 2.25 represent thermal energy loss via neutrinos and thermal energy deposition via nuclear reactions, respectively. During active accretion, heat is deposited by non-equilibrium nuclear reactions (Sato, 1979; Bisnovatyĭ-Kogan & Chechetkin,

1979) which deposit ≈ 0.2 MeV per accreted nucleon in the outer crust (Gupta et al., 2007) and ≈ 1.5 MeV per accreted nucleon in the inner crust (Haensel & Zdunik, 1990, 2003, 2008). When we model the thermal evolution of the crust in neutron star transients in Chapter 4, we parametrize nuclear heating during active accretion rather than resolve individual reaction layers, following the approach of Brown (2000).

We parametrize the heating expected from electron captures in the outer crust by distributing heat over the pressure $P = 7.2 \times 10^{26}$ erg cm $^{-3}$ to $P = 1.3 \times 10^{30}$ erg cm $^{-3}$ such that the total heat deposited is ≈ 0.2 MeV per accreted nucleon. To parametrize pycnonuclear fusion heating in the inner crust we distribute heat over the pressure interval $P = 2.6 \times 10^{30}$ erg cm $^{-3}$ to $P = 1.5 \times 10^{31}$ erg cm $^{-3}$ such that the total heat deposited is ≈ 1.5 MeV per accreted nucleon. In neutron stars that require extra heating to match quiescent temperatures, we include the additional nuclear emissivity of $\epsilon_{\text{nuc}} = \dot{m}Q_{\text{shallow}}$ proportional to the accretion rate \dot{m} , where Q_{shallow} is in MeV per accreted nucleon. For example, the neutron star transient MXB 1659-29 requires $Q_{\text{shallow}} \approx 1$ MeV per accreted nucleon to reproduce quiescent temperatures.

Neutrino cooling in the crust is primarily due to neutrino-pair production. For neutrino losses due to neutrino-pair production we use the neutrino emissivity from Yakovlev et al. (2001) (their Equation 22). At ocean and crust temperatures $T \gtrsim 2 \times 10^9$ K neutrino losses from begin to balance crust heating. For instance, MAXI J0556-332 reaches a nearly maximally hot state where neutrino losses offset the heating from extra shallow heating in the crust (Deibel et al., 2015). In addition, neutrino emission from Urca cycling nuclei pairs (discussed in Chapter 5) limits the ocean and crust temperature to $T \lesssim 8 \times 10^8$ K near the depths inferred for superburst ignition (Deibel et al., 2016).

Chapter 3

Magnetar Starquakes

Magnetars are isolated neutron stars with large magnetic fields between $B_{\text{dip}} \sim 10^{14}\text{--}10^{15}$ G, as determined from their spin periods and spin-down rates assuming a dipole magnetic field¹. Magnetars were initially classified as either Anomalous X-ray Pulsars (AXPs) or Soft Gamma-ray Repeaters (SGRs), as determined by emission in either the soft X-ray or hard X-ray/soft γ -ray, respectively (see Mereghetti (2008) for a review).

Powerful γ -ray flares from some magnetars (Barat et al., 1983) are thought to occur after a reconfiguration of the strong magnetic field fractures the crystalline crust, triggering a powerful burst of energy (Thompson & Duncan, 1995; Schwartz et al., 2005). In this model, crust fracturing not only transports energy into the magnetosphere, where it is reemitted as the giant flare, but energy is also deposited into the rigid crust causing a starquake (Duncan, 1998). If this is indeed the case, then quasi-periodic oscillations (hereafter QPOs) observed in the tail of giant flare emission (Israel et al., 2005; Strohmayer & Watts, 2005; Watts & Strohmayer, 2006) may be interpreted as torsional oscillation modes of the crust during a starquake (Piro, 2005; Strohmayer & Watts, 2006; Samuelsson & Andersson, 2007). Crust oscillations, however, do not reproduce the lowest frequency QPOs (Samuelsson & Andersson, 2007). Alternative theories explain QPOs as amplified core magnetohydrodynamic modes (Glampedakis et al., 2006; Levin, 2006), but these models do not produce the highest frequency QPOs (van Hoven & Levin, 2012).

¹McGill SGR/AXP Online Catalog,
<http://www.physics.mcgill.ca/~pulsar/magnetar/main.html>

Within the pure crust mode paradigm for the observed QPOs, studies of starquakes often assume that superfluid neutrons in the neutron star inner crust (Migdal, 1959; Gezerlis & Carlson, 2010; Shternin et al., 2007; Brown & Cumming, 2009) near the crust-core phase transition eliminate viscous drag (Ruderman, 1968). In this case, QPOs arise from pure crust modes and can therefore constrain crust physics (Steiner & Watts, 2009; Deibel et al., 2014). In particular, as we discuss in this chapter, crust modes constrain the nuclear symmetry energy at mass densities near nuclear saturation. Furthermore, because torsional mode frequencies are sensitive to the crust thickness — which in turn is set by the neutron star’s mass and radius — modeling QPO frequencies constrains the magnetar’s mass and radius.

3.1 A Magnetized Crust

Magnetars are isolated non-accreting neutron stars and it is assumed that their crust composition has not been polluted from the pristine composition frozen in post-supernova. Therefore, the equilibrium crust composition outlined and computed in Chapter 2 will be a sufficient representation of the magnetar’s crust. However, the high magnetic fields of magnetars alter the crust composition at low densities because the electrons become quantized into energy levels above the critical magnetic field (see Equation 3.1). These modifications will alter the energy density contribution from electrons and consequently the nucleus that minimizes the total energy density in the calculation for the equilibrium crust.

3.1.1 Electron Quantization

At the magnetic field strengths inferred for magnetars the ocean and crust composition is altered at low densities by the magnetic field. The electron contribution to the energy density becomes

comparable to the other energy density contributions at low densities when the electron cyclotron energy equals the rest mass energy of the electron, $\hbar\omega_c = m_e c^2$, giving a field

$$B_{\text{crit}} = \frac{m_e^2 c^3}{\hbar e} \approx 4.4 \times 10^{13} \text{ G}, \quad (3.1)$$

and we define the quantity,

$$B_* = B/B_{\text{crit}}, \quad (3.2)$$

which is a convenient quantity when discussing the large magnetic fields of magnetars. In magnetars where the magnetic field is $B \gtrsim B_{\text{crit}}$ we see the composition is altered at low densities, as seen in Table 3.1. When the magnetic field is $B \gg B_{\text{crit}}$ the composition can be altered at densities greater than the neutron-drip point ($\rho \gtrsim \rho_{\text{drip}} \approx 4 \times 10^{11} \text{ g cm}^{-3}$). The electron contribution to the energy density is that of an electron gas embedded in a perpendicular magnetic field $\vec{B} = B\hat{z}$. Following the work of Broderick et al. (2000), the electrons acquire an effective mass, m_e^* , in the presence of the magnetic field

$$m_e^{*2} = m_e^2 + 2 \left(x + \frac{1}{2} - \frac{1}{2} \nu \right) eB, \quad (3.3)$$

where m_e , x , and ν are respectively the electron mass, principal quantum number, and electron spin (Rabi, 1928; Ventura & Potekhin, 2001). The additional term in the electron mass designates the Landau level which is set almost entirely by the strength of the magnetic field. The maximum Landau level is found using the fermi momentum of the electron

$$k_F^2 = E_{F,e}^2 - m_e^{*2}, \quad (3.4)$$

where k_F is the electron Fermi momentum and $E_{F,e}$ is the electron Fermi energy. In the neutron star crust the electrons are degenerate and relativistic, and $E_{F,e} \approx \mu_e \gg m_e c^2$, where μ_e is the chemical potential of electrons. The maximum Landau level is set as the principal quantum number before k_F^2 becomes negative. The fermi momentum can be found by using the known electron number density, $n_e = Zn/A$, and solving for the chemical potential after summing over the total number of Landau levels within the equation

$$n_e = \frac{eB}{2\pi^2} \sum_{\sigma_z} \sum_n k_F. \quad (3.5)$$

Knowing the electron fermi momentum we can easily obtain the electronic contribution to the energy density per baryon,

$$\epsilon_e(Z, A, n; n_e) = \frac{eB}{4\pi^2} \int_0^{k_F} k^2 \sqrt{k^2 + m_e^*{}^2} dk. \quad (3.6)$$

Note that we use the relativistic treatment of electrons because magnetar magnetic field strengths near $B \gtrsim B_{\text{crit}}$ imply that the electrons are relativistic ($\hbar k_{F,e} \gg m_e c^2$).

3.1.2 Composition

Electron quantization in a strong magnetic field ($B \gg B_{\text{crit}}$) alters the energy density of electrons. A change in the electron contribution to the total energy density changes the equilibrium nucleus at a given mass density in the crust. A revised crust composition in various magnetic fields $B \gtrsim B_{\text{crit}}$ are shown in Table 3.1.

The crust composition sets the shear modulus μ , which encodes the crust's response to elastic

Table 3.1: Equilibrium nuclei below the crust-core transition in a magnetized crust.

Nuclei ¹	ρ_{\max} (g cm ⁻³)				
	$B_* = 0$	$B_* = 1$	$B_* = 10$	$B_* = 10^2$	$B_* = 10^3$
${}^{64}_{28}\text{Ni}$	2.23×10^8		2.33×10^8	1.63×10^9	1.75×10^{10}
${}^{66}_{28}\text{Ni}$	1.37×10^9		1.40×10^9	2.92×10^9	2.71×10^{10}
${}^{84}_{34}\text{Se}$	5.66×10^9			4.87×10^9	5.29×10^{10}
${}^{82}_{32}\text{Ge}$	1.73×10^{10}			1.69×10^{10}	7.62×10^{10}
${}^{80}_{30}\text{Zn}$	3.99×10^{10}			3.94×10^{10}	1.01×10^{11}
${}^{78}_{28}\text{Ni}$	1.56×10^{11}			1.57×10^{11}	1.61×10^{11}
${}^{76}_{26}\text{Fe}$	1.86×10^{11}			1.85×10^{11}	1.76×10^{11}
${}^{122}_{40}\text{Zr}$	2.51×10^{11}			2.52×10^{11}	1.98×10^{11}
${}^{120}_{38}\text{Sr}$	3.54×10^{11}			3.54×10^{11}	4.04×10^{11}
${}^{118}_{36}\text{Kr}$	5.17×10^{11}			5.15×10^{11}	5.77×10^{11}
${}^{116}_{34}\text{Se}$	8.11×10^{11}			8.13×10^{11}	8.56×10^{11}
${}^{114}_{32}\text{Ge}$	2.35×10^{12}				2.25×10^{12}
${}^{112}_{30}\text{Zn}$	3.94×10^{12}				4.02×10^{12}
${}^{110}_{28}\text{Ni}$	8.64×10^{12}				8.65×10^{12}
${}^{166}_{40}\text{Zr}$	1.07×10^{13}				1.08×10^{13}

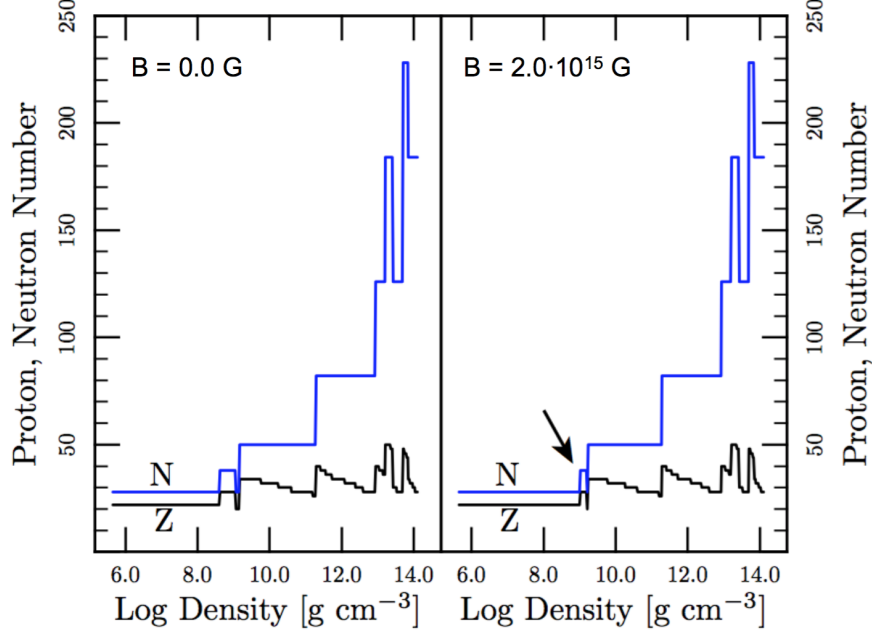


Figure 3.1: Equilibrium composition of the neutron star crust in a strong magnetic field $B = 2 \times 10^{15}$ G. (*Left panel*): Equilibrium crust composition without a magnetic field. (*Right panel*): The black arrow indicates the first transition between equilibrium nuclei, which has moved to a greater depth as a consequence of the strong magnetic field when compared to the left panel.

stresses. We use the shear modulus of a body-centered cubic lattice (Strohmayer et al., 1991),

$$\mu = \frac{0.1194\Gamma}{1 + 0.595(\Gamma_0/\Gamma)^2} n_i k_B T, \quad (3.7)$$

where Γ is the plasma coupling parameter of the crust (Equation 2.4) and $\Gamma_0 \equiv 175$ is the melting point of the crust. The speed of shear waves in the crust $v_s = \sqrt{\mu/\rho}$ is set by the shear modulus.

3.2 Crust Torsional Modes

Magnetar giant flares have luminosities $L_{\text{peak}} \sim 10^{44} - 10^{47}$ ergs s^{-1} (Barat et al., 1983). Operating under the assumption that a fraction of the energy is transported to the crust, the crust will receive a strong impulse that will drive oscillation modes, shown schematically in Figure 3.2. The intense

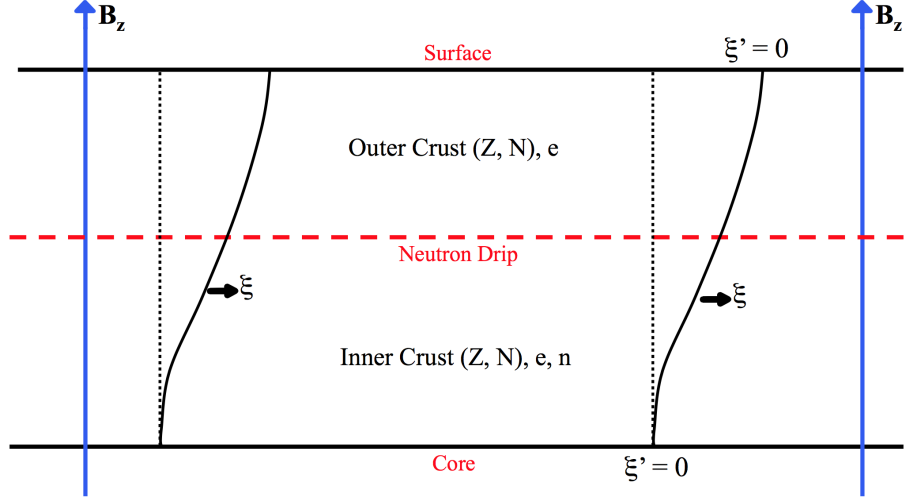


Figure 3.2: Schematic of a torsional oscillation mode in the magnetar crust. Crust oscillation frequencies are found using Equation 3.14, using the boundary condition $\xi' = 0$ (loss of traction) at the base and top of the crust.

gravity and vertical stratification confine the modes to the axial direction and the mode spectrum can be well described by a differential equation of motion for axial perturbations. What arises is an eigenvalue problem, where the solution of the differential equation are the eigenmodes of the crust. To produce the most realistic solutions we add general relativistic effects and magnetic effects to our differential equation for torsional oscillations.

The axial perturbation equation, which describes axial torsional oscillation modes, is derived by Schumaker & Thorne (1983) and applied to modern neutron star models in Samuelsson & Andersson (2007). Here we follow the formalism of Samuelsson & Andersson (2007) when describing the axial perturbation equation in the absence of a magnetic field, which takes the form

$$\xi'' + F'\xi' + G\xi = 0, \quad (3.8)$$

where ξ is an axial perturbation and primes indicate derivatives with respect to the radial coordinate. The functions F and G depend on the elastic properties of the crust and the space-time

metric,

$$F' = \left\{ \ln \left[r^4 e^{\nu-\lambda} (\varepsilon + p_t) v_r^2 \right] \right\}' , \quad (3.9)$$

and

$$G = \frac{e^{2\lambda}}{v_r^2} \left[e^{-2\nu} \omega^2 - \frac{v_t^2 (\ell - 1) (\ell + 2)}{r^2} \right] , \quad (3.10)$$

where r is the radial coordinate, ε is the energy density, p is the pressure, ω is the oscillation angular frequency, and l is the angular wave number. Here we use a static, spherically symmetric space-time metric,

$$ds^2 = -e^{2\nu} dt^2 + e^{2\lambda} dr^2 + r^2 (d\theta^2 + \sin^2 \theta d\phi^2) , \quad (3.11)$$

and the perturbation equation may be expressed as (Samuelsson & Andersson, 2007),

$$\xi'' + \left\{ \ln \left[r^4 e^{\nu-\lambda} (\varepsilon + p_t) v_r^2 \right] \right\}' \xi' + \frac{e^{2\lambda}}{v_r^2} \left[e^{-2\nu} \omega^2 - \frac{v_t^2 (\ell - 1) (\ell + 2)}{r^2} \right] \xi = 0 , \quad (3.12)$$

where $e^{2\lambda} \approx e^{-2\nu} = (1 - 2M(r)/r)^{-1}$ in the crust. The large magnetic fields in magnetars drive magnetic waves, or Alfvén waves, which can significantly alter crust dynamics where $v_A > v_s$ (Piro, 2005). This is the case for the magnetic field of SGR 1806-20 ($B = 2.4 \times 10^{15}$ G) where $v_A \gg v_s$ in the outer crust, as seen in Figure 3.3. Therefore, we add corrections for a finite Alfvén velocity to the perturbation equation. The Newtonian expression for axial perturbations with a magnetic field are (Piro, 2005; Steiner & Watts, 2009),

$$\frac{(\mu \xi')'}{\rho} + v_A^2 \xi'' + \left[\omega^2 \left(1 + \frac{v_A^2}{c^2} \right) - \frac{(l^2 + l - 2)\mu}{\rho r^2} \right] \xi = 0 , \quad (3.13)$$

where $v_A = B / \sqrt{4\pi\rho_i}$. Combining the general relativistic expression and the Newtonian magnetic

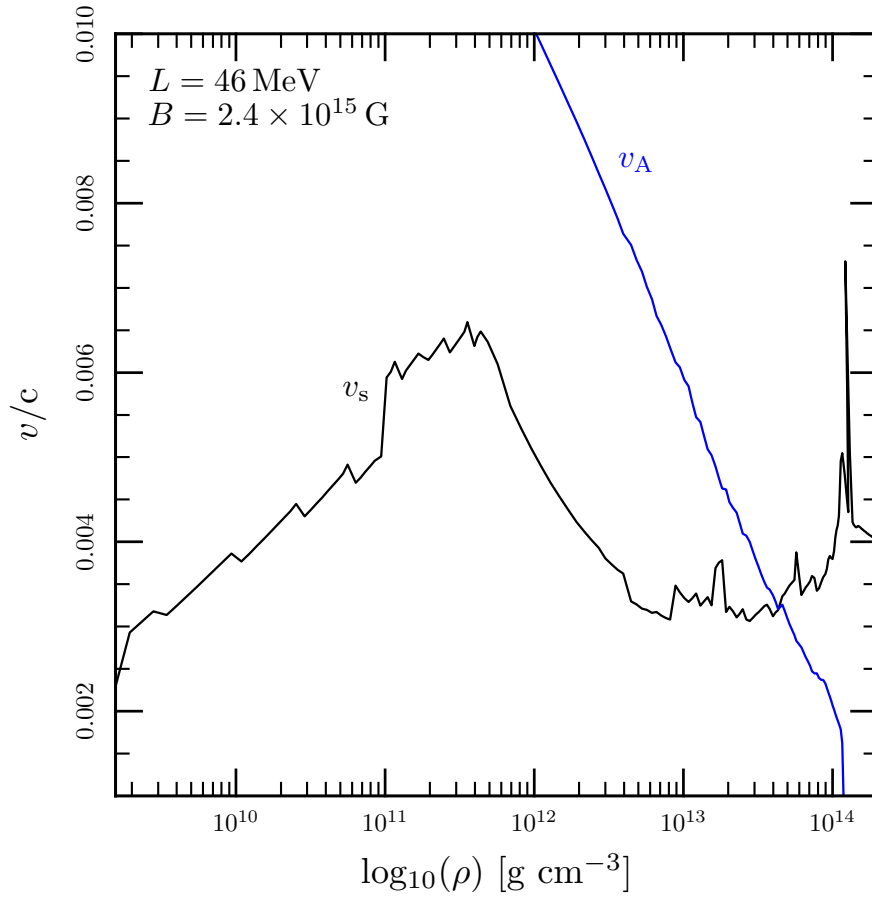


Figure 3.3: Alfvén velocity (blue curve) and shear velocity (black curve) in the crust as a function of mass density. The composition is that of a $1.4 M_{\odot}$ neutron star using the SLy4 crust EOS.

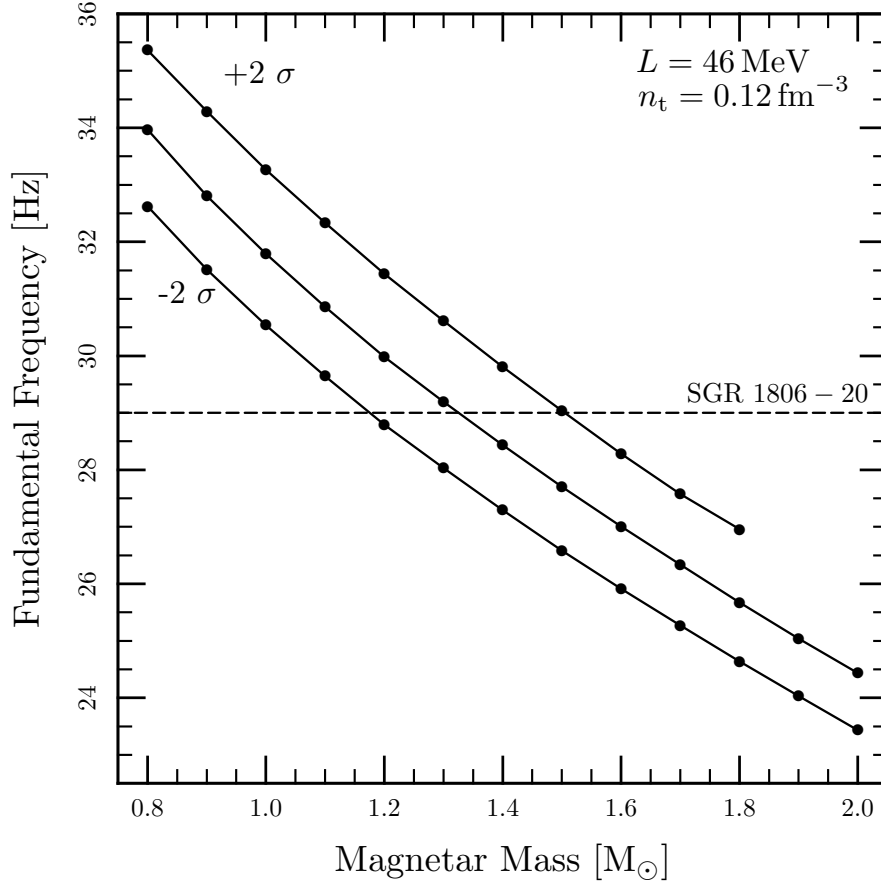


Figure 3.4: Frequency of the fundamental $l = 2$ mode as a function of the magnetar mass for the core EOS probability distribution (centroid and $\pm 2\sigma$) from Steiner et al. (2013) and an SLy4 crust EOS. The dashed black line indicates the observed 29 Hz QPO of SGR 1806-20. The frequencies are evaluated for a crust-core transition density of 0.12 fm^{-3} with $B = 0 \text{ G}$.

expression,

$$(v_s^2 + v_A^2)\xi'' + v_s^2 \frac{d}{dr} \left\{ \ln \left[r^4 e^{\nu-\lambda} (\varepsilon + p) v_s^2 \right] \right\} \xi' + e^{2\lambda} \left[e^{-2\nu} \omega^2 \left(1 + \frac{v_A^2}{c^2} \right) - \frac{(l^2 + l - 2) v_s^2}{r^2} \right] \xi = 0. \quad (3.14)$$

In the limit that $B \rightarrow 0$, Equation 3.12 is recovered. In the limit that $e^{2\lambda} \rightarrow 1$, $e^{-2\nu} \rightarrow 1$, the Newtonian expression (Equation 3.13) is recovered. A full derivation of the perturbation equations can be found in Appendix 6.

In this study, we calculate crust modes for several crust equations of state. The modes will

differ between crust equations of state due to a changing shear modulus and crust thickness. We integrate Equation 3.14 over the crust, that is, from $r = R_{\text{core}}$ the core radius to the top of the crust $r = R_{175}$ where the crust melts where $\Gamma = 175$, given by the ocean-crust transition density in 2.5. The traction ξ' vanishes at the top of the crust where pressure vanishes, and we also assume neutron superfluidity at the crust-core interface causes a loss of traction there by eliminating viscous drag (Ruderman, 1968).

3.3 Constraints from Observations

Each neutron star mass and radius give a unique crust thickness and therefore a unique set of torsional crust modes. Because of the orthogonal behavior of fundamental and overtone crust modes, matching the observed fundamental and harmonic modes from a magnetar can only be achieved by one mass and radius combination for a given equation of state, an example is shown in Figure 3.4. Observations of photosphere radius expansion bursts and low-mass X-ray binaries give empirical constraints on the neutron star core equation of state (Steiner et al., 2010; Steiner et al., 2013). We investigate which core equation of state contains crusts that host torsional modes at similar frequencies to those observed in giant flare QPOs. In particular, we examine the giant flares from the magnetars SGR 1806-20 (Strohmayer & Watts, 2006; Watts & Strohmayer, 2006) and SGR 1900+14 (Strohmayer & Watts, 2005).

3.3.1 Nuclear Symmetry Energy

The different core equations of state from Steiner et al. (2013) are characterized by different degrees of stiffness of the nuclear symmetry energy. The nuclear symmetry energy, $S(n)$, is defined as the energy cost from departing from neutron-proton symmetric matter. Equations of state with

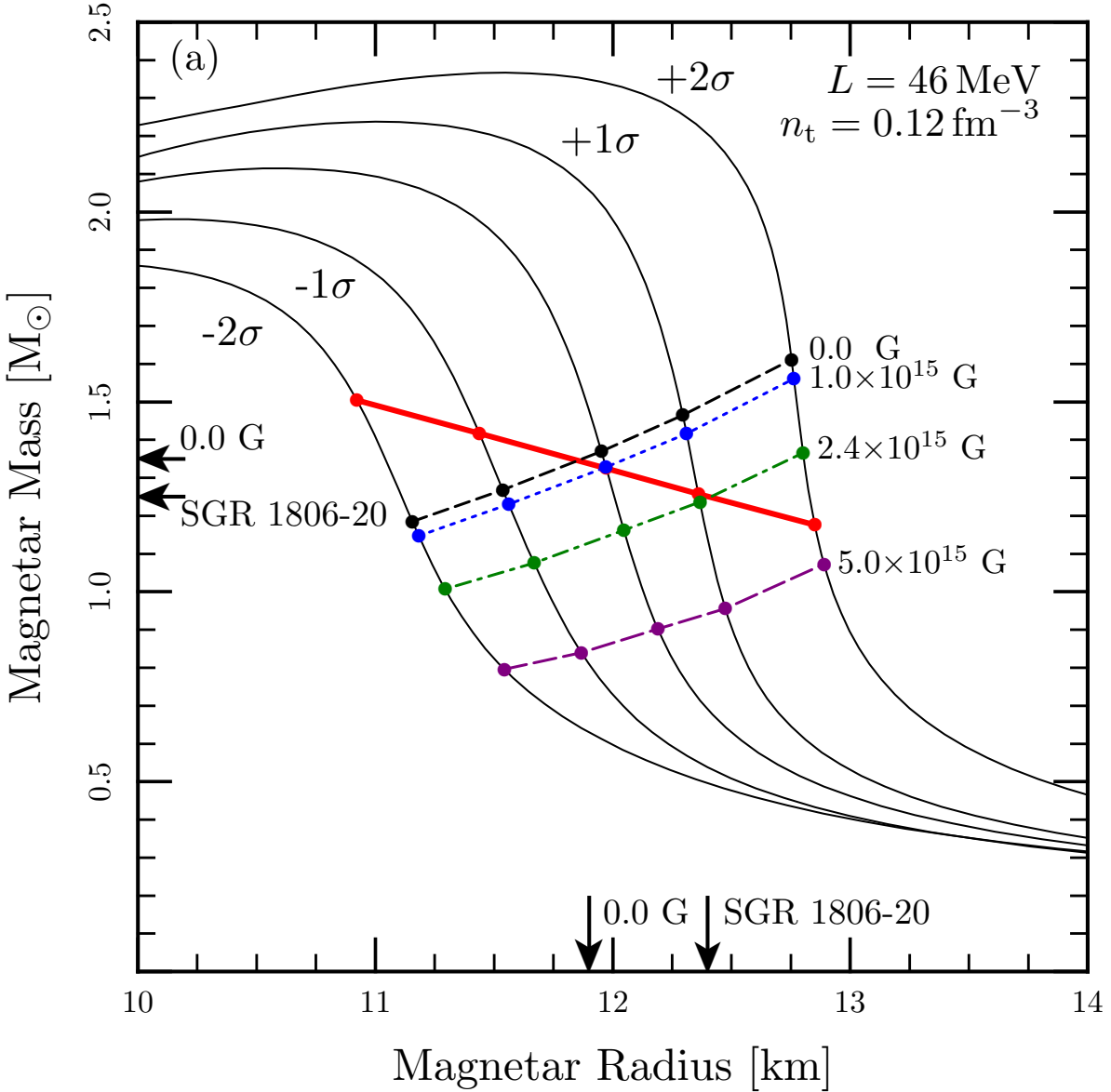


Figure 3.5: Magnetar mass as a function of radius for the core EOS probability distribution from Steiner et al. (2013). Frequencies are evaluated using the SLy4 crust EOS ($L = 46 \text{ MeV}$) for $n_t = 0.12 \text{ fm}^{-3}$. The thick red solid line indicates masses and radii for which the fundamental mode has a frequency of 29 Hz in the case of SLy4 and 18 Hz in the case of Rs. The black short-dashed line indicates masses and radii for a 626 Hz harmonic mode and $B = 0 \text{ G}$. Masses and radii from 626 Hz harmonic modes with magnetized crusts are labeled accordingly. Arrows indicate masses and radii that match both the fundamental and the harmonic modes for the field-free case and the case with the magnetic field of SGR 1806-20 ($B = 2.4 \times 10^{15} \text{ G}$).

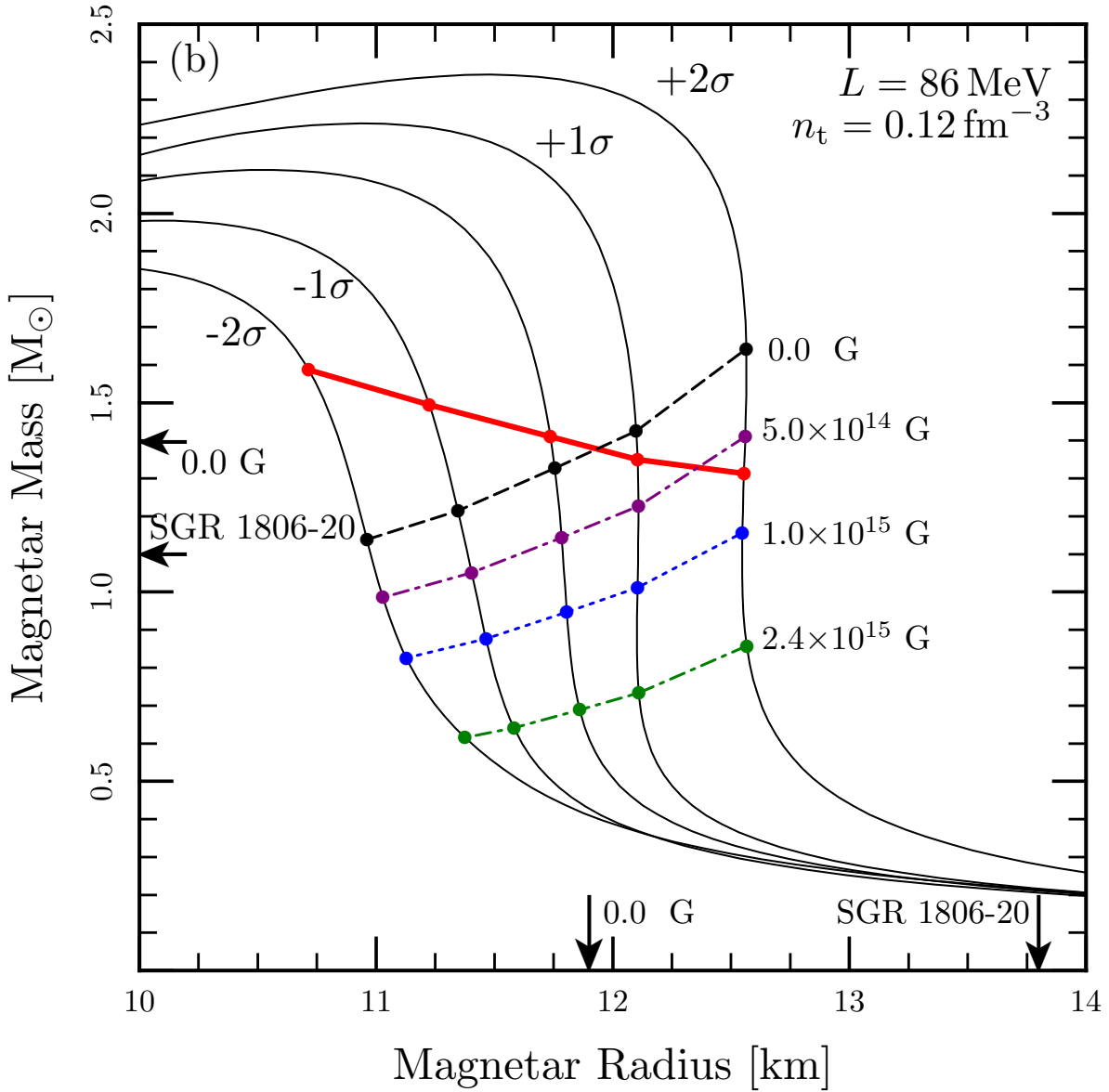


Figure 3.6: Magnetar mass as a function of radius for the core EOS probability distribution from Steiner et al. (2013). Frequencies are evaluated using the Rs crust EOS ($L = 86 \text{ MeV}$) for $n_t = 0.12 \text{ fm}^{-3}$. The thick red solid line indicates masses and radii for which the fundamental mode has a frequency of 29 Hz in the case of SLy4 and 18 Hz in the case of Rs. The black short-dashed line indicates masses and radii for a 626 Hz harmonic mode and $B = 0 \text{ G}$. Masses and radii from 626 Hz harmonic modes with magnetized crusts are labeled accordingly. Arrows indicate masses and radii that match both the fundamental and the harmonic modes for the field-free case and the case with the magnetic field of SGR 1806-20 ($B = 2.4 \times 10^{15} \text{ G}$).

different values of the symmetry energy will have varying degrees of stiffness/softness near the nuclear saturation point. The degree of stiffness is determined by the first derivative of the symmetry energy at nuclear saturation, $L \equiv 3n_0 (\partial S / \partial n)_{n=n_0}$, where $n_0 = 0.16 \text{ fm}^{-3}$. Different values for L lead to different mass-radius relations for the neutron star. As a result, studies that model magnetar QPOs as torsional oscillations of the crust can constrain the nuclear symmetry energy (Steiner & Watts, 2009; Sotani et al., 2012, 2013b; Deibel et al., 2014; Iida & Oyamatsu, 2014; Sotani et al., 2015).

Magnetar masses and radii that support crust frequencies consistent with observed QPOs can be seen in Figures 3.5 and 3.6 for the SLy4 crust equation of state with $L = 46 \text{ MeV}$ and the Rs equation of state with $L = 86 \text{ MeV}$, respectively. Furthermore, two magnetic fields, $B = 0$ and $2.4 \times 10^{15} \text{ G}$ — the inferred dipole magnetic field of SGR 1806-20 — are tested to illustrate the impact of the magnetic field on determining masses and radii with this method. Both values of L give magnetar masses and radii that support crust modes consistent with observed QPOs. A softer equation of state with $L = 46 \text{ MeV}$, however, finds magnetar masses and radii more consistent with the best fits from other empirical constraints from Steiner et al. (2013), when a realistic $2.4 \times 10^{15} \text{ G}$ magnetic field is included in the crust oscillation calculation. Although an equation of state with $L = 86 \text{ MeV}$ may reproduce the observed oscillations with a realistic magnetic field, it requires magnetar masses and radii well outside the 2σ boundaries from empirical constraints.

3.3.2 Neutron Entrainment

A fraction of the quasi-free neutron gas in the inner crust may be entrained by the nuclear lattice during a crust oscillation (Chamel et al., 2013a; Chamel, 2013). If this is the case, an axial perturbation will move more mass and the shear velocity of crust oscillations will decrease. This will in turn alter the oscillation frequencies of the crust (Sotani et al., 2013a). The impact of neutron

entrainment on fundamental and overtone crust frequencies can be seen in Figures 3.7 and 3.8 for the SLy4 crust equation of state with $L = 46$ MeV and the Rs equation of state, respectively. Here f_{ent} indicates the fraction of quasi-free neutrons entrained by the crust lattice during an oscillation.

We find that the fraction of entrained neutrons has a negligible effect on the harmonic modes of the crust because harmonic mode energy is uniformly distributed throughout the entire crust (Piro, 2005). The fundamental mode frequency, however, is significantly altered by neutron entrainment, likely because the fundamental mode's energy is concentrated in the deepest part of the crust. Using the SLy4 equation of state, entrainment fractions $f_{\text{ent}} \gtrsim 0.75$ are needed to have predicted crust modes match observed QPOs in SGR 1806-20, as can be seen in Figure 3.7. Entrainment fractions $f_{\text{ent}} \lesssim 0.75$ require larger magnetar masses and radii that are outside of the best fits from empirical constraints from observations of PREs and LMXBs (Steiner et al., 2013). For the Rs equation of state, low entrainment fractions $f_{\text{ent}} \lesssim 0.3$ are preferred, as can be seen in Figure 3.8. Note that values of $f_{\text{ent}} \approx 0.35 - 0.90$ have been suggested by a study of Bragg scattering with the crust's crystal lattice (Chamel et al., 2013b).

Generally, the degree of neutron entrainment alters fundamental and harmonic crust modes by changing the shear velocity in the crust. Crust equations of state with larger values of L have smaller fundamental mode frequencies; a similar result was found by Sotani et al. (2013a). Furthermore, these authors also find that a higher entrainment fraction decreases fundamental mode frequencies (note that $N_s/N_d = 1 - f_{\text{ent}}$ in the notation of Sotani et al. 2010). Our results are only for equations of state fit to observations of neutron stars (Steiner et al., 2013) and we can not fully determine the correlation of L and f_{ent} using our equations of state with discrete L values.

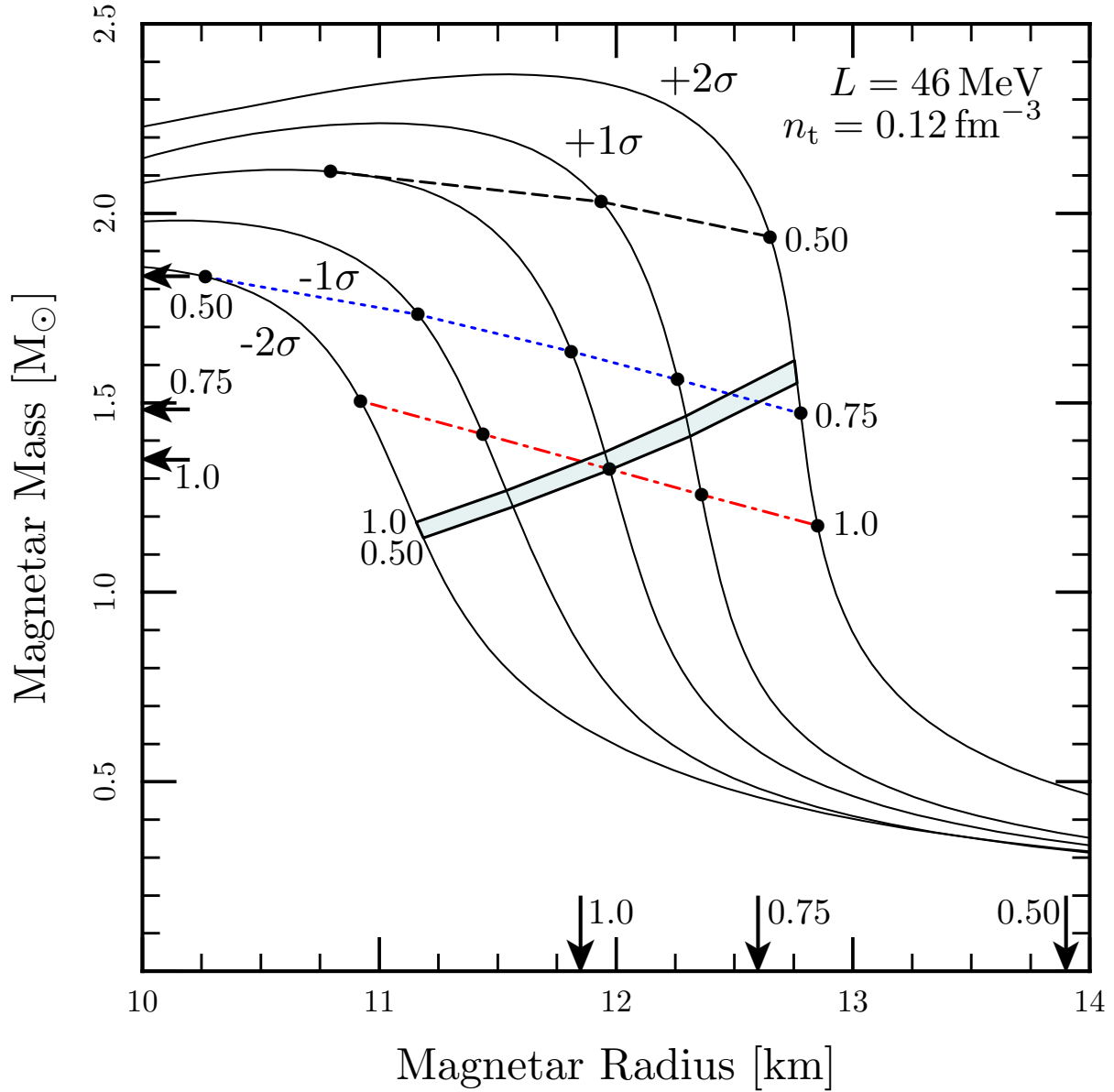


Figure 3.7: Magnetar mass as a function of radius for EOS probability distribution from Steiner et al. (2013). Frequencies are evaluated using the SLy4 crust EOS with $B = 0 \text{ G}$ and $n_t = 0.12 \text{ fm}^{-3}$. The red dot-dashed, blue dotted, and black dashed lines indicate masses and radii from fundamental modes of frequency 29 Hz for different free neutron entrainment fractions f_{ent} . The shaded band indicates masses and radii from 626 Hz harmonic modes as f_{ent} is varied from 0.50 to 1.0. Arrows indicate the masses and radii that match both the fundamental and the harmonic modes for $f_{\text{ent}} = 1.0, 0.75, \text{ and } 0.50$.

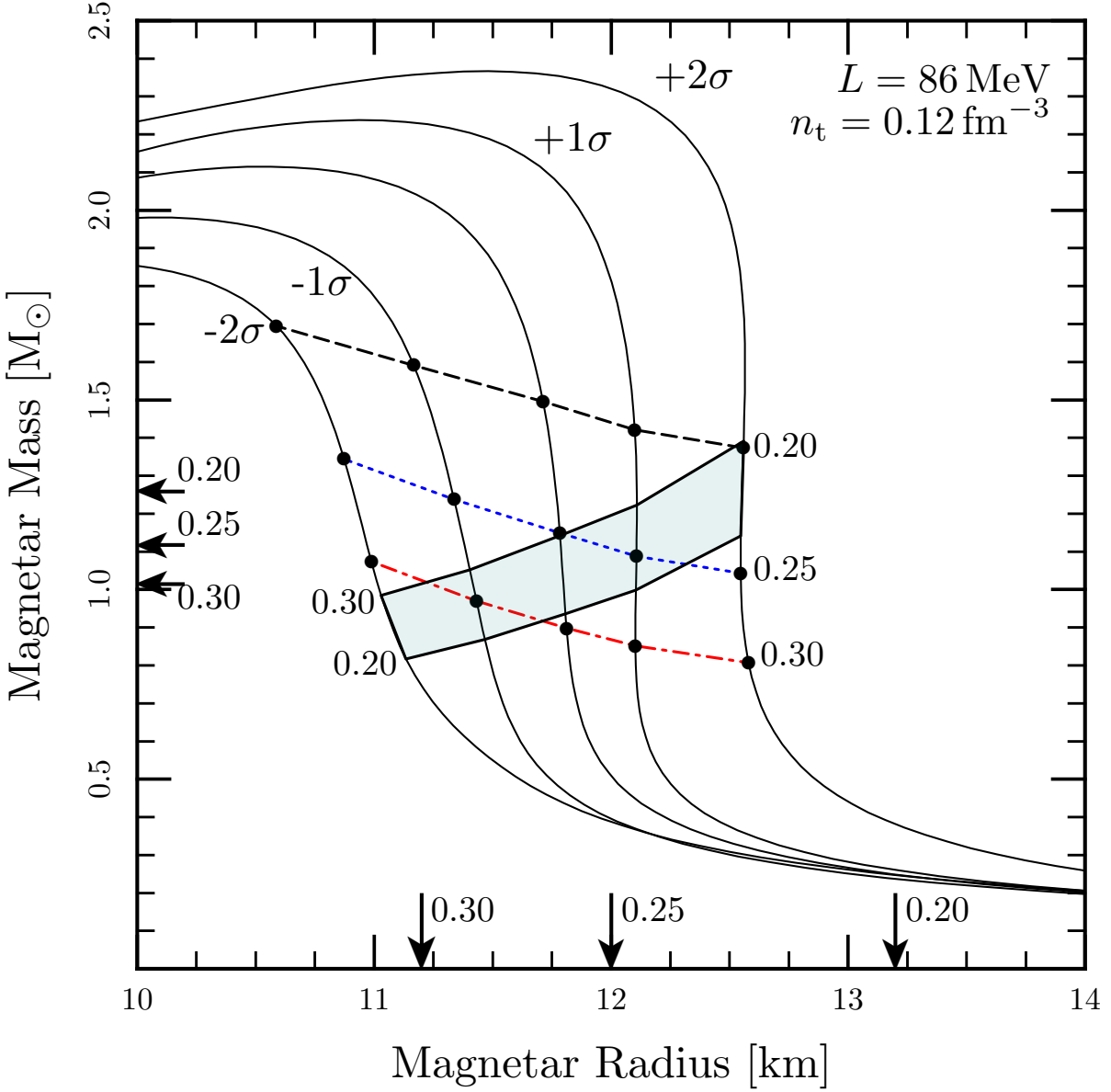


Figure 3.8: The same as Fig. 3.7, but for the Rs crust EOS with $B = 0 \text{ G}$. Here the free neutron entrapment fraction f_{ent} is varied from 0.20 to 0.30, with f_{ent} labeled next to the corresponding curves. The red dot-dashed, blue dotted, and black dashed lines indicate masses and radii from the 29 Hz fundamental mode. The shaded band indicates masses and radii from the 626 Hz harmonic mode. Arrows indicate the masses and radii for $f_{\text{ent}} = 0.30$, 0.25, and 0.20 that match both the fundamental and harmonic modes.

3.3.3 Crust-core Transition Depth

The crust's harmonic frequencies are sensitive to the location of the crust-core transition. Harmonic crust modes scale with the crust thickness and therefore a change in the depth of the crust-core transition will change the crust thickness and harmonic mode frequencies (Deibel et al., 2014). The pressure of the crust-core transition is unknown (Newton et al., 2013).

To investigate the impact of the crust-core transition density on mode frequencies, we test the crust-core transition density values $n_t = 0.08$ and 0.12 fm^{-3} to represent the range of values obtained in Oyamatsu & Iida (2007). The impact of the crust-core transition density on crust fundamental and overtone modes can be seen by comparing Figures 3.5 and 3.9.

For a crust-core transition density of $n_t = 0.12 \text{ fm}^{-3}$, crust oscillation frequencies match observed QPOs for SGR 1806-20 for a magnetar mass $M = 1.25 M_\odot$ and radius $R = 12.4 \text{ km}$. A shallow crust-core transition at $n_t = 0.08 \text{ fm}^{-3}$ does not give a mass and radius consistent with constraints from observations of low-mass X-ray binaries (Steiner et al., 2013), requiring a magnetar mass $M = 0.96 M_\odot$ and radius $R = 13.5 \text{ km}$, as can be seen in Figure 3.9. A small magnetar mass and large magnetar radius is also needed in the case of the Rs equation of state with $n_t = 0.12 \text{ fm}^{-3}$. For this equation of state, predicted crust oscillations match observed QPOs for a magnetar mass $M = 1.10 M_\odot$ and radius $R = 13.8 \text{ km}$, as can be seen in Figure 3.6.

3.3.4 Crust Magnetic Field

In crust mode calculations at $B = 0 \text{ G}$ we assume that the crust thickness remains constant (i.e., $R_{\text{crust}} - R_{\text{core}} = \Delta R$ is constant). In large magnetic fields $B \gg B_{\text{crit}}$ the crust thickness decreases with increasing magnetic field because the melting point (Equation 2.4) moves to greater depths. Furthermore, the magnetic field alters the composition, as seen in Table 3.1, which alters the shear

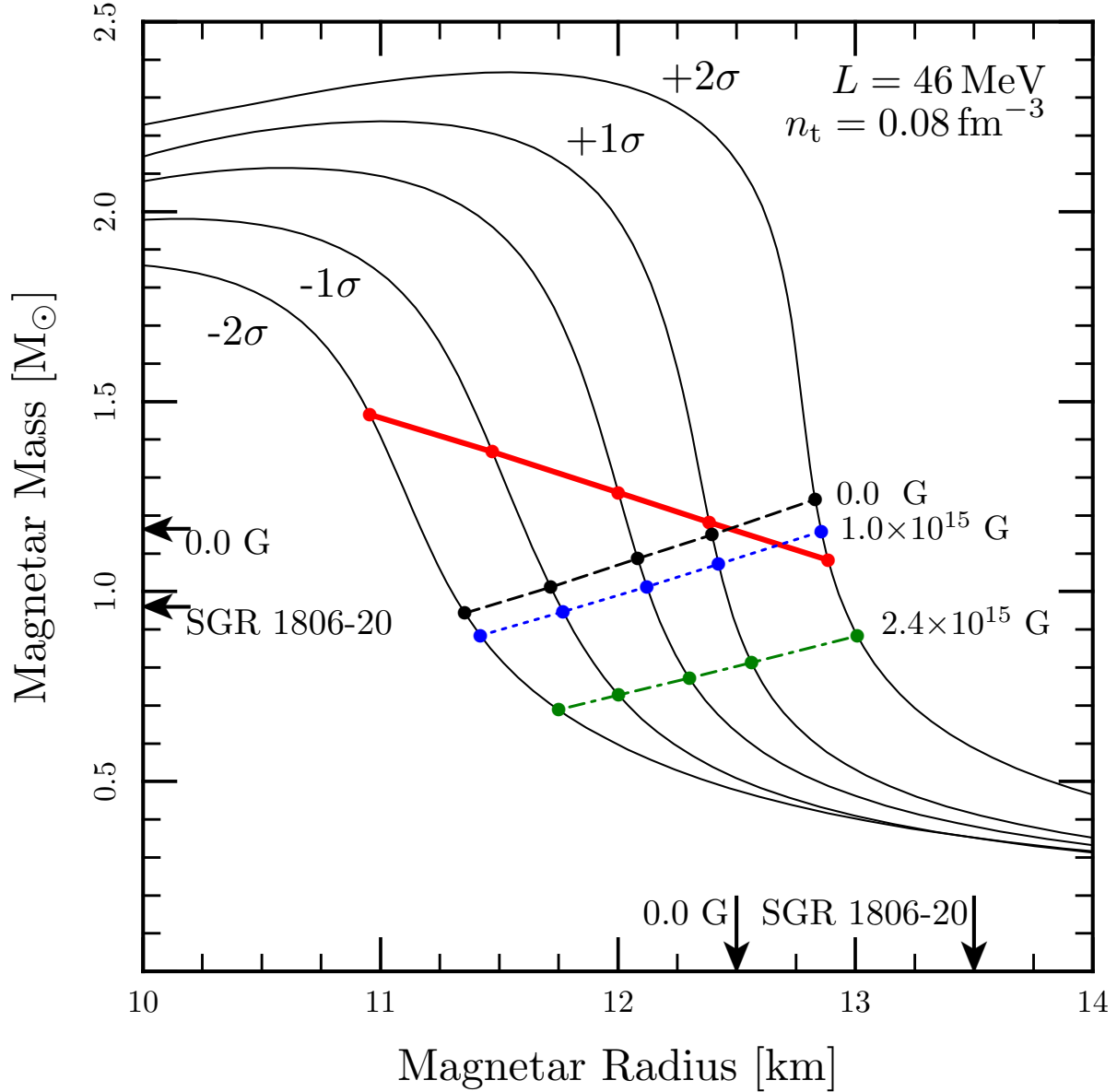


Figure 3.9: The same as Fig. 3.5, but for the SLy4 crust EOS with $n_t = 0.08$ fm $^{-3}$. The thick red solid line indicates masses and radii determined from a fundamental mode of 29 Hz. Masses and radii from harmonic modes with magnetized crusts are labeled accordingly. Arrows indicate masses and radii that match both the fundamental and the harmonic modes for the field-free case and the case with the magnetic field of SGR 1806-20 ($B = 2.4 \times 10^{15}$ G).

modulus. We find that large magnetic fields, and the resulting decrease in crust thickness and change in composition, have a negligible effect on crust fundamental modes, but may significantly impact crust harmonic modes.

The difference between crust frequencies in a crust with a magnetic field of $B = 0\text{ G}$ and $B = 2.4 \times 10^{15}\text{ G}$ can be seen in Figures 3.5 and 3.6. The fundamental crust mode for both crust magnetic fields are identical — similar to the results found by Nandi et al. (2012). The fundamental mode energy is concentrated at the base of the crust (Piro, 2005) where the Alfvén velocity is small compared to the shear velocity and the fundamental mode frequency is mostly determined by the radius of the neutron star (i.e., our choice of equation of state). Harmonic modes have their energy spread over the crust and are sensitive to the Alfvén velocity at lower densities, which is large compared to the shear velocity for the magnetic fields examined here, as can be seen in Figure 3.3. Therefore, harmonic mode frequencies are greatly impacted by the choice of magnetic field; the SLy4 equation of state requires $B \lesssim 5 \times 10^{15}\text{ G}$ and the Rs equation of state requires $B \lesssim 10^{15}\text{ G}$ to have magnetar masses and radii consistent with predictions from low-mass X-ray binaries (Steiner et al., 2013).

The sensitivity of the harmonic mode to the crust magnetic field is worthy of note. If observed QPOs are indeed crust oscillation modes, crust magnetic fields must not be much greater than inferred dipole magnetic fields, otherwise QPOs can only be matched by magnetar masses and radii that are inconsistent with observations of PREs and LMXBs (Steiner et al., 2013). In order to match QPOs with smaller magnetar radii, for instance $R < 11.1\text{ km}$ as found by Guillot et al. (2013), requires larger values of L and f_{ent} .

Chapter 4

Neutron Star Transient Thermal Evolution

In this chapter, we explore the thermal evolution of a neutron star transient's outer layers during and after an accretion outburst. Accretion outbursts have been observed for many neutron stars in low-mass X-ray binaries (see Degenaar et al. (2015) for a summary). Accumulated accreted material compresses existing envelope material deeper in the neutron star. Material compressed into the neutron star crust induces non-equilibrium reactions (Bisnovatyĭ-Kogan & Chechetkin, 1979; Sato, 1979) that deposit $\approx 1\text{--}2$ MeV per accreted nucleon of heat (Haensel & Zdunik, 1990, 2003; Gupta et al., 2007; Haensel & Zdunik, 2008). The neutron star enters quiescence when accretion halts and the neutron star's outer layers begin to cool back to thermal equilibrium with the core. The quiescent emission of the neutron star is powered by the thermal emission from the neutron star surface (Rutledge et al., 2002) as a portion of heat deposited during outburst diffuses toward the surface. This thermal evolution model can be understood qualitatively as a cooling slab (Section 4.1).

The cooling slab model can successfully explain cooling neutron star transients in quiescence once realistic microphysics for the neutron star crust are included (Section 4.2). We apply the thermal evolution model to examine the thermal evolution of the hottest neutron star transient observed to date, MAXI J0556-332 (Matsumura et al., 2011; Homan et al., 2011; Sugizaki et al., 2013; Homan et al., 2014), in Section 4.2.1. The high temperature reached in the outer layers of MAXI J0556-332 make it an interesting test case for thermal evolution models and reveals heating anomalies in the outer crust. In Section 4.3 we apply the thermal evolution model to the Z-source

transients — which trace out a distinctive “Z” shape in the X-ray color-color diagram (Hasinger & van der Klis, 1989) — to create an observational test for the presence of g -modes in the neutron star’s ocean. Finally, in Section 4.4, we use the late-time cooling of transients to examine the thermal properties of the deepest regions of the inner crust near the crust-core transition.

4.1 A Cooling Slab

During an accretion outburst, heat is deposited in the neutron star’s outer layers by nuclear reactions which brings the neutron star’s outer layers out of thermal equilibrium with the core. Given the length of an observed outburst we can predict the temperature of the neutron star at the outset of quiescence by following the time-dependent thermal diffusion through the neutron star’s outer layers. We model the thermal evolution of the crust during outburst and quiescence by constructing a cooling slab that follows the heat flux across the entire crust. The heat flux can be described by Fick’s Law

$$F = -K\nabla T , \tag{4.1}$$

where F is the heat flux, K is the thermal conductivity, and T is the temperature. The divergence of the heat flux describes the change in local temperature as a function of time, that is, the time-dependent thermal diffusion. The thermal diffusion equation can be written as

$$\rho C \frac{dT}{dt} = \nabla \cdot (K \cdot \nabla T) , \tag{4.2}$$

where ρ is the mass density, C is the specific heat per unit mass, and T is the local temperature. In

one dimension, the thermal evolution is described by

$$\rho C \frac{dT}{dt} = \frac{\partial}{\partial x} \cdot \left(K \cdot \frac{\partial T}{\partial x} \right), \quad (4.3)$$

where x is the spatial coordinate. This expression is generically the diffusion equation in one dimension,

$$\frac{du}{dt} = \frac{\partial}{\partial x} \left(D(u(x), x) \frac{\partial u}{\partial x} \right) = \frac{\partial D(u(x), x)}{\partial u} \left(\frac{\partial u}{\partial x} \right)^2 + D(u(x), x) \frac{\partial^2 u}{\partial x^2}, \quad (4.4)$$

which can be finite differenced depending on the diffusion coefficients dependence on u . Advancing the solution for u with time can be achieved using the method of lines, which can be found in Press et al. (2007). This method involves integrating the system of ordinary differential equations formed by finite differencing the right hand side of Equation 4.4. Integrating the resulting equation with respect to time for each zone's set of ordinary differential equations gives the solution for u at the next time step for that zone.

In the case of our cooling slab model of the neutron star crust, u represents the crust temperature T and for our spatial coordinate x we choose the mass density in the crust ρ . Then, the diffusivity D is

$$D(\rho) = \frac{K}{\rho C_V}, \quad (4.5)$$

where the thermal conductivity $K \approx K_e$ throughout the ocean and crust because electron conduction is the primary means of thermal transport.

Scaling to typical values of the inner crust, where electron-impurity scattering sets the thermal conductivity of electrons, gives

$$D \approx 4 \text{ cm}^2 \text{ s}^{-1} \left(\frac{Y_e}{0.05 Y_n} \right)^{1/3} \left(\frac{\langle Z \rangle}{Q_{\text{imp}} \Lambda_{eQ}} \right), \quad (4.6)$$

where Y_n is the free neutron fraction, $\langle Z \rangle$ is the average proton number of the composition, Q_{imp} is the impurity parameter, and Λ_{eQ} is the Coulomb logarithm for electron-impurity scattering (Potekhin et al., 1999).

4.2 Realistic Cooling Models

Neutron star thermal evolution models that include accretion-driven heating during outburst naturally reproduce quiescent light curves of neutron star transients, for example in XTE J1702-462 (Fridriksson et al., 2010, 2011; Page & Reddy, 2013; Turlione et al., 2015) and EXO 0748-676 (Degenaar et al., 2009, 2014). For example, in Figure 4.1 we show a model fit to the quiescent cooling curve of MXB 1659-29 using the neutron star thermal evolution code dStar (Brown, 2015) where the cooling slab model reproduces well the broken power-law behavior of the quiescent light curve. The code solves the fully general relativistic heat diffusion equation using a method of lines algorithm in the MESA numerical library (Paxton et al., 2011, 2013, 2015) and the microphysics of the crust follows Brown & Cumming (2009).

We modeled the ≈ 2.5 year outburst in MXB 1659-29 (Wijnands et al., 2003, 2004) using a local mass accretion rate $\dot{m} = 0.1 \dot{m}_{\text{Edd}}$, where $\dot{m}_{\text{Edd}} = 8.8 \times 10^4 \text{ g cm}^{-2} \text{ s}^{-1}$ is the local Eddington mass accretion rate. The model uses a neutron star mass of $M = 1.6 M_{\odot}$ and radius of $R = 11.2 \text{ km}$ that are consistent with the quiescent light curve fits from Brown & Cumming (2009). Whereas Brown & Cumming (2009) held T_b fixed during accretion to simulate the effect of a shallow heat source, we instead include the heat source directly and allow T_b to evolve as accretion proceeds. The model includes a $Q_{\text{shallow}} = 1 \text{ MeV}$ per accreted nucleon shallow heat source spread between $y = 2 \times 10^{13} \text{ g cm}^{-2}$ and $y = 2 \times 10^{14} \text{ g cm}^{-2}$ (which will be discussed further in Section 4.2.1), where $y \approx P/g$ is the column depth (Equation 2.3). For the crust composition we use the accreted

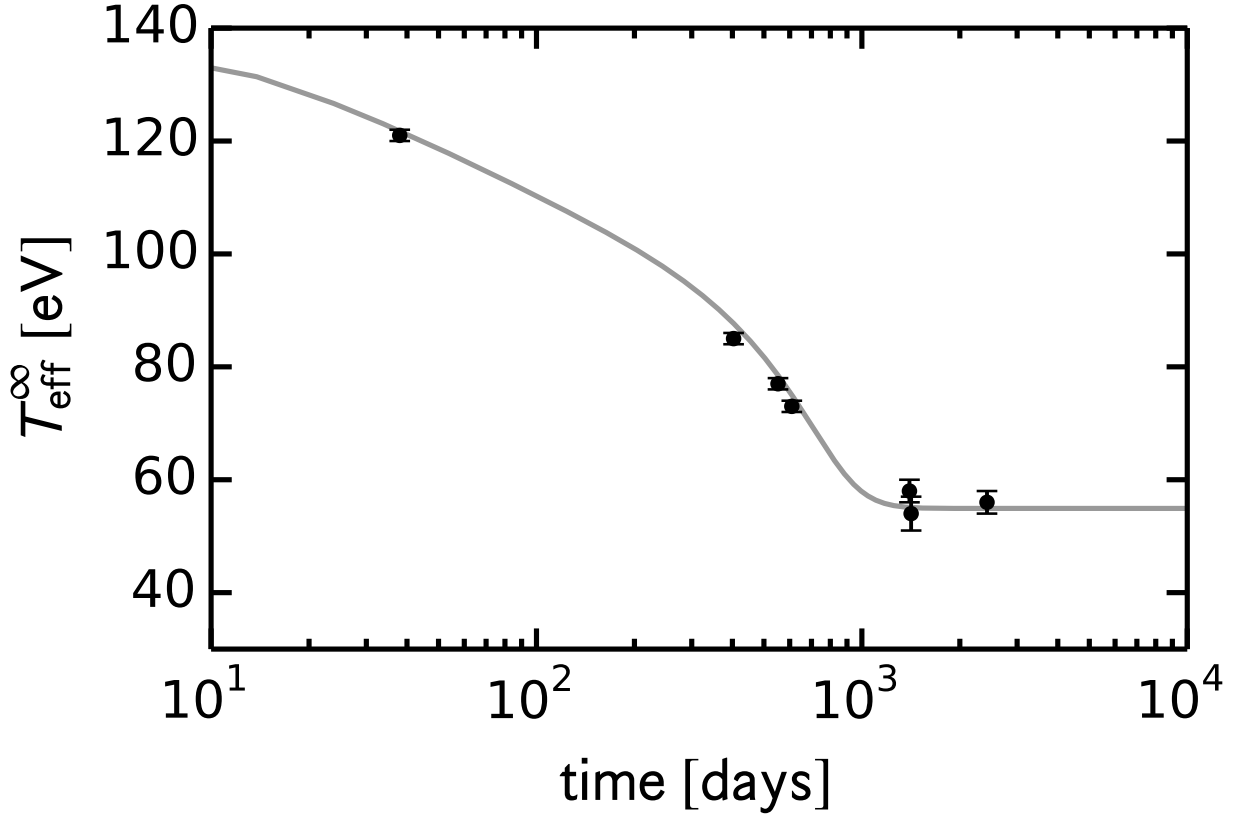


Figure 4.1: Quiescent lightcurve of the neutron star MXB 1659-29. The model uses a neutron star mass of $M = 1.6 M_{\odot}$, a neutron star radius of $R = 11.2$ km, a shallow heat source of $Q_{\text{shallow}} = 1.0$ MeV per accreted nucleon, and a core temperature of $T_{\text{core}} = 4 \times 10^7$ K. The model also uses an impurity parameter of $Q_{\text{imp}} = 2.5$ for the entire crust as done in Brown & Cumming (2009).

composition from Haensel & Zdunik (2008) that assumes an initial composition of pure ^{56}Fe (see their Table A3). The temperature at the top of the crust T_b is mapped to the neutron star’s effective temperature by a $T_{\text{eff}} - T_b$ relation (Gudmundsson et al., 1982, 1983) updated for a mixed helium and iron envelope (Brown et al., 2002).

The model of crust cooling in MXB 1659-29 uses a crust impurity parameter of $Q_{\text{imp}} = 2.5$ and core temperature $T_{\text{core}} = 4 \times 10^7$ K, consistent with the fit from Brown & Cumming (2009). The impurity parameter is assumed constant throughout the entire crust and was constrained to $Q_{\text{imp}} < 10$ in MXB 1659-29 (Brown & Cumming, 2009). In this model, the crust reaches thermal equilibrium with the core by ≈ 1000 days into quiescence, and so predicts a constant temperature

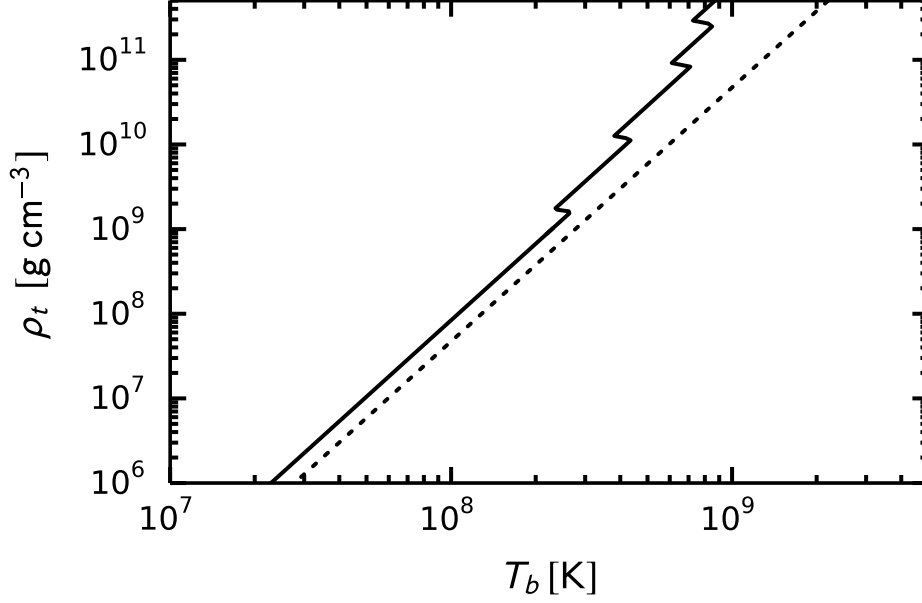


Figure 4.2: Location of the ocean-crust transition as a function of temperature at the base of the ocean. The black solid curve is for the one-component accreted composition (Haensel & Zdunik, 1990) and the black dotted curve is for a multi-component accreted composition (Steiner, 2012). The crystallization density is given by Equation (2).

at later times. The predicted quiescent light curve (Figure 4.1) using our thermal evolution model agrees well with the predicted cooling curve from Brown & Cumming (2009).

Although heat diffuses toward the neutron surface during quiescence, the quiescent light curve can be simply understood as a cooling front moving inward from the surface toward the crust-core interface. Therefore, as the neutron star's outer layers cool the light curve probes successively deeper layers (Brown & Cumming, 2009) with increasingly longer thermal times. A cooling front moving through the neutron star's outer layers will move on a timescale corresponding to the thermal time of the layer its in. The thermal time to reach a mass density ρ (Heney & L'Ecuyer, 1969) is

$$\tau_{\text{therm}} = \frac{1}{4} \left[\int_z \left(\frac{\rho C_V}{K} \right)^{1/2} dz' \right]^2, \quad (4.7)$$

where the integration is carried out over the depth of the layer z , C_V is the specific heat, and K is

the thermal conductivity. The thermal time for the ocean is then

$$\tau_{\text{therm,liquid}}^{\infty} \approx 1.2 \text{ days } \rho_9 \left(\frac{g_{14}}{2} \right)^{-2} \left(\frac{Y_e}{0.4} \right)^3 \left(\frac{Z}{34} \right) \left(\frac{1+z}{1.24} \right), \quad (4.8)$$

where Y_e is the electron fraction, g_{14} is the neutron star gravity in units of $10^{14} \text{ cm s}^{-2}$, and $1+z = (1 - 2GM/(Rc^2))^{-1/2}$ is the redshift to the observer frame at infinity. At higher densities, where $\rho \gtrsim 10^9 \text{ g cm}^{-3}$, the heat capacity is set by the ions with $C_V \approx C_V^{\text{ion}} = 3k_B/Am_u$ (Equation 2.29). The thermal conductivity is set by lattice phonons with an electron-phonon scattering $\nu = \nu_{ep} \approx 13\alpha k_B T/\hbar$ (Baiko & Yakovlev, 1995, 1996), where $\alpha = e^2/\hbar c \approx 1/137$ is the fine structure constant. The resulting thermal time in the solid crust is

$$\tau_{\text{therm,solid}}^{\infty} \approx 2.1 \text{ days } \rho_9 \left(\frac{g_{14}}{2} \right)^{-2} \left(\frac{Y_e}{0.4} \right)^2 \left(\frac{56}{A} \right) \left(\frac{1+z}{1.31} \right), \quad (4.9)$$

as was previously shown in Brown & Cumming (2009) (their Equation 9). As can be seen from the density dependence of the thermal time, the early quiescent light curve probes low densities in the neutron star's ocean and the late time light curve reveals the physics of the inner crust. As we will show in the following sections, the early light curve in MAXI J0556-332 reveals a strong heating anomaly in the shallow crust and the late-time light curve of MXB 1659-29 constrains the thermal properties of the deep inner crust.

4.2.1 Heating Anomalies in MAXI J0556-332

Accretion-driven nuclear reactions deposit $\approx 1 \text{ MeV}$ per accreted nucleon of crustal heating during an accretion outburst; however, some sources require additional heating in the outer crust during outburst to fit quiescent observations. For example KS 1731-260 (Wijnands et al., 2001, 2002) and

MXB 1659-29 (Wijnands et al., 2003, 2004; Cackett et al., 2008) require ≈ 1 MeV per accreted nucleon (Brown & Cumming, 2009) during outburst to fit quiescent light curve observations. Although the source of extra heating is unknown, some heat may be supplied by compositionally-driven convection in the neutron star ocean (Medin & Cumming, 2011, 2014, 2015) and stabilized helium burning in the neutron star envelope (Brown & Bildsten, 1998).

Here we discuss the hottest neutron star transient MAXI J0556-332 that is an exceptional and interesting test case for our thermal evolution model. MAXI J0556-332 was discovered in outburst in January 2011 (Matsumura et al., 2011). The source entered quiescence 16 months later at a high temperature (Homan et al., 2014). In following the quiescent thermal evolution of MAXI J0556-332 during outburst/quiescence, we demonstrate that a strong heating anomaly is present in its deep ocean and shallow crust. In fact, the $\gtrsim 6$ MeV per accreted nucleon of heating is more than can be supplied by compositionally-driven convection or nuclear reactions. Furthermore, the anomalous heating required in this source is greater than any other source observed to date.

To fit the cooling light curve, we assume that a $M = 1.5 M_{\odot}$ and $R = 11$ km neutron star accreted at the local Eddington rate $\dot{m} = \dot{m}_{\text{Edd}} \equiv 8.8 \times 10^4 \text{ g cm}^{-2} \text{ s}^{-1}$ for 16 months, matching the duration of the MAXI J0556-332 outburst (Homan et al., 2014), before cooling began. At the temperatures observed for MAXI J0556-332, the $T_{\text{eff}}-T_b$ relation is insensitive to the helium mass in the envelope. The shallow heat source is uniformly distributed in $\log y$ centered on a value $y_h = 6.5 \times 10^{13} \text{ g cm}^{-2}$ ($\rho \approx 1.2 \times 10^{10} \text{ g cm}^{-3}$) and ranging from $y_h/3$ to $y_h \times 3$; where the column depth y is given in Equation 2.3. The strength of shallow heating is assumed to vary proportionally with the accretion rate.

As can be seen in Figure 4.3, the moderate gravity from a $M = 1.5 M_{\odot}$ and $R = 11$ km neutron star best reproduces the quiescent cooling observations of MAXI J0556-332. Late time observations will change with gravity, not only due to the $T_{\text{eff}}^{\infty} \propto g^{1/4}/(1+z)$ scaling, but also due

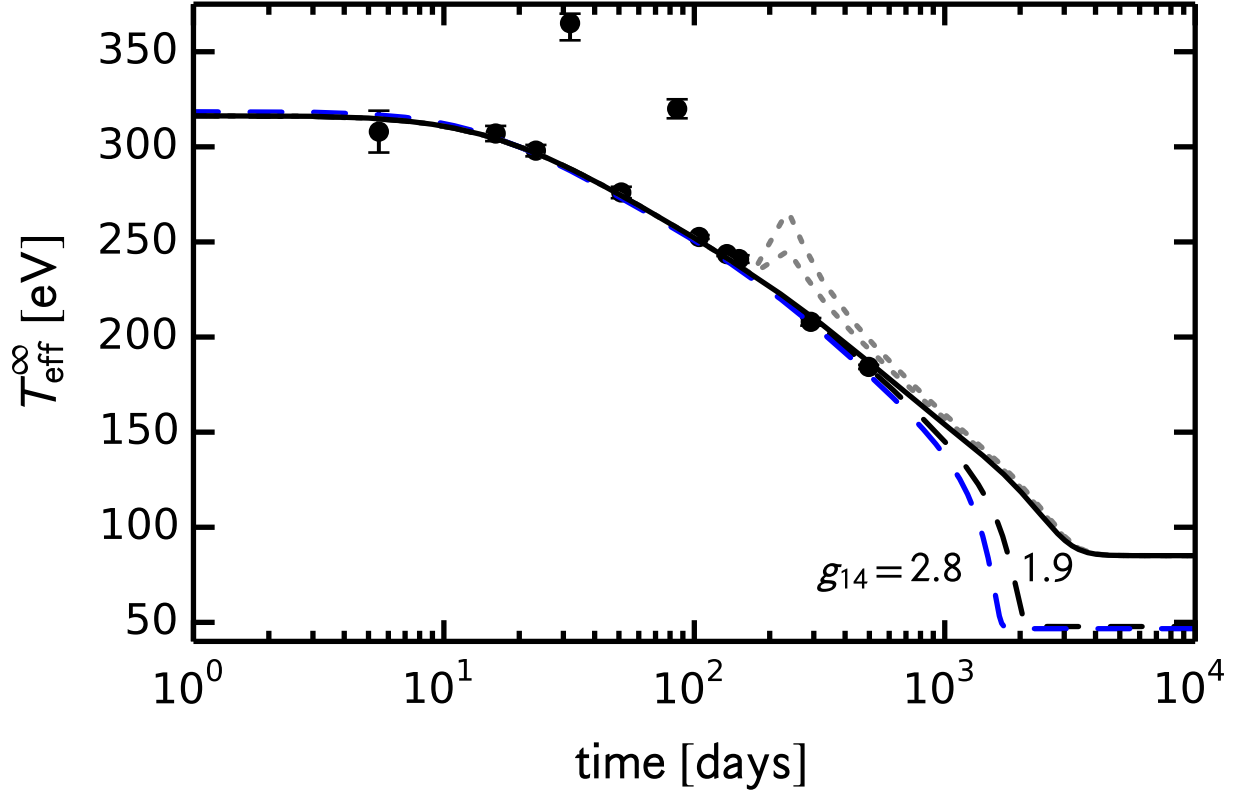


Figure 4.3: Quiescent lightcurve of the neutron star MAXI J0556-332. The solid black curve corresponds to a model with $M = 1.5 M_{\odot}$, $R = 11$ km, $Q_{\text{shallow}} = 6.0$ MeV, and $T_{\text{core}} = 10^8$ K; the dashed black curve is for the same model with $T_{\text{core}} = 3 \times 10^7$ K. The black dotted curves are light curves with a reheating event ≈ 170 days into quiescence for $Q_{\text{shallow}} = 6.0$ MeV (upper curve) and $Q_{\text{shallow}} = 3.0$ MeV (lower curve). The blue dashed curve is for a $M = 2.1 M_{\odot}$, $R = 12$ km neutron star fit to the observations by changing the shallow heating depth and strength. The data above the light curve are contamination from residual accretion. Note that $T_{\text{eff}}^{\infty} \propto g^{1/4}/(1+z)$ which leads to different observed core temperatures for different gravities.

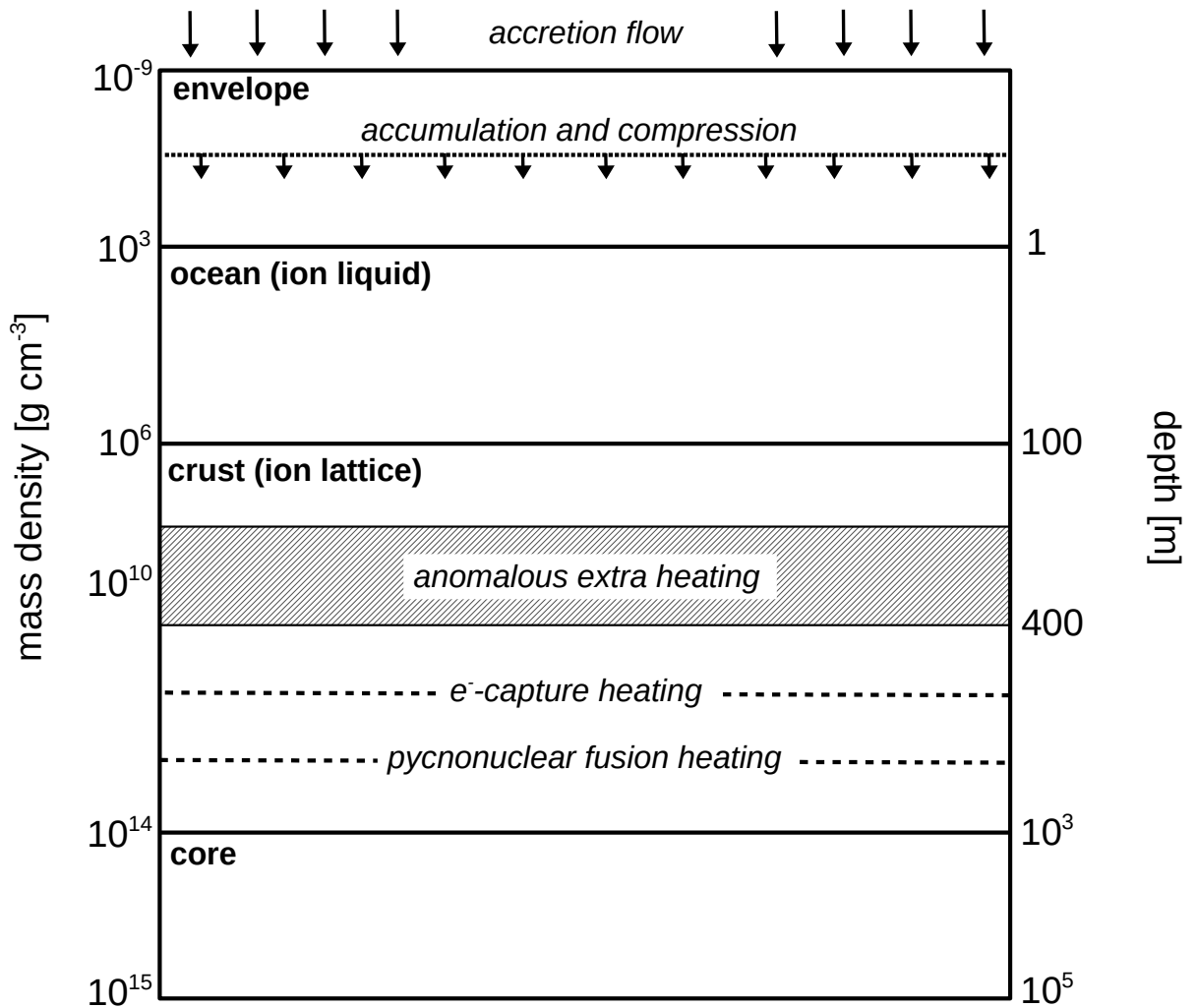


Figure 4.4: Schematic of the neutron star's outer layers and the location of the anomalous shallow heating in MAXI J0556-332.

to the thickness of the crust. As shown by Deibel et al. (2015), a fit to the quiescent light curve requires extra heating of $Q_{\text{shallow}} = 6.0 \text{ MeV}$ per accreted nucleon. The heat must be deposited over the range $y \approx 2 \times 10^{13} - 2 \times 10^{14} \text{ g cm}^{-2}$ in order to fit the break in the light curve near ≈ 20 days, as shown schematically in Figure 4.4. Although the depth of extra heating is well constrained by the break in the light curve, other neutron star masses and radii require a different amount of extra heating, as can be seen in Figure 4.6. Similar shallow heating is required in thermal evolution models of MXB 1659-29 and KS 1731-260 (Brown & Cumming, 2009), each requiring $\approx 1 \text{ MeV}$ per accreted nucleon extra heating during outburst near $y \lesssim 2 \times 10^{14} \text{ g cm}^{-2}$ to fit the quiescent light curve.

Shallow heating raises the temperature of the crust to $T_b \sim 10^9 \text{ K}$ by the end of outburst. The ocean-crust boundary (the crust melting point, Equation 2.4) is pushed significantly deeper as a result. By the end of outburst the ocean-crust boundary is located at $\rho_t \approx 2 \times 10^{11} \text{ g cm}^{-3}$, as can be seen in Figure 4.5. The crust is in a near maximally hot state, due to the large amount of shallow heating, with a temperature “ceiling” set by neutrino emission at mass densities $\rho \gtrsim 10^{10} \text{ g cm}^{-3}$. Because $T_b > \Theta_D$ throughout the outer crust, the thermal conductivity is set by electron-ion scattering and the thermal time from Equation 4.8 applies.

Note that MAXI J0556-332 requires more shallow heating than other sources; the $\approx 4\text{--}10 \text{ MeV}$ per accreted nucleon of shallow heating is larger than required in KS 1731-260 and MXB 1659-29, each requiring $\approx 1 \text{ MeV}$ per accreted nucleon (Brown & Cumming, 2009). This hints at an energy source much larger than the $\approx 0.2 \text{ MeV}$ per accreted nucleon supplied by compositionally driven convection in the ocean (Medin & Cumming, 2011, 2014, 2015) or the $\approx 2 \text{ MeV}$ per accreted nucleon additional deep crustal heating possible given the uncertainties on the nuclear symmetry energy (Steiner, 2012). The Keplerian energy of the accretion flow is $\sim 80 \text{ MeV}$ per accreted nucleon (at the inner-most stable circular orbit) and may plausibly provide the shallow heating. As

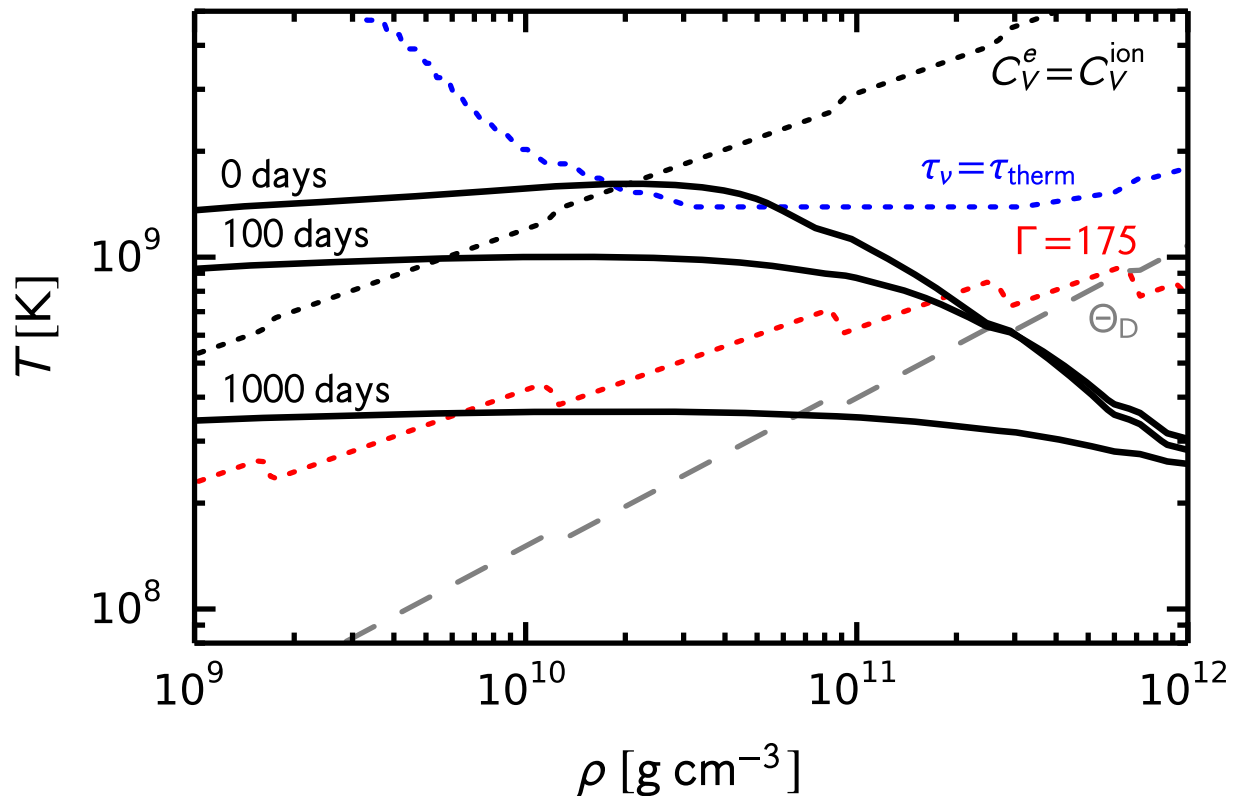


Figure 4.5: Quiescent temperature evolution of the neutron star MAXI J0556-332. Solid black curves indicate the evolution of the crust temperature during quiescence for the $M = 1.5 M_{\odot}$ and $R = 11$ km model, shown in Figure 4.3. The red dotted curve is the melting line of the crust ($\Gamma = 175$) for the crust composition in Haensel & Zdunik (1990), the black dotted curve is the transition from an electron-dominated heat capacity to an ion-dominated heat capacity ($C_V^e = C_V^{\text{ion}}$), and the blue dotted curve is where the local neutrino cooling time is equal to the thermal diffusion time ($\tau_{\nu} = \tau_{\text{therm}}$). The gray dashed curve shows the lattice Debye temperature Θ_D ; when $T \ll \Theta_D$ electron-impurity scattering influences the thermal conductivity.

suggested by Inogamov & Sunyaev (1999, 2010), gravitational modes excited in a differentially rotating envelope may dissipate energy deeper in the star. The mode energies are of the order required and the dissipation of these modes in the shallow crust is worthy of future study with realistic ocean and crust models.

The high accretion rate during outburst, when combined with the large amount of shallow heating, brings the crust into a regime of stable helium burning for helium layers at $y \approx 2 \times 10^8 \text{ g cm}^{-2}$ (Bildsten & Brown, 1997; Zamfir et al., 2014). During outburst, the crust also enters a regime of stable carbon burning for carbon layers at $y \gtrsim 10^{10} \text{ g cm}^{-2}$ (Cumming & Bildsten, 2001). For this reason, an appreciable layer of carbon can not accumulate at the superburst ignition depth around $y \sim 10^{12} \text{ g cm}^{-2}$. There have been no Type I X-ray bursts or superbursts observed from MAXI to date, consistent with stable burning of helium and carbon. We predict that MAXI J0556-332 is unlikely to have either type-I X-ray bursts or superbursts if strong shallow heating occurs during subsequent accretion outbursts.

4.2.2 The Reflare in MAXI J0556-332

The luminosity of MAXI J0556-332 increased ≈ 170 days into quiescence to a level similar to that observed at the end of the outburst, and the reflare lasted for ≈ 60 days (Homan et al., 2014). We run a model that accretes at $\dot{m} \approx 0.5 \dot{m}_{\text{Edd}}$ for 60 days after a 170 day initial cooling phase to model the reflare event. We run the model for two values of the shallow heating source, $Q_{\text{shallow}} = 6.0 \text{ MeV}$ and $Q_{\text{shallow}} = 3.0 \text{ MeV}$, which can be seen in Figure 4.3.

The light curves that include the reflare overshoot the observations hundreds of days into quiescence and the light curve deviation lasts ≈ 500 days before returning to the cooling behavior seen prior to the reflare. Clearly, extra heating must not be operating during the reflare, or it must be significantly weaker than during the main accretion outburst. This result may imply that the

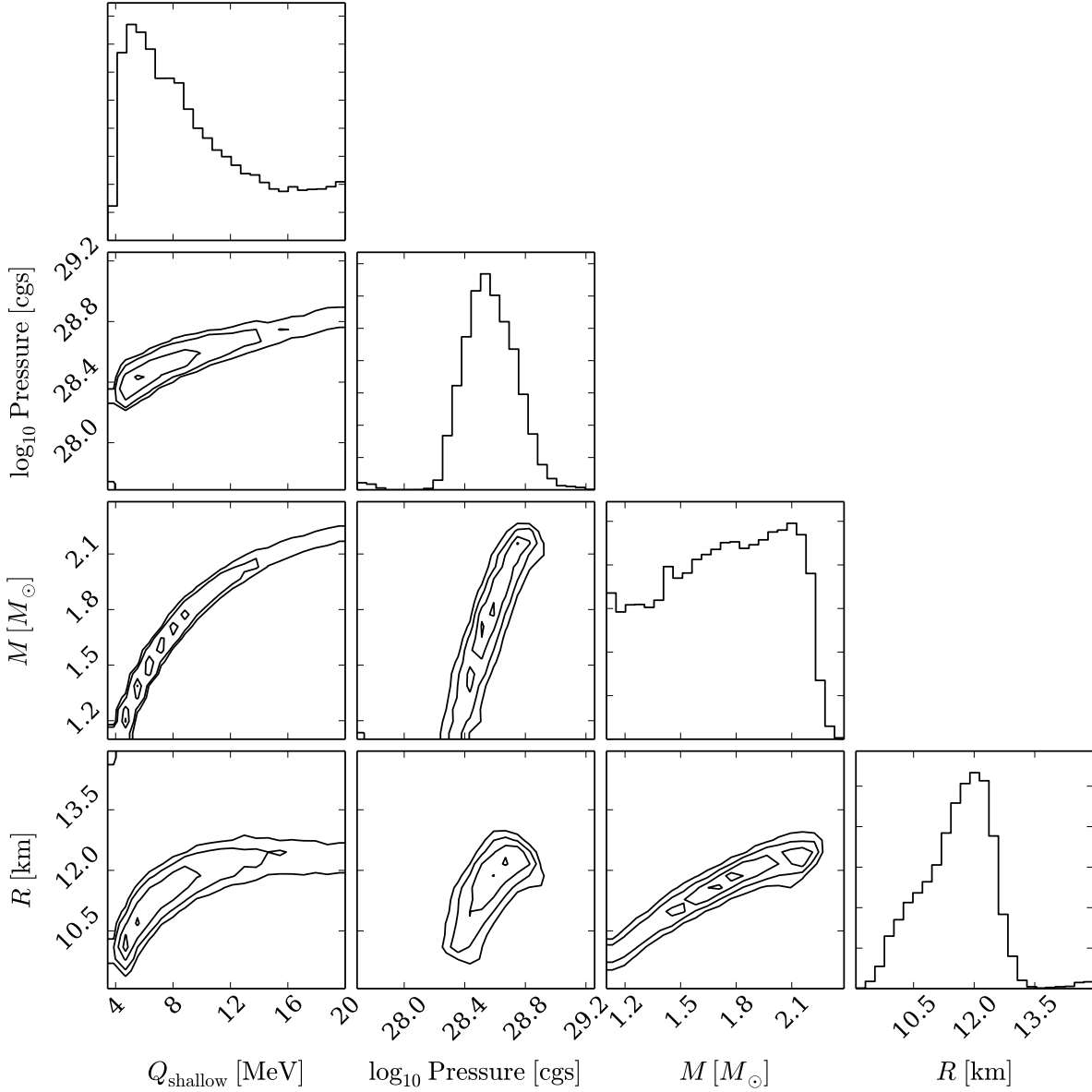


Figure 4.6: Markov chain Monte Carlo fits to the quiescent light curve of MAXI J0556-332 using the crust relaxation code *crustcool*. The contours show the isodensity surfaces of the likelihood \mathcal{L} , corresponding to $\sqrt{-2\ln\mathcal{L}} = 0.5, 1, 1.5, 2$, for the neutron star mass M , radius R , pressure at the shallow heating depth P_h , and the shallow heating strength Q_{shallow} .

extra heating mechanism is not proportional to the mass accretion rate, as is assumed in our thermal relaxation model. The lack of extra heating during the reflare is similar to the lack of extra heating in the ≈ 2 month outburst seen in Swift J174805.3-244637 (Degenaar et al., 2015). Extra heating is needed, however, after a similar ≈ 2.5 month outburst in IGR J17480-2446 (Degenaar & Wijnands, 2011; Degenaar et al., 2011, 2013). These sources may have fundamental differences in their structure that make extra heating active in one and not the others, or perhaps the growth timescale of the extra heating mechanism is ~ 2 months in all sources.

4.3 Observational Tests for Ocean g -modes

The Z sources are neutron stars that accrete intermittently near the Eddington rate (Hasinger & van der Klis, 1989) as inferred from their X-ray luminosities between $L_X \sim 0.5-1.0 L_{X,\text{Edd}}$, see Lewin & van der Klis (2006) for a review. These sources trace out a distinctive “Z” shape in the X-ray color-color diagram: the top of the Z is the horizontal branch, the diagonal is the normal branch, and the bottom of the Z is the flaring branch. The spectral state of the source (i.e., its location on the Z) was traditionally thought to be correlated with changes in the mass accretion rate (Priedhorsky et al., 1986; Hasinger et al., 1990; Homan et al., 2007), but more likely cause secular evolution of a source between a Z-source state and a lower luminosity atoll state ($L_X \sim 0.1-0.5 L_{X,\text{Edd}}$) (Lin et al., 2009). Instead, accretion instabilities at a constant accretion rate are likely the determining factor for changes in the spectral state (Lin et al., 2009; Homan et al., 2010; Fridriksson et al., 2015).

Quasi-periodic oscillations (hereafter QPOs) have been observed in Z-source power spectra during their evolution along the Z-track and each branch of the Z-track has a characteristic set of QPO frequencies, see Lewin & van der Klis (2006) for a review. These QPOs typically appear at

low-frequencies: the horizontal branch oscillations (hereafter HBOs) are QPOs with frequencies between $\approx 10\text{--}30$ Hz. The normal branch oscillations (hereafter NBOs) are QPOs with frequencies ~ 6 Hz. The NBOs increase as the source moves toward the flaring branch and the NBOs eventually blend into flaring branch oscillations (hereafter FBOs) around $\approx 10\text{--}50$ Hz. For instance, continuous blending have been observed in Sco X-1 (van der Klis, 1989; Casella et al., 2006).

The HBOs are thought to be of a geometric origin, resulting from Lense-Thirring precession of the inner-most region of the accretion disk (Lense & Thirring, 1918; Bardeen & Petterson, 1975). Furthermore, the HBOs are consistent with similar frequency QPOs from accreting black holes in the same spectral state. The NBOs may originate from oscillations on the neutron star or accretion disk. For example, the neutron star ocean may host a variety of non-radial oscillations; such as, thermal g -modes (Bildsten & Cutler, 1995; Bildsten et al., 1996; Bildsten & Cumming, 1998). The FBOs are consistent with shallow surface waves in the ocean, known as crustal interface modes (Piro & Bildsten, 2005). Although the FBOs typically have large frequencies $\gtrsim 100$ Hz, the deformability of the crust may pin these modes deep in the crust and result in lower frequencies $\lesssim 20$ Hz (Piro & Bildsten, 2005).

The cores of accreting neutron stars may also contain oscillations, although these oscillations occur at much high frequencies. Specifically, rotating relativistic stars are unstable to the production of Rossby-modes (hereafter r -modes) in their cores, that are excited by gravitational radiation (Andersson, 1998) — analogous to hurricane-like r -modes in a terrestrial ocean. Recently, limits were placed on neutron star core r -mode amplitudes from spin-down rates and thermal emission from quiescent low-mass X-ray binaries (Mahmoodifar & Strohmayer, 2013). Interestingly, the core r -modes may propagate into the neutron star's ocean during an accretion outburst, where their amplitudes increase (Lee, 2014). A candidate r -mode was observed in XTE J1751-305 as a ≈ 250 Hz oscillation in the X-ray light curve (Strohmayer & Mahmoodifar, 2014). This frequency

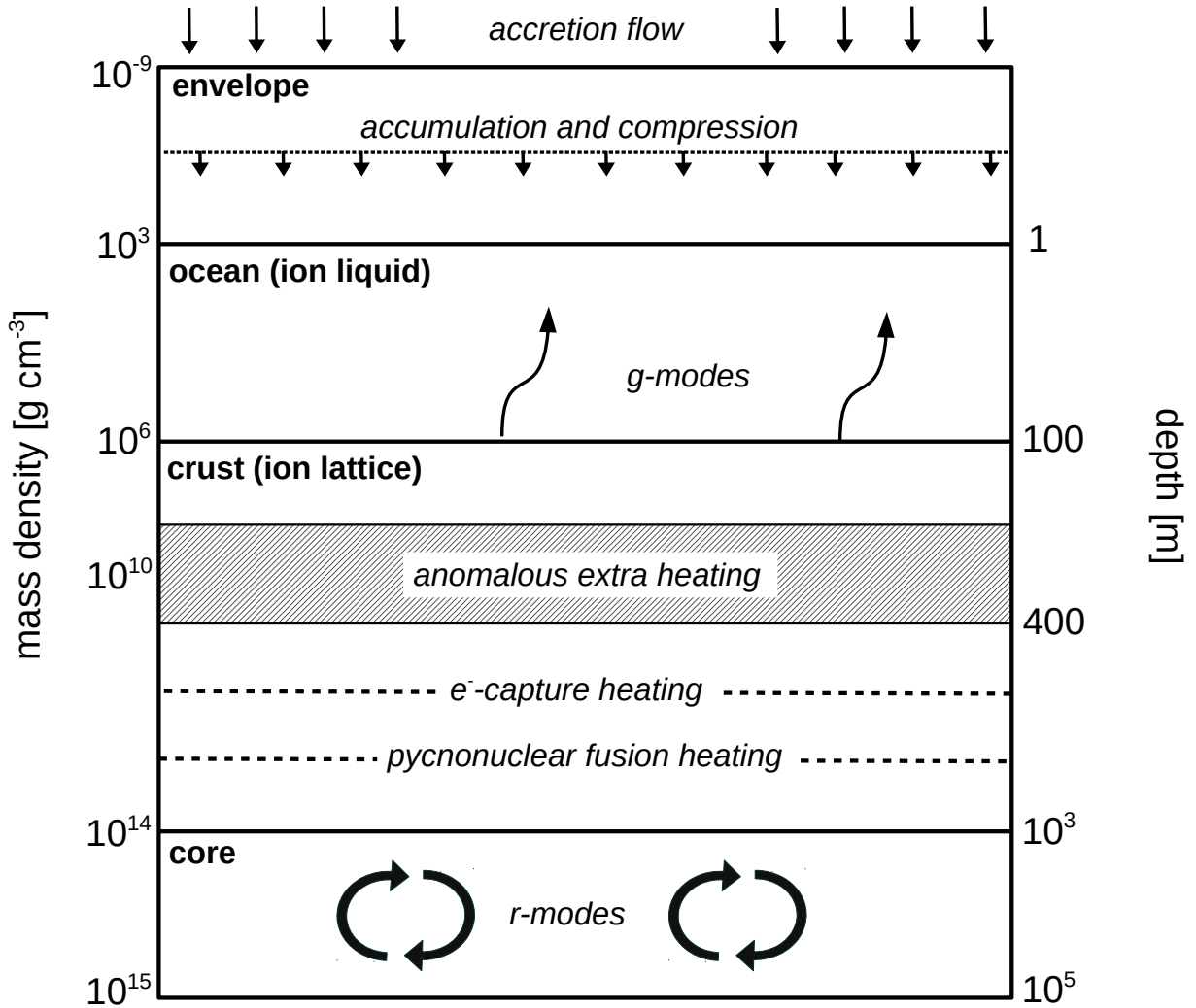


Figure 4.7: Schematic of the neutron star’s outer layers and the location of g -modes.

is approximately $2/3$ of the star’s rotation frequency ($\nu \approx 435$ Hz), which is consistent with a core r -mode (Andersson et al., 2014).

In the following section, we outline an observational test for the origin of NBOs using the thermal evolution of the neutron star ocean during an accretion outburst, following the approach of Deibel (2016). In particular, the larger ocean temperatures during an accretion outburst will raise the ocean’s fundamental g -mode frequencies and therefore lead to larger NBO frequencies if ocean g -modes are indeed the origin of the NBOs. Moreover, the hottest neutron star transients

that require shallow heating in their oceans have the largest g -mode frequencies during outburst and thereby provide excellent observational tests for the presence of ocean g -modes. In particular, we will examine the ocean’s thermal evolution in three neutron star transient Z-sources, all with observed accretion outbursts: MXB 1659-29, XTE J1701-462, and MAXI J0556-332.

4.3.1 Neutron Star Ocean Thermal Evolution

During an accretion outburst, the ocean temperature rises as accretion-driven nuclear reactions in the crust supply a heat flux into the ocean (Brown, 2000). Although a majority of crustal heating ($\approx 90\%$) is conducted toward the core, the heat flux entering the ocean is sufficient to raise the temperature to $T_b \gg 10^8$ K during outburst. The increase in temperature will be especially pronounced in neutron stars that have active shallow heating during their accretion outbursts, such as KS 1731-260 and MXB 1659-29 which require ≈ 1 MeV per accreted nucleon (Brown & Cumming, 2009), and MAXI J0556-332 which requires $\approx 6\text{--}16$ MeV per accreted nucleon (Deibel et al., 2015).

As can be seen in Figure 2.2, the ocean crystallization point (given by Equation 2.5) shifts to higher mass densities as the crust temperature increases. Initially the neutron star ocean is in thermal equilibrium with the neutron star core near $T_b \approx T_{\text{core}} = 3 \times 10^7$ K and the ocean-crust transition density is $\rho \approx 2.2 \times 10^6$ g cm $^{-3}$. During an accretion outburst, the ocean temperature increases, and the ocean-crust transition density increases, as unavoidable accretion-driven nuclear reactions heat the ocean out of thermal equilibrium with the core. We now examine the ocean’s thermal evolution in three neutron star transient Z-sources: MXB 1659-29, XTE J1701-462, and MAXI J0556-332.

We run a model of the MAXI J0556-332 ≈ 460 day accretion outburst (Matsumura et al., 2011; Homan et al., 2011; Sugizaki et al., 2013; Homan et al., 2014), with the neutron star parameters fit

from quiescent observations: $M = 1.5 M_{\odot}$, $R = 11$ km, $Q_{\text{shallow}} = 6$ MeV per accreted nucleon, and $Q_{\text{imp}} = 1$. During outburst, the ocean-crust transition (Equation 2.5) moves from $\rho \approx 2.2 \times 10^6$ g cm $^{-3}$ at the beginning of outburst to $\approx 2 \times 10^{11}$ g cm $^{-3}$ by the end of outburst when the ocean temperature is $T_b \approx 7.5 \times 10^8$ K. The ocean properties as a function of time during the accretion outburst can be seen in Figure 4.8. The ocean has $T_b \gtrsim 7 \times 10^8$ K for ≈ 500 days into quiescence and takes ≈ 2900 days to reestablish thermal equilibrium with the core.

We also run thermal evolution models for the observed accretion outbursts in MXB 1659-29 and XTE J1701-462. For MXB 1659-29 we run a model of its previous 2.5 year outburst (Wijnands et al., 2003, 2004) at the accretion rate inferred for this source near $\langle \dot{M} \rangle \approx 0.1 \dot{M}_{\text{Edd}}$. Brown & Cumming (2009) fit the quiescent light curve of this source and found the best-fit parameters: $M = 1.5 M_{\odot}$, $Q_{\text{imp}} \approx 4$, and $Q_{\text{shallow}} \approx 1$ MeV per accreted nucleon. The properties of the ocean in MXB 1659-29 during outburst and quiescence can be seen in Figure 4.8. The ocean has $T_b \gtrsim 10^8$ K for ≈ 700 days into quiescence and takes ≈ 1400 days to reestablish thermal equilibrium with the core.

For XTE J1701-462, we run a thermal evolution model for its ≈ 2 year outburst (Fridriksson et al., 2010, 2011). We use the neutron star parameters fit from quiescent light curve fits: $M = 1.6 M_{\odot}$, $R = 11.6$ km, and $Q_{\text{imp}} \approx 7$. We also add $Q_{\text{shallow}} = 0.17$ MeV per accreted nucleon from a recent study of the quiescent light curve (Turlione et al., 2015). The properties of the ocean in XTE J1701-462 during outburst and quiescence can be seen in Figure 4.8. The ocean has $T_b \gtrsim 10^8$ K for ≈ 1700 days into quiescence and takes ≈ 3100 days to reestablish thermal equilibrium with the core.

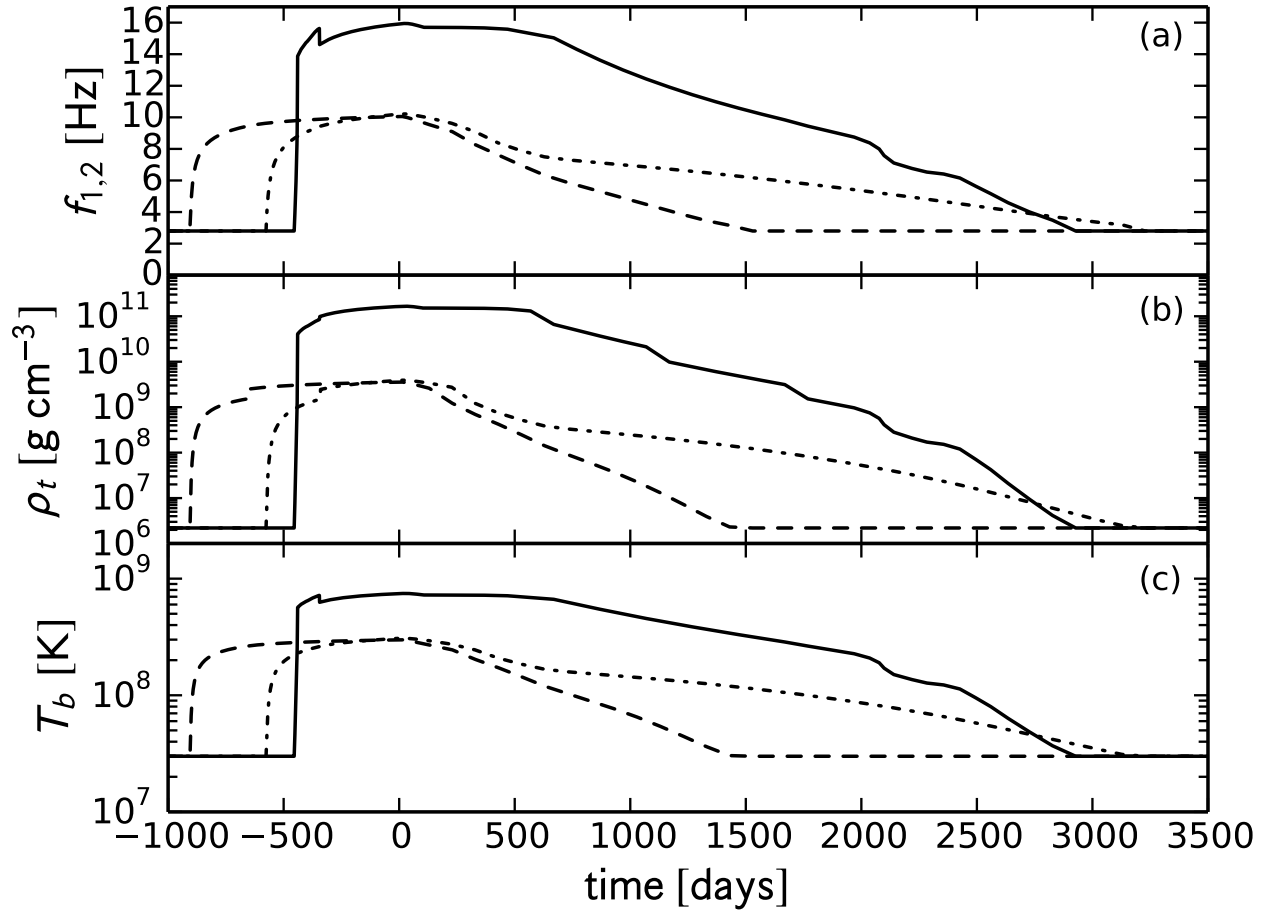


Figure 4.8: Thermal evolution as a function of time during outburst/quiescence for MAXI J0556-332 (solid curves), MXB 1659-29 (dashed curves), and XTE J1701-462 (dot-dashed curves). *Panel (a)*: Fundamental $n = 1$, $l = 2$ g -mode frequencies in the ocean (Equation 4.10). *Panel (b)*: The ocean-crust transition density (Equation 2.5). *Panel (c)*: Temperature at the ocean-crust transition.

4.3.2 g -mode Spectrum of the Neutron Star Ocean

The g -modes may be excited in the neutron star ocean as angular momentum is transported into the ocean by a spreading layer of accreted material (Inogamov & Sunyaev, 1999, 2010) — the same mechanism that excites global acoustic modes in the neutron star envelope during accretion (Philippov et al., 2016). The g -mode spectrum has been derived for the ocean (McDermott et al., 1983; Bildsten & Cutler, 1995). For a non-rotating neutron star with a magnetic field $B \lesssim 10^{11}$ G, the g -mode frequencies can be analytically approximated within $\approx 10\%$ (Bildsten & Cutler, 1995),

$$f_{n,l} \approx 2.8 \text{ Hz} \left[\frac{l(l+1)}{6} \frac{T_b}{3 \times 10^7 \text{ K}} \frac{56}{A} \right]^{1/2} \left(\frac{10 \text{ km}}{R} \right) \times \left[1 + \left(\frac{3n\pi}{2} \right)^2 \left(\ln \left\{ \frac{\rho_t}{1 \text{ g cm}^{-3}} \right\} \right)^{-2} \right]^{-1/2}, \quad (4.10)$$

where n is the number of nodes in the ocean, l is the angular wavenumber, and R is the radius of the neutron star. The upper boundary of the ocean is taken at the base of the envelope near a mass density $\rho \approx 1 \text{ g cm}^{-3}$, however, the frequency spectrum is largely insensitive to the location of this upper boundary. Even though Equation 4.10 is derived for an isothermal ocean, the oscillation spectrum is primarily set by the temperature at the base of the ocean in non-isothermal models (Bildsten & Cumming, 1998), and Equation 4.10 gives frequencies accurate within $\approx 10\%$ (Bildsten & Cutler, 1995). Note that this expression is not valid for rapidly rotating neutron stars with $f_{\text{spin}} \gg 300 \text{ Hz}$, where the g -mode frequencies become highly modified (Bildsten et al., 1996).

The thermal time in the ocean (Equation 4.8) determines the time to raise the ocean's temperature during the accretion outburst. The thermal time in the liquid ocean is shown in Figure 4.2.

Normal-branch oscillations have been observed in several sources, for example Cyg X-2 (Hasinger & van der Klis, 1989; Wijnands et al., 1997; Dubus et al., 2004), SCO X-1 (Hertz et al., 1992; van

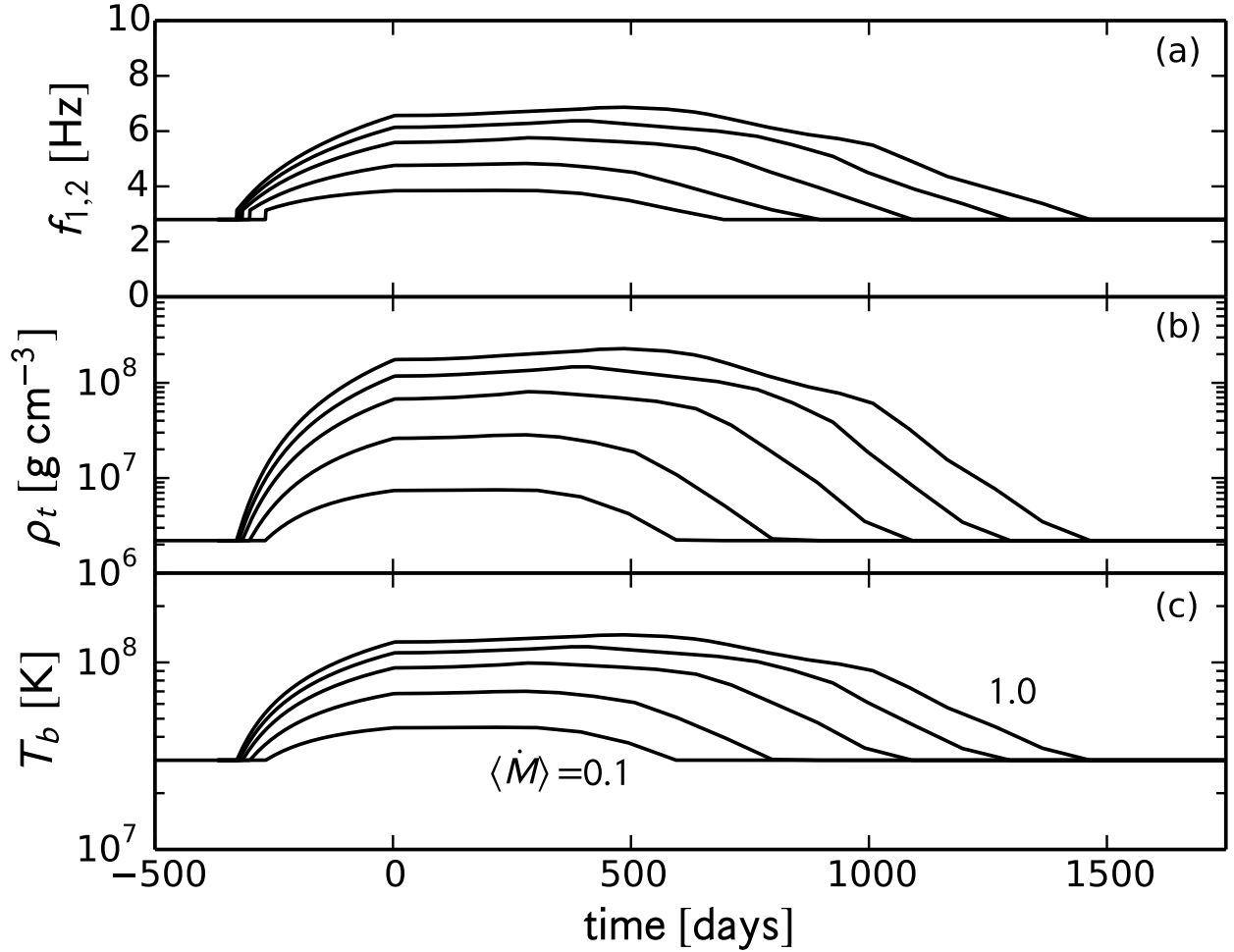


Figure 4.9: Thermal evolution as a function of time during outburst/quiescence for neutron star transients with $\langle \dot{M} \rangle = 0.1\text{--}1.0 \dot{M}_{\text{Edd}}$. *Panel (a)*: Fundamental $n = 1$, $l = 2$ g -mode frequencies in the ocean (Equation 4). *Panel (b)*: The ocean-crust transition density (Equation 2). *Panel (c)*: Temperature at the ocean-crust transition.

der Klis et al., 1996; Titarchuk et al., 2014), and GX 5-1 (Kuulkers et al., 1994; Jonker et al., 2002). NBO frequencies are typically between $\approx 5\text{--}7$ Hz, but larger frequencies are observed; for example, XTE J1701-462 has NBO frequencies between $\approx 7\text{--}9$ Hz (Homan et al., 2007; Fridriksson et al., 2010). As we show in this section, the temperature of the neutron star’s ocean during outburst supports fundamental g -modes of similar frequencies. In particular, we run a model of the last outburst in XTE J1701-462 and find g -modes consistent with the observed NBO frequencies in this source.

Before accretion begins, the predicted fundamental g -mode is initially ≈ 3 Hz in the cold ocean ($T_b \approx T_{\text{core}} \sim 10^7$ K). During active accretion, the predicted fundamental g -mode frequency increases as unavoidable accretion-driven nuclear heating raises the ocean’s temperature. For example, sources accreting between $\langle \dot{M} \rangle = 0.1\text{--}1.0 \dot{M}_{\text{Edd}}$ have predicted fundamental g -modes between $\approx 3\text{--}7$ Hz, as can be seen in Figure 4.9. Predicted fundamental g -mode frequencies $\gtrsim 7$ Hz require active shallow heating during outburst to reach ocean temperatures $\gtrsim 10^8$ K required to support these frequencies. Therefore, observing NBOs $\gtrsim 7$ Hz in transients that require shallow heating, such as MAXI J0556-332, MXB 1659-29, and XTE J1701-462, provides an observational test to link NBOs and the ocean g -modes. In particular, during steady state accretion MAXI J0556-332 has predicted fundamental g -mode frequencies between $\approx 8\text{--}16$ Hz, MXB 1659-29 and XTE J1701-462 have predicted g -mode frequencies between $\approx 8\text{--}10$ Hz — frequencies only possible in the hotter oceans found in sources with shallow heating. The evolution of the predicted fundamental g -mode in these sources can be seen in Figure 4.8. We predict that MAXI J0556-332 had a fundamental g -mode frequency near ≈ 11 Hz at the time of its recent activity (Negoro et al., 2016; Russell & Lewis, 2016; Jin & Kong, 2016). If shallow heating is active during the current outburst in MXB 1659-29 (Negoro et al., 2015), we predict this source will have a fundamental g -mode frequency near ≈ 9 Hz at the time of the most recent observation (Bahramian et al., 2016) after being in outburst for ≈ 160 days.

NBO frequencies observed in the last outburst from XTE J1701-462 (Fridriksson et al., 2010) are consistent with ocean g -modes. NBOs were observed within the first ≈ 10 weeks near ≈ 7 Hz (Homan et al., 2007), and our model predicts fundamental g -mode frequencies near ≈ 7 Hz after 10 weeks of active accretion. Furthermore, once the ocean reaches steady state, our model of the XTE J1701-462 outburst contains predicted ocean g -modes between $\approx 7\text{--}10$ Hz, which is consistent with the observed $\approx 7\text{--}9$ Hz NBOs observed in this source during outburst (Homan

et al., 2010).

Although current instrumentation may not allow observations of NBOs in MXB 1659-29 and MAXI J0556-332 during quiescence, renewed accretion outbursts in both objects may allow observations of NBOs. We predict that observed NBOs during these sources current accretion outbursts should be $\gtrsim 5$ Hz in MXB 1659-29 and $\gtrsim 10$ Hz in MAXI J0556-332. The renewed activity in MAXI J0556-332 (Negoro et al., 2016; Russell & Lewis, 2016) perhaps holds the best prospects for catching large NBO frequencies because the ocean in MAXI J0556-332 had not cooled to the core temperature before the most recent accretion outburst, and the predicted ocean g -mode frequency is already $\gtrsim 7$ Hz.

Note that the above observational tests for the presence of ocean g -modes does not require a complete picture of how X-ray emission is modulated by ocean oscillations, which is outside the scope of this work. Uncertainties remain in the nature of the accretion flow near the neutron star surface and how the accretion flow may interact with the neutron star's outer layers. For example, a spreading boundary layer of accreted material may extend into the ocean (Inogamov & Sunyaev, 1999, 2010), and may transport angular momentum therein. A coupling of the boundary layer and the ocean in this way may only modulate X-ray emission near the equator, however, where modes may even interfere with accretion disk emission (Bildsten et al., 1996). If observations support a g -mode origin for the NBOs, this will motivate future work to model the ocean's coupling to a spreading boundary layer.

If NBOs are indeed ocean g -modes, observed NBO frequencies $\gtrsim 7$ Hz can then be used as a diagnostic of the shallow heating strength. For example, as shown in this work, ocean g -mode frequencies near ≈ 10 Hz (≈ 16 Hz) are found in sources in steady state with $Q_{\text{shallow}} \approx 1$ MeV ($Q_{\text{shallow}} \approx 6$ MeV). It is worth noting, however, that during outburst the ocean in MAXI J0556-332 approaches a maximum temperature set by neutrino emission around $T_b \approx 2 \times 10^9$ K at the

depth of the shallow heat source (Deibel et al., 2015). Because the ocean temperature is near maximum, a g -mode frequency of ≈ 16 Hz is likely the largest $n = 1$ $l = 2$ g -mode that can be supported in Z-source oceans. Therefore, NBO frequencies of ≈ 16 Hz only give the lower limit $Q_{\text{shallow}} \gtrsim 6$ MeV for the shallow heating strength.

The depth of the ocean-crust transition during outburst is relevant to the study of the shallow heating mechanism. For example, the ocean-crust interface in MAXI J0556-332 moves to densities between $\rho_t \sim 10^9$ – 10^{11} g cm $^{-3}$ during outburst. This density range is characteristic of the location of the shallow heating inferred from quiescent light curves of quasi-persistent transients (Brown & Cumming, 2009), which is needed at mass densities near $\rho_{\text{shallow}} \lesssim 3 \times 10^{10}$ g cm $^{-3}$. For example, shallow heating is required between $\rho_{\text{shallow}} \sim 5 \times 10^9$ – 3×10^{10} g cm $^{-3}$ in MAXI J0556-332, as determined from its quiescent light curve (Deibel et al., 2015). This suggests that the shallow heating mechanism is connected to the ocean-crust phase transition, and work in this direction is ongoing.

Often the observed ≈ 5 – 7 Hz NBOs blend into ≈ 10 – 20 Hz flaring branch oscillations (hereafter FBOs); for example, a continuous blending was observed in SCO X-1 (Casella et al., 2006). The timescale of observed NBO-FBO blending disfavors a g -mode origin for the FBOs. The thermal time at the depth of the ocean-crust transition (Figure 4.10) determines the timescale for variations in the g -mode frequencies. For g -mode frequencies $\lesssim 7$ Hz, variations may occur on timescales of hours; variations in frequencies $\gtrsim 7$ Hz occur on timescales of days — much longer than the timescale of the observed blending. The NBO-FBO blending phenomena, however, is consistent with a superposition of ocean g -modes and ocean interface waves. The interface modes were determined to have frequencies ~ 200 Hz when calculated with a rigid crust boundary condition (McDermott et al., 1988), but may have lower frequencies near ~ 20 Hz when the flexibility of the crust is taken into account (Piro & Bildsten, 2005). It is unclear why oscillation energy might

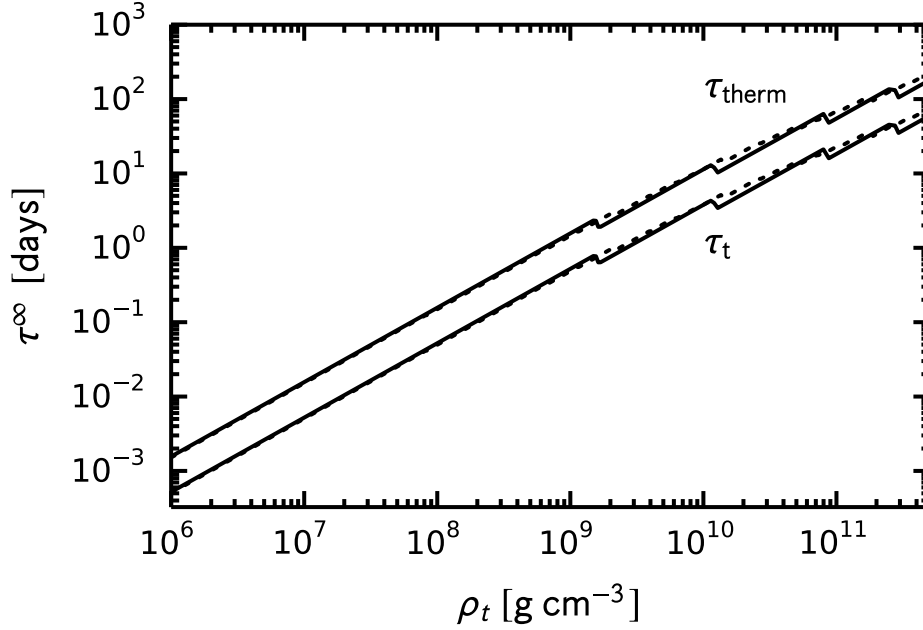


Figure 4.10: Characteristic timescales in the neutron star ocean. The upper curves are the thermal time for an equilibrium composition (solid curve) and accreted composition (dotted curve). The lower curves are for the timescale for changes in ρ_t for an equilibrium composition (solid curve) and an accreted composition (dotted curve).

transition between the different modes, but the coupling of the g -modes to the interface modes is worthy of future study.

Quasi-periodic oscillations between $\approx 5\text{--}7$ Hz in the atoll sources ($L_X \sim 0.1\text{--}0.5 L_{X,\text{Edd}}$) are also consistent with ocean g -modes. For example, the ≈ 7 Hz oscillation observed in 4U 1820-30 (Wijnands et al., 1999; Belloni et al., 2004) is consistent with a $n = 1$ $l = 2$ g -mode in a lighter ocean. In a lighter ocean, such as those considered in Bildsten & Cutler (1995), g -mode frequencies are larger by a factor of $\sim (56/16)^{1/2}$ compared to those studied here. This may explain the observed oscillations in 4U 1820-30, where accretion from the helium companion star (Wijnands et al., 1999) would result in a different ocean composition than the one considered here.

4.4 Late Time Cooling and Nuclear Pasta

As discussed in Section 4.2, as a neutron star cools in quiescence the X-ray light curve reveals layers with increasingly longer thermal times. For the cooling front to reach the deepest layers of the inner crust, close to the crust-core transition, the neutron star must cool for $\gtrsim 1000$ days. Though many quiescent neutron stars experience a new accretion outburst before cooling entirely, one cooling neutron star transient MXB 1659-29 cooled for $\gtrsim 2500$ days and allows a unique view of the inner crust's thermal properties.

Following the outburst and return to quiescence of MXB 1659-29 (Wijnands et al., 2003, 2004; Cackett et al., 2008), crust thermal relaxation models of MXB 1659-29 (Brown & Cumming, 2009) initially indicated that the outer layers in this source had returned to thermal equilibrium with the core, as suggested by a plateau in the quiescent luminosity after ≈ 1000 days in quiescence. A recent observation of MXB 1659-29 (Cackett et al., 2013), however, demonstrates that cooling continued after ≈ 2500 days into quiescence, suggesting that thermal equilibrium with the core had not yet been established. Cooling at late times near ≈ 2500 days corresponds to cooling layers deep in the neutron star's inner crust near a mass density $\rho \sim 10^{13} \text{ g cm}^{-3}$, densities predicted for the formation of nuclear pasta.

In the high density environment of the inner neutron star crust, nuclei are distorted into various shapes, called *nuclear pasta* (Ravenhall et al., 1983; Hashimoto et al., 1984). Nuclear pasta has been studied using quantum molecular dynamics simulations (Maruyama et al., 1998; Watanabe et al., 2003) and semi-classical molecular dynamics simulations (Horowitz et al., 2004a; Horowitz & Berry, 2008; Schneider et al., 2013), but the thermal properties of nuclear pasta remain uncertain (Horowitz et al., 2015). Because the quiescent light curve reveals successively deeper layers with time, the cooling light curve thousands of days into quiescence is affected by the thermal properties

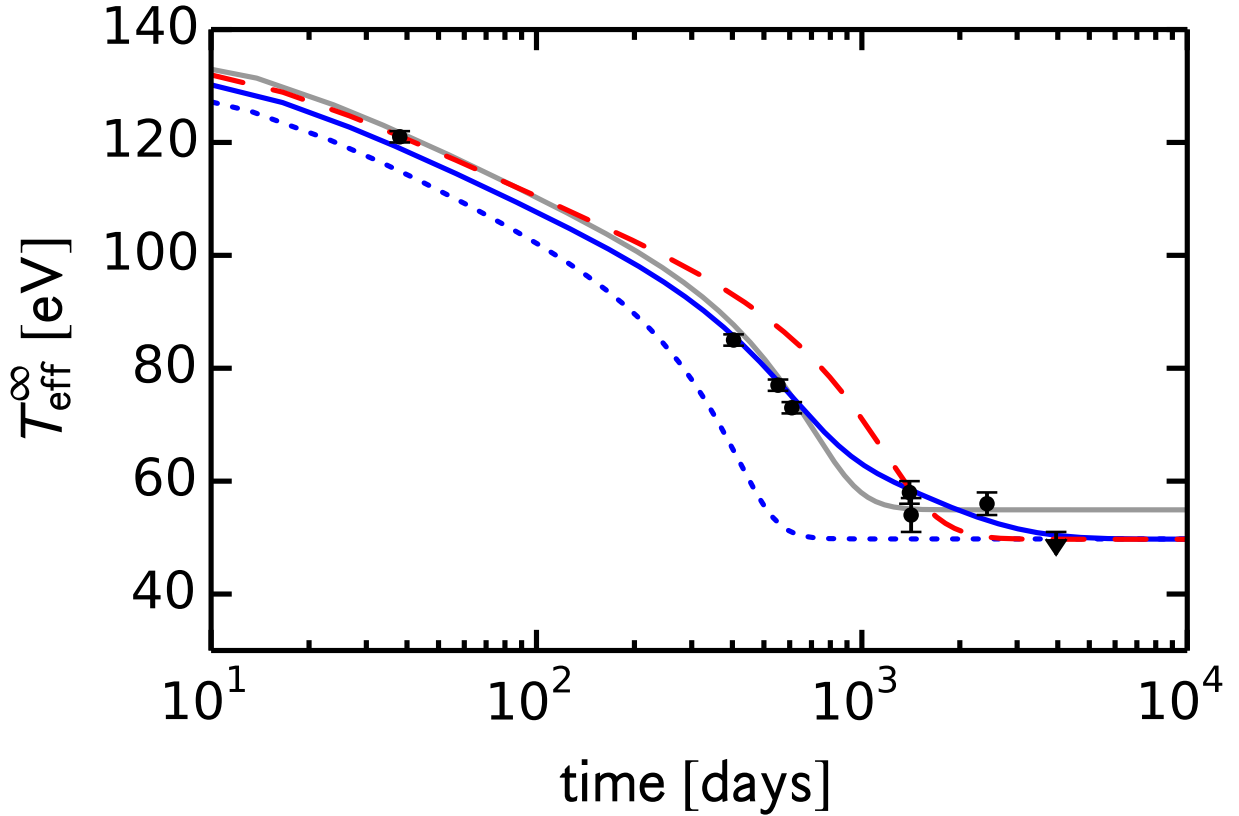


Figure 4.11: Crust cooling models of the late time cooling of MXB 1659-29. Cooling models for MXB 1659-29. The solid gray curve is a model that uses $Q_{\text{imp}} = 2.5$ throughout the entire crust and $T_{\text{core}} = 4 \times 10^7$ K. The solid blue curve is a model with $Q_{\text{imp}} = 20$ for $\rho > 8 \times 10^{13}$ g cm $^{-3}$, $Q_{\text{imp}} = 1$ for $\rho < 8 \times 10^{13}$ g cm $^{-3}$, $T_{\text{core}} = 3.25 \times 10^7$ K, and using the G08 pairing gap. The dashed red curve uses the same Q_{imp} as the solid blue curve, but with the S03 pairing gap. The dotted blue curve is a model with the G08 pairing gap and $Q_{\text{imp}} = 1$ throughout the crust, but without a low thermal conductivity pasta layer.

of the nuclear pasta in the deep inner crust. Horowitz et al. (2015) show that a low thermal conductivity layer may explain the late time cooling of MXB 1659-29, and that spiral defects may lower the pasta's thermal conductivity. This prediction is consistent with the low electrical conductivity of pasta that may explain the cutoff in the spin period distribution of pulsars at $P \sim 10$ s (Pons et al., 2013).

To investigate the impact of a pasta layer on the late time quiescent light curve of MXB 1659-29, we run a model of the MXB 1659-29 outburst using the best fit parameters from Brown & Cumming (2009): an accretion outburst lasting 2.5 years at a local mass accretion rate $\dot{m} \approx 0.1 \dot{m}_{\text{Edd}}$ where $\dot{m}_{\text{Edd}} \approx 8.8 \times 10^4 \text{ g cm}^{-2} \text{ s}^{-1}$ is the local Eddington mass accretion rate, a neutron star mass $M = 1.6 M_{\odot}$, a neutron star radius $R = 11.2 \text{ km}$, and a core temperature $T_{\text{core}} = 2.6 \times 10^7 \text{ K}$. The impurity parameter is defined for two separate regions: 1) for the crust $Q_{\text{imp}} = 3.5$ following Brown & Cumming (2009) and only impacts the thermal conductivity in the inner crust where $T < T_p$, and 2) a pasta layer with a second impurity parameter Q_{pasta} defined at mass densities $\rho > 8 \times 10^{13} \text{ g cm}^{-3}$ and extending to the crust-core transition.

The light curve from our standard model without pasta can be seen in Figure 4.11. In this model the crust reaches thermal equilibrium with the core by ≈ 1000 days into quiescence, and so predicts a constant temperature at later times. We also show two models with an impure inner crust with $Q_{\text{pasta}} = 25$. One of these corresponds to the model in Horowitz et al. (2015) and shows a long decline in temperature even at times as late as ≈ 2000 days. The other impure crust models, however do not show a decline at late times, but instead level off. The difference in the light curves is in the assumed $T_c(\rho)$ profiles, which are shown in Figure 4.12. Significant late time cooling only occurs if there is a normal layer of neutrons at the base of the crust, giving a large heat capacity there. The pasta layer maintains a temperature difference of $\Delta T \approx 3 \times 10^7 \text{ K}$ between the inner crust and core during the outburst. As a consequence, normal neutrons with a long thermal time

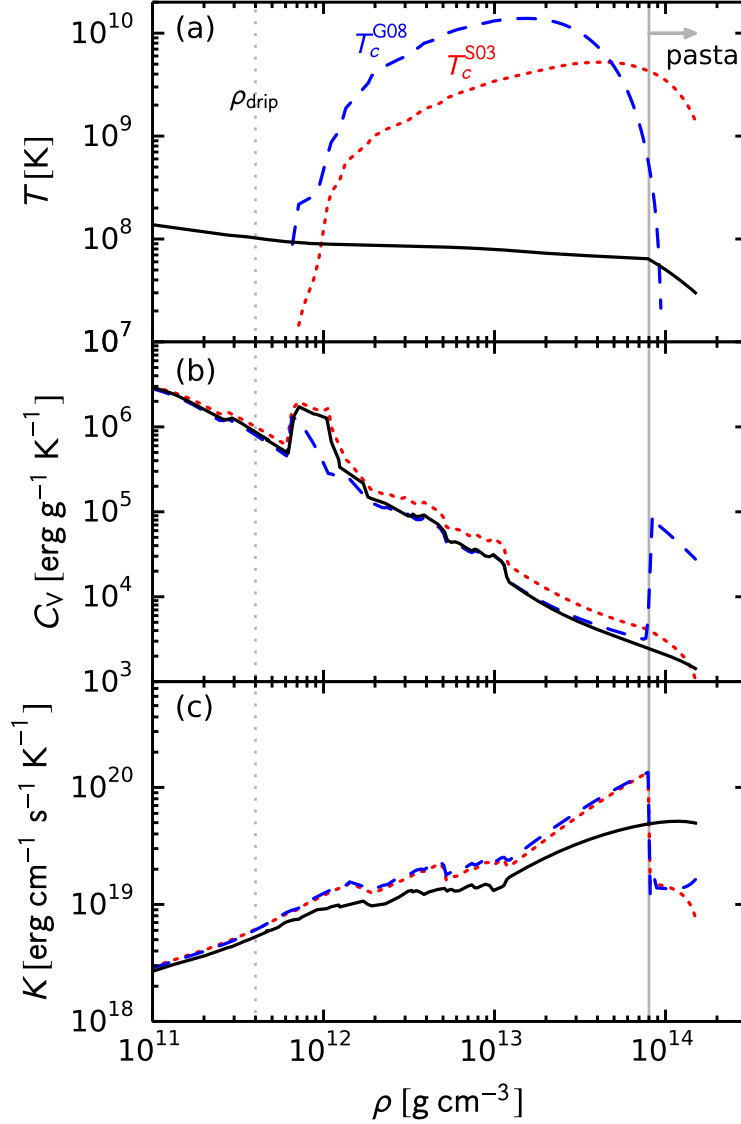


Figure 4.12: Thermal transport in the inner crust of MXB 1659-29 at the start of quiescence. The gray vertical lines indicate the neutron drip density and the transition to nuclear pasta. *Panel (a)*: The temperature profile (solid curve) corresponding to the cooling model in Figure 4.11 with a $Q_{\text{imp}} = 20$ pasta layer and the G08 pairing gap. The dashed curves show two choices for $T_c(\rho)$; the blue dashed curve corresponds to G08 and the red dotted curve is S03. *Panel (b)*: The heat capacity profiles for the same models as Figure 4.11. Solid black curve: $Q_{\text{imp}} = 3.7$ throughout the inner crust. Dashed blue curve: $Q_{\text{imp}} = 20$ for $\rho > 8 \times 10^{13} \text{ g cm}^{-3}$ and $Q_{\text{imp}} = 1$ for $\rho < 8 \times 10^{13} \text{ g cm}^{-3}$ using the G08 pairing gap that closes in the crust. Dotted red curve: same as dashed curve, but with a different choice for $T_c(\rho)$ from the S03 pairing gap that closes in the core. *Panel (c)*: Thermal conductivity profiles for the same models.

appear at the base of the crust that cause late time cooling if the neutron singlet pairing gap closes in the crust. Without normal neutrons at the base of the crust, as is the case if the neutron singlet pairing gap closes in the core, the crust reaches thermal equilibrium with the core after ≈ 3000 d and late time cooling is removed.

Some analytic estimates are useful to understand why the late time cooling occurs, and the crucial role of the normal neutron layer. First, we consider the temperature contrast ΔT between the inner crust and the core that develops during the accretion outburst (see panel (a) of Figure 4.12). This is set by the value at which the heat flux through the pasta layer balances the nuclear heating in the crust (mostly located at shallower densities near the neutron drip region). The heating rate is $\epsilon_{\text{nuc}} = \dot{m}E_{\text{nuc}}$ where $E_{\text{nuc}} \approx 2$ MeV per accreted nucleon. The equivalent heat flux is $F_{\text{in}} \approx 2 \times 10^{22}$ erg cm $^{-2}$ s $^{-1}$ for an accretion rate of $\dot{m} = 0.1 \dot{m}_{\text{Edd}}$.

The heat flux through the pasta layer is $F \approx K\Delta T/H$, where K is the thermal conductivity and H the pressure scale height. Neutrons set the pressure in the inner crust, so that¹ $H = P/\rho g \approx 7 \times 10^4$ cm ($\rho_{14}^{2/3} Y_n^{5/3}/g_{14}$) where Y_n is the neutron fraction, ρ_{14} is the mass density in units of 10^{14} g cm $^{-3}$, and the surface gravity of the neutron star is $g = (GM/R^2)(1-2GM/Rc^2)^{-1/2}$ in units of 10^{14} cm s $^{-2}$. As can be seen in Figure 4.13, the thermal conductivity is primarily set by electron-impurity scattering (Equation 2.33) because neutron-impurity scattering only becomes comparable to electron scattering very close to the crust-core transition. The resulting thermal conductivity from electron-impurity scattering is given in Equation 2.35. Therefore, the temperature difference between inner crust and core is

$$\Delta T \approx 3 \times 10^7 \text{ K} \left[\frac{\rho_{14}^{1/3}}{g_{14} T_8} \frac{Y_n^{5/3}}{(Y_e/0.05)^{1/3}} \left(\frac{Q_{\text{imp}} \Lambda_e Q}{\langle Z \rangle} \right) \left(\frac{\dot{m}}{0.1 \dot{m}_{\text{Edd}}} \right) \right], \quad (4.11)$$

¹In the inner crust, $\Gamma_1 \equiv (\partial \ln P / \partial \ln \rho)_s$ varies with density: at first Γ_1 decreases below 4/3 (the value for degenerate relativistic electrons) and then it increases for $\rho \gtrsim 10^{13}$ g cm $^{-3}$ and approaches $\Gamma_1 \lesssim 2$ at roughly nuclear density. For definiteness in computing H , we set $\Gamma_1 = 5/3$.

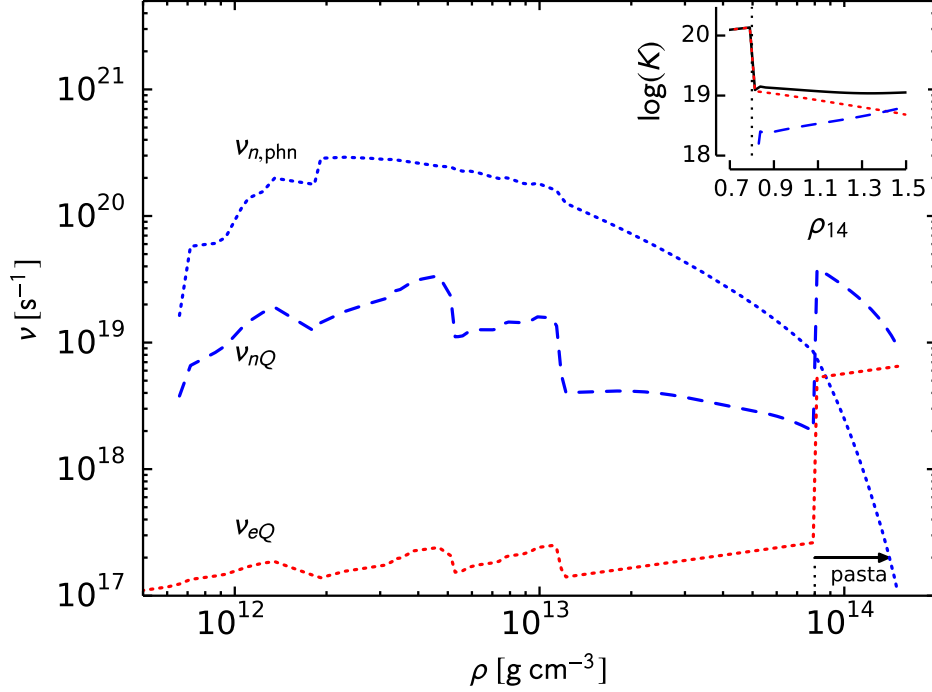


Figure 4.13: Scattering frequencies for electrons and neutrons in the inner crust at the beginning of quiescence for the model with $Q_{\text{imp}} = 20$ at $\rho > 8 \times 10^{13} \text{ g cm}^{-3}$, $Q_{\text{imp}} = 1$ at $\rho < 8 \times 10^{13} \text{ g cm}^{-3}$, and the pairing gap that closes in the crust (Gandolfi et al., 2008). *Subplot*: Thermal conductivity K from electron scattering (dotted red curve), neutron scattering (dashed blue curve), and from both electrons and neutrons (solid black curve). The mass density ρ is given in units of $10^{14} \text{ g cm}^{-3}$. The region containing nuclear pasta is to the right of the vertical black dotted line.

which is in reasonable agreement with the temperature jumps seen in Figure 4.12, panel (a), between $\rho \approx 8 \times 10^{13} \text{ g cm}^{-3}$ and $\rho \approx 1.5 \times 10^{14} \text{ g cm}^{-3}$.

Page & Reddy (2012) pointed out that differences in $T_c(\rho)$ and the resulting presence or absence of a layer of normal neutrons at the base of the crust could affect the cooling curves at late times ≈ 1000 days into cooling. We find a much larger effect and on a longer timescale here because the low thermal conductivity of the nuclear pasta layer keeps the inner crust much hotter during the outburst. During quiescence, the base of the crust remains at a higher temperature than the core for ≈ 5000 days (see Equation 4.11). The temperature difference between the crust and core results in a slow decline of the quiescent light curve after $\gtrsim 1000$ days, as can be seen in Figure 4.11.

Late time cooling in MXB 1659-29 requires that the 1S_0 neutron singlet pairing gap close

in the crust. As a result, superfluid neutrons are confined to the inner crust shallower than the pasta layer at $\rho \lesssim 8 \times 10^{13} \text{ g cm}^{-3}$ where $T \ll T_c$. By contrast, a recent study of pulsar glitches suggests that the neutron superfluid extends from the crust into the core continuously (Andersson et al., 2012). Recent calculations of the neutron effective mass in a non-accreted ($Q_{\text{imp}} = 0$) crust suggest that $m_n^\star \gg m_n$ at the base of the crust (Chamel, 2005, 2012). In this case, a larger fraction of free neutrons are entrained in the inner crust and the neutron superfluid must then extend into the core to supply adequate inertia for pulsar glitches (Andersson et al., 2012; Ho et al., 2015). We note, however, that the above calculation for the neutron effective mass is likely inappropriate for the impure crust compositions found in the accreting transients studied here. Therefore, we here assume $m_n^\star \approx m_n$ as found in Brown (2013) in the absence of neutron effective mass calculations in an accreted crust.

Chapter 5

Urca Cooling Nuclei Pairs

Neutrino emission through cycles of e^- -capture and β^- -decay, or “Urca” cycles, was first proposed as a cooling process relevant for stellar collapse (Gamow & Schoenberg, 1940). An Urca cycle occurs when an e^- -capture daughter nucleus undergoes β^- -decay on a timescale much shorter than other possible nuclear reactions, producing the cycle



where Z is the proton number and A is the mass number of the e^- -capture parent nucleus. The e^- -capture parent and the e^- -capture daughter thereby form an *Urca pair*. Neutrinos liberate a majority ($\gtrsim 2/3$) of the e^- -capture threshold energy Q_{EC} (Gamow & Schoenberg, 1940; Haensel & Zdunik, 1990) which escape from the star entirely due to the large mean free path of the neutrino. The strong T^5 dependence of the Urca cycling neutrino emission means that Urca cooling becomes important in high-temperature systems. For example, Urca cooling has been studied in the context of white dwarfs interiors at temperatures near $\sim 10^9$ K (Tsuruta & Cameron, 1970). As we will show, Urca cycles occur in the neutron star interior and become an important cooling mechanism in accreting neutron stars that reach temperatures $T \gtrsim 10^8$ K in their oceans and crusts.

5.1 Urca Pair Formation

An accretion outburst in a neutron star transient deposits hydrogen- and helium-rich material into the neutron star's envelope. As the envelope temperature rises, accreted hydrogen-rich and helium-rich material in the envelope may eventually ignite unstably, powering a type-I X-ray burst. Burning in type-I X-ray bursts proceeds via the rapid proton-capture process (Fujimoto et al., 1981; Wallace & Woosley, 1981) which produces an array of neutron-rich nuclei and a significant amount of carbon (Schatz et al., 1999); for example, unstable nuclear burning typically produces nuclei with masses $A \sim 60\text{--}100$ in Type I X-ray bursts (Schatz et al., 1998, 2001; Brown et al., 2002; Schatz et al., 2003; Woosley et al., 2004; Cyburt et al., 2010). The accumulation of more accreted material in the neutron star's envelope compresses the carbon-rich layer deeper in the star. Eventually, the ambient density and temperature are sufficient to ignite the $^{12}\text{C} + ^{12}\text{C}$ fusion reaction, triggering a superburst in the envelope (Schatz et al., 2003), and producing ashes in the same mass regime (Keek & Heger, 2011; Keek et al., 2012). Note that stable nuclear burning in hot neutron star envelopes $\gtrsim 5 \times 10^8$ K also produces nuclei of similar masses (Schatz et al., 1999).

The accumulation of material in the envelope by subsequent accretion outbursts compresses the ashes of nuclear burning deeper into the neutron star. Nuclear reaction network calculations that follow the compressed ashes of nuclear burning found that ashes contain Urca pairs that become active in the neutron star crust (Schatz et al., 2014). Urca pairs had previously been considered as a coolant in neutron stars (Bahcall & Wolf, 1965), but were not found in nuclear reaction network calculations of the accreted crust. Nuclear reaction network calculations of the accreted crust were previously done in the zero temperature approximation, which is typically a valid assumption for e^- -captures in the degenerate electron gas where $\mu_e \gg k_B T$. At zero temperature, e^- -captures occur when $\mu_e > |Q_{\text{EC}}|$ and β^- -decays are blocked because electron phase space is restricted.

Urca reaction shells will appear if the network uses a finite temperature instead of the zero temperature approximation (Schatz et al., 2014). At finite temperature, e^- -captures occur when $|Q_{\text{EC}}| - k_{\text{B}}T \lesssim \mu_e \lesssim |Q_{\text{EC}}| + k_{\text{B}}T$ and β^- -decays are allowed. These reactions occur in an Urca “shell” with a thermal width $\mu_e \pm k_{\text{B}}T$, or $(\Delta R)_{\text{shell}} \approx Y_e k_{\text{B}}T / m_u g$ (Cooper et al., 2009; Schatz et al., 2014). A schematic of an Urca reaction layer in a neutron star is shown in Figure 5.1.

Following the approach of Tsuruta & Cameron (1970), in the relativistic limit ($\mu_e \approx E_{\text{F}} \gg m_e c^2$) the specific neutrino emissivities from e^- -captures (+) and β^- -decays (−) in the degenerate electron ocean are

$$\epsilon_{\nu}^{\pm} \approx m_e c^2 \left(\frac{\ln 2}{ft} \right) \langle F \rangle^{\pm} n^{\pm} I^{\pm}(E_{\text{F}}, T), \quad (5.3)$$

where n^{\pm} is the number density of nuclei, $\alpha \approx 1/137$ is the fine structure constant, and the Coulomb factor can be expressed as $\langle F \rangle^{\pm} \approx 2\pi\alpha Z / |1 - \exp(\mp 2\pi\alpha Z)|$. The electron phase space integrals are

$$I^+(E_{\text{F}}, T) = \int_{W_m}^{\infty} W \sqrt{W^2 - 1} (W - W_m)^3 S dW, \quad (5.4)$$

$$I^-(E_{\text{F}}, T) = \int_1^{W_m} W \sqrt{W^2 - 1} (W_m - W)^3 (1 - S) dW, \quad (5.5)$$

where $W \equiv E_e / m_e c^2$ is the electron energy, $W_m \equiv |Q_{\text{EC}}| / m_e c^2$ is the electron capture threshold energy, $S = (1 + \exp[(E_e - E_{\text{F}}) / k_{\text{B}}T])^{-1}$ is the statistical factor, and $E_{\text{F}} \approx 3.7 \text{ MeV} (\rho_9 Y_e / 0.4)^{1/3}$ is the electron Fermi energy, and $\rho_9 \equiv \rho / (10^9 \text{ g cm}^{-3})$. The total neutrino luminosity in the Urca shell is found by integrating the sum of the specific neutrino emissivities from e^- -captures and β^- -decays over the reaction shell,

$$L_{\nu} \approx 4\pi R^2 \int_{\text{shell}} (\epsilon_{\nu}^+ + \epsilon_{\nu}^-) dz', \quad (5.6)$$

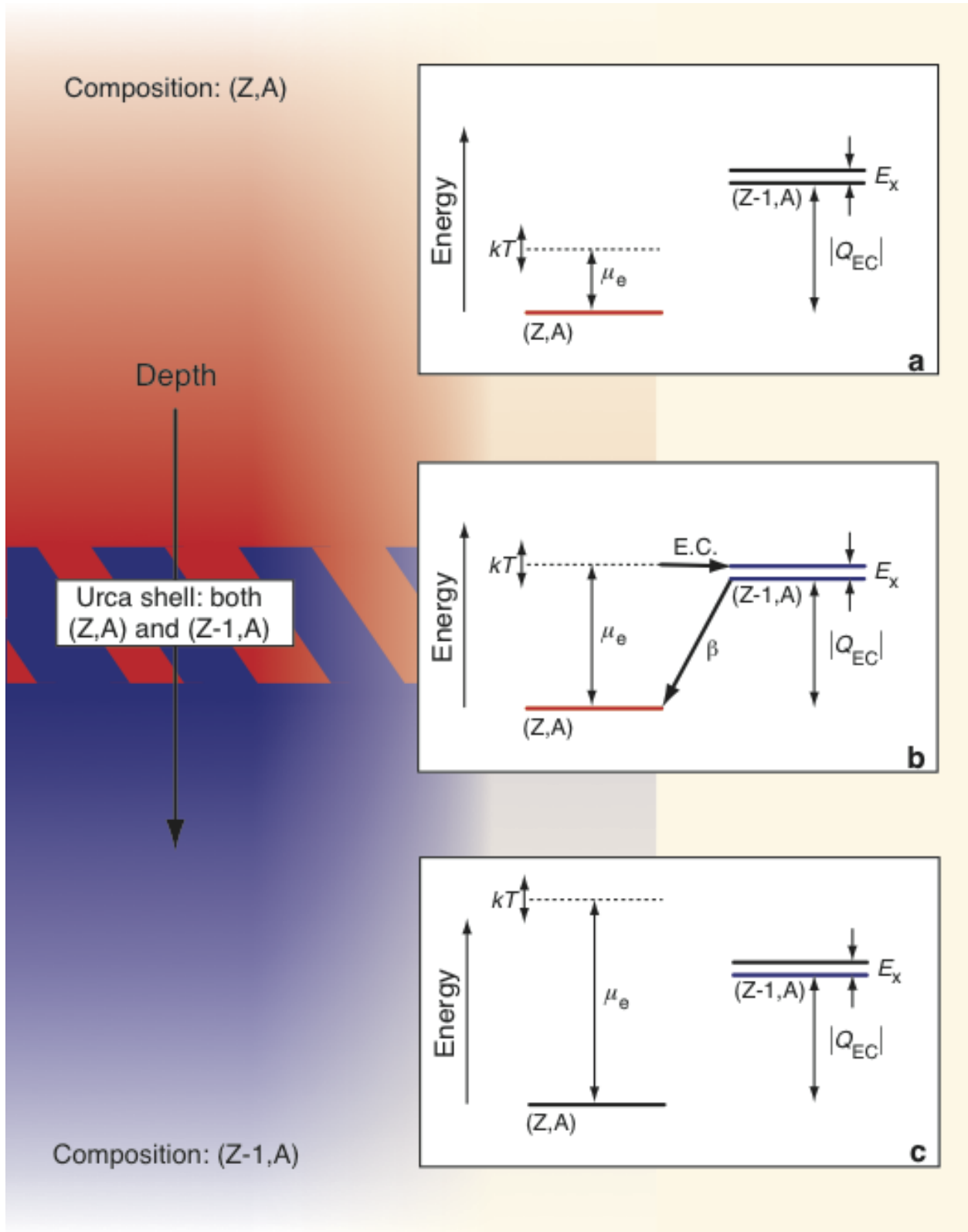


Figure 5.1: Schematic of an Urca reaction shell. The red colored region is composed of the parent nucleus, which electron captures into the daughter nucleus represented by the blue colored region. The Urca reaction layer has a thermal width $Q_{EC} \pm k_B T$, where $\mu_e \approx Q_{EC}$ is the center of the Urca shell.

where R is the radius of the neutron star. The Urca cycle occurs over a thin shell defined by the temperature $(\Delta R)_{\text{shell}} \approx Y_e k_B T / m_u g$ (Cooper et al., 2009; Schatz et al., 2014) where $(\Delta R)_{\text{shell}} \ll R$, $Y_e \approx Z/A$ is the electron fraction, and the surface gravity of the neutron star is $g = GM/R^2$. The integral in Equation 5.6 can be solved analytically by transforming the integration variable $dz' \approx (dP/d\mu_e)(d\mu_e/\rho g)$. The approximate neutrino luminosity in the Urca shell is

$$L_\nu \approx L_{34} \times 10^{34} \text{ ergs s}^{-1} X T_9^5 \left(\frac{g_{14}}{2}\right)^{-1} R_{10}^2, \quad (5.7)$$

where the parameter L_{34} is a function of nuclear properties only,

$$L_{34} = 2.15 \left(\frac{10^6 \text{ s}}{ft}\right) \left(\frac{56}{A}\right) \left(\frac{Q_{\text{EC}}}{4 \text{ MeV}}\right)^5 \left(\frac{\langle F \rangle^*}{0.5}\right), \quad (5.8)$$

and we define the parameters: $T_9 \equiv T/(10^9 \text{ K})$, $g_{14} \equiv g/(10^{14} \text{ cm s}^{-2})$, $R_{10} \equiv R/(10 \text{ km})$, $\langle F \rangle^* \equiv \langle F \rangle^+ \langle F \rangle^- / (\langle F \rangle^+ + \langle F \rangle^-)$, and $X \equiv Am_{un}/\rho$ is the mass fraction of the parent nucleus in the composition.

5.2 Crust Urca Pairs

A nuclear reaction network calculation that follows compressed X-ray burst and superburst ashes found Urca pairs form in the neutron star crust (Schatz et al., 2014). Schatz et al. (2014) found that the presence of Urca pairs is robust for X-ray burst and superburst ashes. Furthermore, at large enough abundances neutrino cooling from Urca pairs in the crust balances accretion-driven heating at crust temperatures $\gtrsim 2 \times 10^8 \text{ K}$. The Urca pairs in the crust with the strongest neutrino luminosities are shown in Table 5.1. Because Urca cooling may balance accretion-driven heating, Urca pairs may leave observational signatures in the cooling light curves of neutron star transients

Table 5.1: Urca pairs in the neutron star crust (Schatz et al., 2014).

Urca pair		ρ	μ_e	L_{34}	$X \cdot L_{34}$	$X \cdot L_{34}$
parent	daughter	[$10^{10} \text{ g cm}^{-3}$]	[MeV]	[$X = 1$]	[X_{XRB}]	[X_{SB}]
^{29}Mg	^{29}Na	4.79	13.3	4.5×10^4	8.2	< 0.1
^{55}Ti	$^{55}\text{Sc}, ^{55}\text{Ca}$	3.73	12.1	2.0×10^4	95	370
^{31}Al	^{31}Mg	3.39	11.8	1.6×10^4	46	< 0.1
^{33}Al	^{33}Mg	5.19	13.4	1.5×10^4	80	< 0.1
^{56}Ti	^{56}Sc	5.57	13.8	3.5×10^3	—	—
^{57}Cr	^{57}V	1.22	8.3	3.0×10^3	12	4.9
^{57}V	$^{57}\text{Ti}, ^{57}\text{Sc}$	2.56	10.7	3.0×10^3	12	4.9
^{63}Cr	^{63}V	6.82	14.7	1.8×10^3	17	< 0.1
^{105}Zr	^{105}Y	3.12	11.2	1.7×10^3	< 0.1	0
^{59}Mn	^{59}Cr	9.45	7.6	1.6×10^3	7.4	0.51
^{103}Sr	^{103}Rb	5.30	13.3	1.2×10^3	< 0.1	0
^{96}Kr	^{96}Br	6.40	14.3	1.2×10^3	0.15	0
^{65}Fe	^{65}Mn	2.34	10.3	1.1×10^3	17	< 0.1
^{65}Mn	^{65}Cr	3.55	11.7	8.6×10^2	13	< 0.1

and may impact superburst ignition.

5.2.1 Impact on Neutron Star Transients

During an accretion outburst, the crust of a neutron star transient is heated out of thermal equilibrium with the core and can reach temperatures where Urca cooling becomes important. When accretion halts, a cooling wave propagates inward and the thermal emission powers the quiescent light curve (Rutledge et al., 2002). Features in the crust temperature profile, such as local temperature dips caused by neutrino cooling, may be revealed in the quiescent light curve. The strength of Urca cooling depends on the temperature reached during steady state in the neutron star crust.

In particular, the best candidates to possibly confirm the existence of Urca cooling are neutron star quasi-persistent transients (see Chapter 4) where accretion rates near the Eddington accretion rate ($\dot{M}_{\text{Edd}} \approx 2 \times 10^{-8} M_{\odot} \text{ yr}^{-1}$) raise the neutron star's temperature significantly. Of particular interest is the neutron star transient MAXI J0556-332 (hereafter MAXI; Homan et al. 2014)

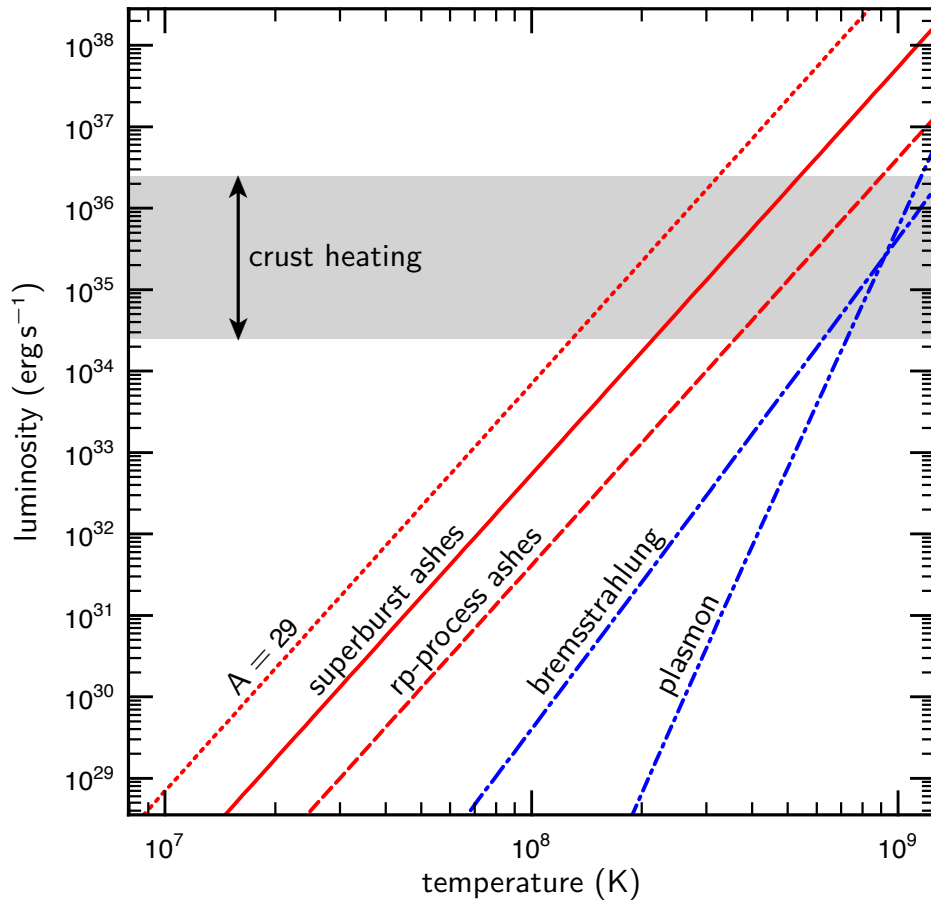


Figure 5.2: Luminosity sources in the neutron star crust as a function of crust temperature. The red curves indicate the neutrino luminosities from Urca pairs. Blue curves indicate neutrino cooling from other processes in the neutron star crust. The gray shaded region indicates the heating luminosity from crustal heating.

which is the hottest neutron star transient and reaches $T \approx 2 \times 10^9$ K in the crust (Deibel et al., 2015) - making it an ideal testing ground for Urca cooling pairs. Here we detail the work done in Deibel et al. (2015), where the quiescent observations from MAXI are compared against light curve models with Urca pairs in the neutron star crust.

We fit the quiescent light curve of MAXI J0556-332 using the thermal evolution code dStar. The best fit model is discussed in Section 4.2.1, with $M = 1.5 M_{\odot}$, $R = 11$ km, and $Q_{\text{shallow}} = 6.0$ MeV per accreted nucleon. The best fit curve can be seen in Figure 5.3. As noted in Section 5.1, Urca cooling pairs have two major impacts on the temperature of the crust during an accretion episode. First, the Urca pair cools the crust *locally* through the emission of energy in the form of neutrinos. Second, the Urca pair thermally decouples layers above and below the reaction layer because heat is only conducted *into* the layer, not *across* the layer. In the case of MAXI, the thermal decoupling most significantly impacts the shape of the quiescent light curve, as can be seen in Figure 5.3. The observed MAXI light curve decreases monotonically for hundreds of days and the cooling front has had time to enter the inner crust. If Urca cooling were present in MAXI, the crust below the shallow heat source ($\rho > \rho_h$) is thermally decoupled from the shallow heat source near $\rho \sim 10^{10}$ g cm⁻³ by Urca cooling pairs present between $\rho \sim 10^{10} - 10^{11}$ g cm⁻³. As a result, the light curve “dips” as the cooling front moves deeper than the shallow heat source; that is, the light curve after ≈ 20 days into quiescence.

5.2.2 Impact on Neutron Star Superbursts

Superbursts are powerful X-ray bursts thought to be triggered by unstable carbon ignition in the neutron star envelope (Woosley & Taam, 1976; Fujimoto et al., 1981; Cumming & Bildsten, 2001; Strohmayer & Brown, 2002a). Superbursts are observed in neutron stars with accretion rates between $\approx 0.1-0.3 \dot{M}_{\text{Edd}}$ (Wijnands, 2001) with inferred ignition depths between

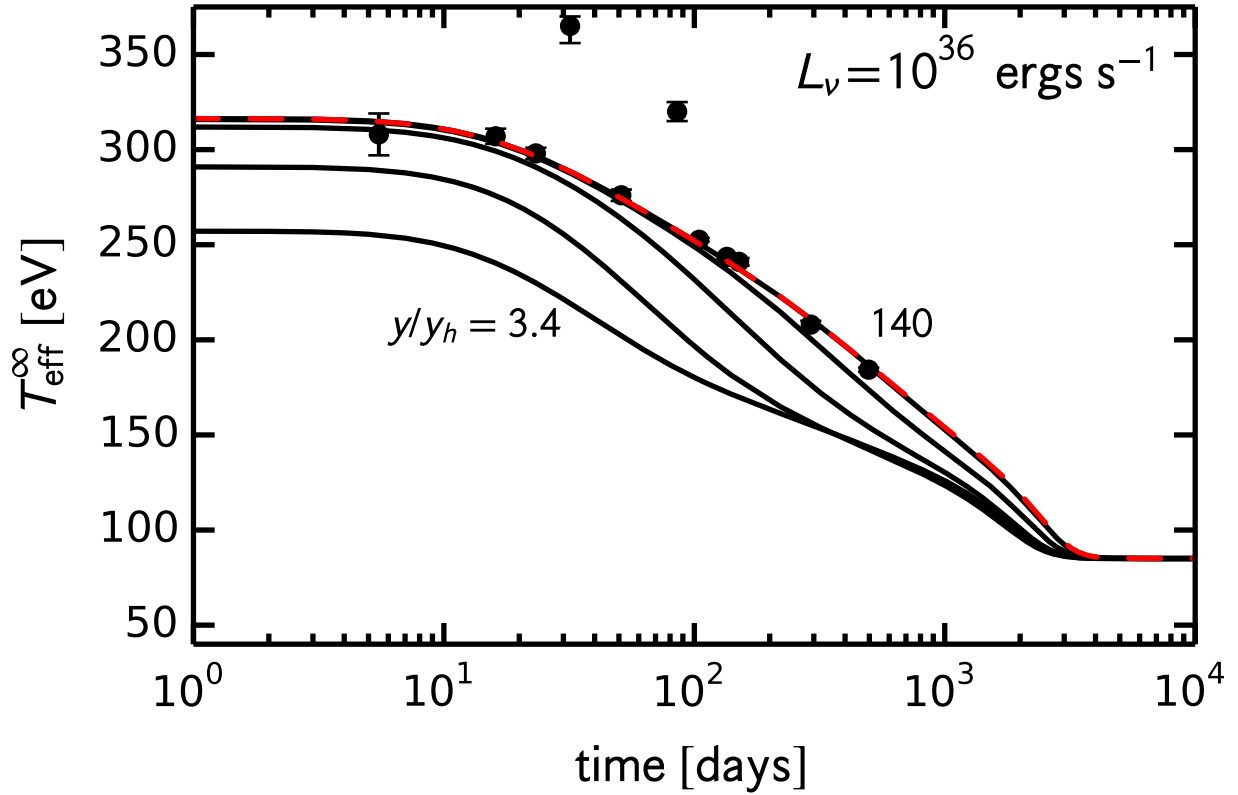


Figure 5.3: Quiescent lightcurve of the neutron star MAXI J0556-332. The crust model is for a $M = 1.5 M_{\odot}$, $R = 11$ km neutron star with $Q_{\text{shallow}} = 6.0$ MeV. The light curve without Urca cooling is shown as a red dashed curve. Model light curves with Urca pairs, with $L_{\nu} = 10^{36}$ ergs s^{-1} , are shown as black curves. From left to right, shell depths are $y/y_h = 3.4, 6.7, 17, 43, 140$, that correspond to $\rho_{10} = 3, 5, 10, 20, 50$, respectively.

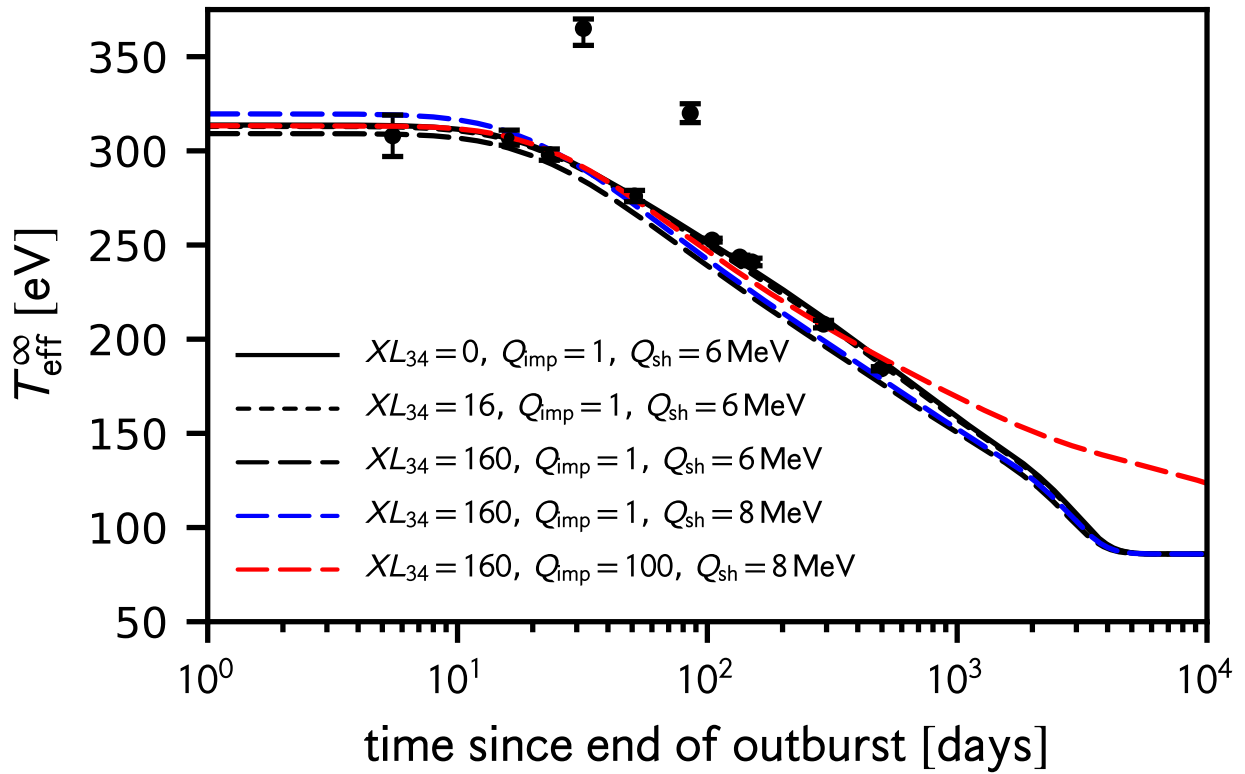


Figure 5.4: Quiescent lightcurve of the neutron star MAXI J0556-332 with an ^{33}Al Urca shell. The crust model is for a $M = 1.5 M_{\odot}$, $R = 11 \text{ km}$ neutron star with $Q_{\text{shallow}} = 6.0 \text{ MeV}$.

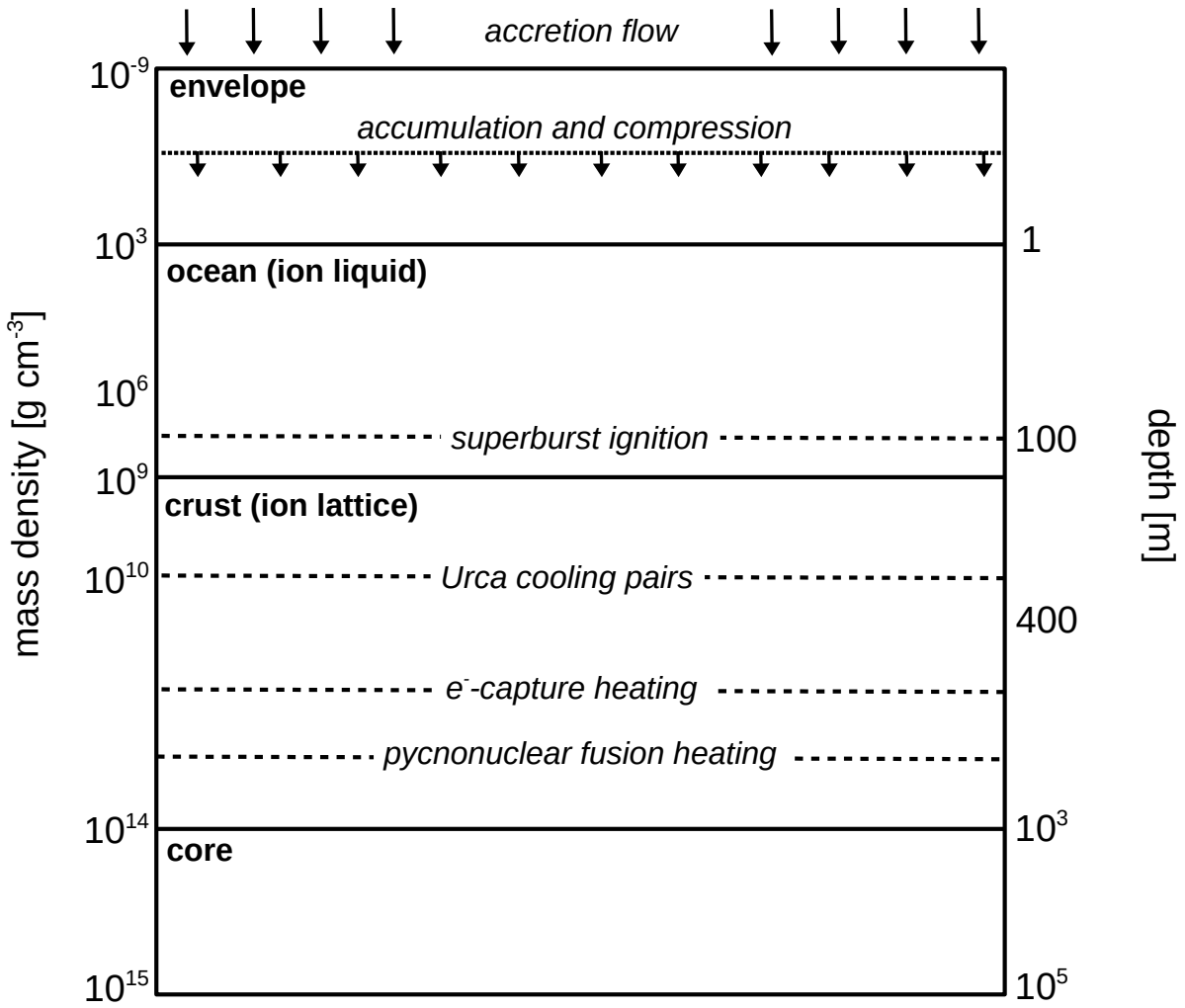


Figure 5.5: Schematic of the neutron star's outer layers and the location of superburst ignition and Urca cooling pairs.

Table 5.2: Properties of the strongest Urca e^- -capture parents identified in Meisel & Deibel (2017) and in Schatz et al. (2014), absent even- A nuclides, excluded by Meisel et al. (2015); Deibel et al. (2016).

Parent	$ Q_{\text{EC}} $ (MeV)	$\log(ft)$	L_{34}	X_{XRB}	X_{SB}	X_{S}
^{29}Mg	13.3	5.1	8.2E+3	2.1E-3	1.9E-6	1.6E-4
^{31}Al	11.8	4.9	4.2E+3	3.8E-3	4.3E-6	3.4E-4
^{33}Al	13.4	5.2	3.7E+4	4.3E-3	4.0E-6	8.8E-5
^{55}Sc	12.1	4.9	2.4E+3	3.8E-3	1.8E-2	1.3E-3
^{57}Cr	8.3	11.6	8.6E-5	1.2E-3	1.6E-3	1.7E-3
^{57}V	10.7	4.9	1.2E+3	1.2E-3	1.6E-3	1.7E-3
^{59}Mn	7.6	11.6	5.2E-5	2.8E-3	3.1E-4	2.3E-3
^{63}Cr	14.7	14.4	1.1E-6	6.5E-3	6.5E-9	3.6E-3
^{65}Fe	10.3	11.6	2.1E-4	1.4E-2	4.2E-12	1.6E-2
^{65}Mn	11.7	11.6	4.1E-4	1.4E-2	4.2E-12	1.6E-2

$y_{\text{ign}} \approx 0.5\text{--}3 \times 10^{12} \text{ g cm}^{-2}$ (Cumming et al., 2006). Here we examine neutrino cooling from Urca pairs in the crust to determine the impact on carbon ignition conditions in the neutron star ocean.

During an accretion outburst, the accretion-driven crustal heating produces a heat flux into the overlying neutron star ocean. The $\approx 1\text{--}2$ MeV per accreted nucleon of heat deposited in the crust, however, is not sufficient to heat the ocean for superburst ignition at the depths observed. Superburst ignition models require an addition ≈ 1 MeV per accreted nucleon in the crust to provide ≈ 0.1 MeV per accreted nucleon extra heating into the ocean. This occurs because during steady state $\approx 90\%$ of crustal heating is transported toward the core (Brown, 2000). This extra heating is needed to have superbursts ignite at the observed ignition depths (Cumming & Bildsten, 2001; Cumming et al., 2006). Urca cooling pairs in the crust remove much of the heat flux entering the ocean from accretion-driven crustal heating.

We model the ocean temperature with and without crust Urca pairs to determine their impact on the ocean temperature and in turn their impact on unstable carbon ignition. We calculate the

neutron star ocean’s thermal evolution using the open source code `dStar`¹ which solves the general relativistic heat diffusion equation using the MESA numerical library (Paxton et al., 2011, 2013, 2015). The model has a neutron star mass $M = 1.4 M_{\odot}$, neutron star radius $R = 10$ km, and core temperature $T_{\text{core}} = 3 \times 10^7$ K. The neutron star accretes until the ocean temperature reaches steady state. The flux entering the ocean from the crust is $F = Q_b \dot{m}$, and we define Q_b at $y = 5 \times 10^{14}$ g cm⁻². As shown in Cumming et al. (2006), $Q_b \approx 0.25(\dot{m}/0.3 \dot{m}_{\text{Edd}})^{-1}$ is required for superburst ignition at $y = 10^{12}$ g cm⁻².

Runaway thermonuclear burning of carbon occurs when the local heating rate from carbon fusion ϵ_{C} and the local cooling rate ϵ_{cool} satisfy the condition $d\epsilon_{\text{C}}/dT > d\epsilon_{\text{cool}}/dT$. For the local heating rate from carbon burning, we use the $^{12}\text{C}+^{12}\text{C}$ reaction rate given by Caughlan & Fowler (1988) with screening by Ogata et al. (1993). The local cooling rate is given by $\epsilon_{\text{cool}} = \rho KT/y^2$ (Fujimoto et al., 1981) and approximates the heat lost through thermal diffusion. The unstable carbon ignition curve in an iron ocean with $X_{\text{C}} = 0.2$ is shown in Figure 5.9.

We run a neutron star model with a local accretion rate $\dot{m} = 0.3 \dot{m}_{\text{Edd}}$, the minimum accretion rate for ignition in an ocean with $X_{\text{C}} = 0.2$ (Cumming et al., 2006), where $\dot{m}_{\text{Edd}} \approx 8.8 \times 10^4$ g cm⁻² s⁻¹ is the local Eddington mass accretion rate. We place crust Urca pairs with $X \cdot L_{34} > 1$ from Table 5.1 into our superburst ignition model. We test several values of Q_{shallow} within constraints given by observations. For example, the neutron star transients MXB 1659-29 and KS 1731-260 require $Q_{\text{shallow}} \approx 1$ MeV during outburst to reconcile thermal evolution models with quiescent observations (Brown & Cumming, 2009). For the same reason, the hottest neutron star transient to date, MAXI J0556-332, requires $Q_{\text{shallow}} \approx 6\text{--}16$ MeV per accreted nucleon (Deibel et al., 2015). Specifically, we test $Q_{\text{shallow}} = 1, 5, 10, 15$ MeV per accreted nucleon that correspond to $Q_b = 0.1, 0.25, 1.0, 2.0$ MeV per accreted nucleon, respectively. The ocean temper-

¹<https://github.com/nworbde/dStar>

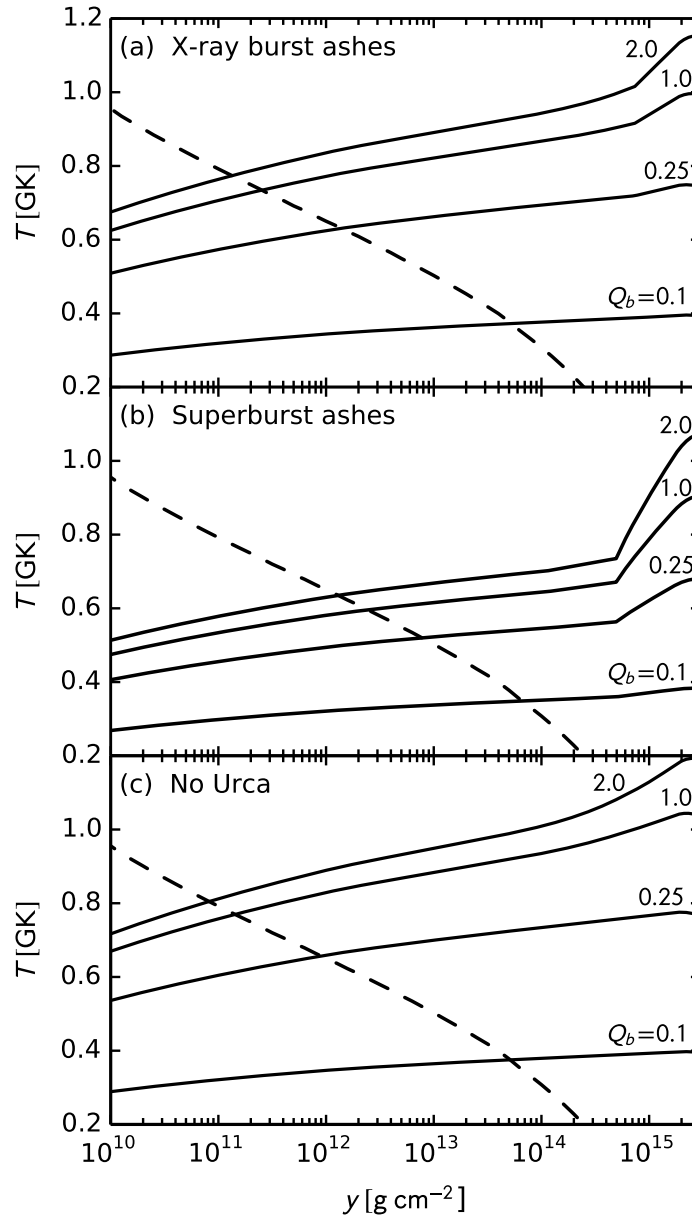


Figure 5.6: Ocean temperature profiles during steady state with Urca pairs in the crust for various values of Q_b . *Panel (a)*: Abundances of Urca pairs calculated from X-ray burst ashes. *Panel (b)*: Abundances of Urca pairs calculated from superburst ashes. *Panel (c)*: Ocean temperature profiles without Urca cooling in the crust.

ature profile for abundances of pairs in X-ray burst ashes (Woosley et al., 2004) and superburst ashes (Keek & Heger, 2011) is shown in Figure 5.6 for the different values of Q_b .

Crust Urca pairs are located deeper than superburst ignition at $y \gtrsim 10^{14} \text{ g cm}^{-2}$, but are shallower than deep crustal heating sources near $y \gtrsim 10^{16} \text{ g cm}^{-2}$, as shown schematically in Figure 5.5. As a consequence, crust Urca pairs impact carbon ignition depths by removing $\approx 80\text{--}90\%$ of the heat flux entering the ocean from crustal and extra heating. As a result, for all values of Q_b tested, carbon ignition occurs deeper than it would otherwise when crust Urca pairs are present. In a crust composed of X-ray burst ashes, the ocean temperature is limited to $T \lesssim 10^9 \text{ K}$ in the carbon ignition region and ignition depths are limited to $y_{\text{ign}} \gtrsim 2 \times 10^{11} \text{ g cm}^{-2}$. In a crust composed of superburst ashes, the ocean temperature is limited to $T \lesssim 7 \times 10^8 \text{ K}$ and carbon ignition depths are limited to $y_{\text{ign}} \gtrsim 2 \times 10^{12} \text{ g cm}^{-2}$. Once nuclear uncertainties are taken into account, allowed carbon ignition depths are $y_{\text{ign}} \gtrsim 10^{11} \text{ g cm}^{-2}$ ($y_{\text{ign}} \gtrsim 2 \times 10^{11} \text{ g cm}^{-2}$) in a crust composed of X-ray burst (superburst) ashes.

5.3 Ocean Urca Pairs

As first observed by Gamow (1941), some nuclei pairs emit neutrinos more efficiently than others, even if their abundance is small by comparison. This occurs because the Urca neutrino luminosity scales as Q_{EC}^5 and the neutrino luminosity will therefore vary between nuclei.

Here we focus on the complete identification of weaker Urca pairs in the $A < 106$ mass range (the highest mass produced in the rp -process) with $|Q_{\text{EC}}| \lesssim 5 \text{ MeV}$. These Urca cycles occur in the neutron star ocean, at column depths expected for superburst ignition $y_{\text{ign}} = P/g \approx 0.5\text{--}3 \times 10^{12} \text{ g cm}^{-2}$ (Cumming et al., 2006). We identify a total of 85 odd- A isotopes with experimentally determined mass excesses (Audi et al., 2012) which give Q_{EC} values accurate within $\approx 1\%$ or

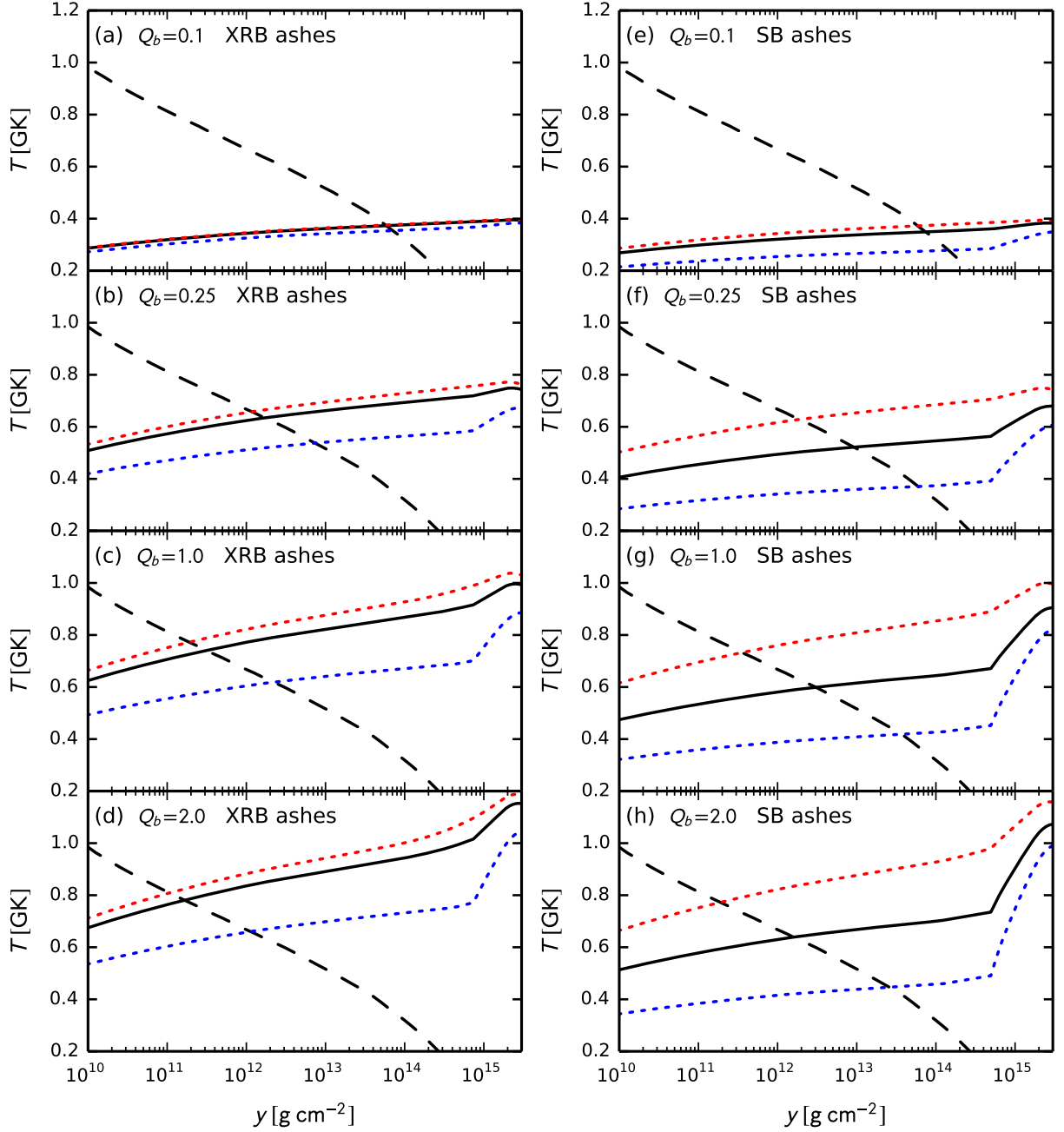


Figure 5.7: Ocean temperature profiles during steady state with Urca pairs in the crust for uncertainties in ft -values. We test the values $Q_b = 0.1, 0.25, 1, 2$ MeV per accreted nucleon. *Panels (a)–(d)*: Abundances of crust Urca pairs calculated from X-ray burst ashes. *Panels (e)–(h)*: Abundances of crust Urca pairs calculated from superburst ashes. The upper red-dashed curves are with ft -values enhanced by a factor of 10 and the lower blue-dashed curves are for ft -values reduced by a factor of 10.

better. In addition to ground-state to ground-state transitions, we include e^- -captures onto excited states with excitation energies $E_X \sim k_B T \sim 100 \text{ keV}$ for the typical temperatures near $\sim 10^9 \text{ K}$ in the ocean of superbursting neutron stars. Taken together with the study by Schatz et al. (2014) of Urca cooling pairs in the neutron star’s crust, this study completes a census of Urca cooling pairs that occur in the neutron star’s outer layers at mass densities below neutron-drip $\rho \lesssim \rho_{\text{drip}} \approx 4 \times 10^{11} \text{ g cm}^{-3}$.

For each odd- A isotope, we calculate the total neutrino luminosity from e^- -capture/ β^- -decay cycles using analytic expressions for the reaction rates (Tsuruta & Cameron, 1970), as outlined in Section 5.1. The ft -values, which measure the transition strength of e^- -captures and β^- -decays, are based on experimental data² when available; otherwise, ft -values are obtained from Table 1 of Singh et al. (1998), using the experimentally determined ground-state spin-parities J^π of the e^- -capture parent and daughter nuclei (Tuli, 2011). This approach to calculating ft -values provides more reliable results than purely theoretical calculations using the quasi particle random phase approximation for the special cases of interest here, where level energies, spins, and parities of all relevant levels are known experimentally. The 15 strongest Urca pairs near the superburst ignition depth are shown in Table 5.3.

We find that Urca cooling is present in all odd- A nuclei studied. In Figure 5.8, Urca pairs are shown relative to the superburst ignition depths constrained from observations between $y \approx 0.5\text{--}3 \times 10^{12} \text{ g cm}^{-2}$ (Cumming et al., 2006). The strongest cooling pairs occur at depths $y \gtrsim 1.1 \times 10^{12} \text{ g cm}^{-2}$. The two strongest cooling pairs are $^{23}\text{Na}\text{--}^{23}\text{Ne}$ and $^{25}\text{Mg}\text{--}^{25}\text{Na}$, which occur near $y \approx 8.6 \times 10^{12} \text{ g cm}^{-2}$ and $y \approx 4.9 \times 10^{12} \text{ g cm}^{-2}$, respectively.

²Evaluated Nuclear Structure Data File (ENSDF) — a computer file of experimental nuclear structure data maintained by the National Nuclear Data Center, Brookhaven National Laboratory (www.nndc.bnl.gov) — as of 11 December 2015

Table 5.3: Urca pairs active in the neutron star ocean.

Urca pair, ${}^A_Z X$	$ Q_{\text{EC}} $ [MeV]	y_{12} ¹	L_{34} ²
${}^{81}_{35}\text{Br} - {}^{81}_{34}\text{Se}$	1.59	0.1	0.10
${}^{49}_{22}\text{Ti} - {}^{49}_{21}\text{Sc}$	2.00	0.3	0.12
${}^{65}_{29}\text{Cu} - {}^{65}_{28}\text{Ni}$	2.14	0.4	0.02
${}^{55}_{25}\text{Mn} - {}^{55}_{24}\text{Cr}$	2.60	1.0	1.95
${}^{69}_{30}\text{Zn} - {}^{69}_{29}\text{Cu}$	2.68	1.1	0.78
${}^{57}_{26}\text{Fe}^* - {}^{57}_{25}\text{Mn}$	2.70	1.2	3.45
${}^{67}_{29}\text{Cu} - {}^{67}_{28}\text{Ni}$	3.58	3.7	15.4
${}^{63}_{28}\text{Ni}^* - {}^{63}_{27}\text{Co}$	3.66	4.1	14.9
${}^{25}_{12}\text{Mg} - {}^{25}_{11}\text{Na}$	3.83	4.9	20.3
${}^{81}_{34}\text{Se} - {}^{81}_{33}\text{As}$	3.86	5.0	4.54
${}^{73}_{31}\text{Ga} - {}^{73}_{30}\text{Zn}$	4.11	6.5	8.61
${}^{79}_{33}\text{As} - {}^{79}_{32}\text{Ge}$	4.11	6.5	7.68
${}^{23}_{11}\text{Na} - {}^{23}_{10}\text{Ne}$	4.38	8.4	42.1
${}^{101}_{42}\text{Mo}^* - {}^{101}_{41}\text{Nb}$	4.63	11	8.92
${}^{57}_{25}\text{Mn} - {}^{57}_{24}\text{Cr}$	4.96	14	17.8

¹ $y_{12} \equiv y/(10^{12} \text{ g cm}^{-2})$, calculated with $g_{14} = 1.85$.

² Calculated with experimental ft -values when possible.

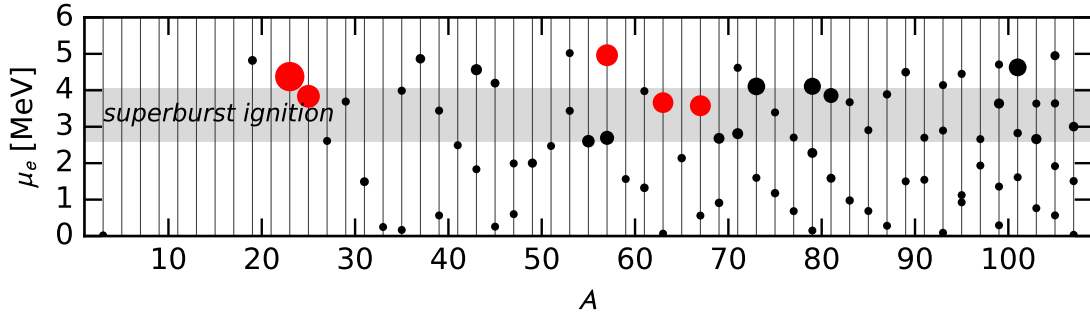


Figure 5.8: Depth of Urca cooling pairs of a given mass number A . The size of data points corresponds to the coefficient L_{34} given in Equation 5.8, and can be found in Table 1. Urca pairs with $L_{34} \geq 10$ are colored in red. The gray band indicates empirical constraints on the superburst ignition depth between $y_{\text{ign}} \approx 0.5\text{--}3 \times 10^{12} \text{ g cm}^{-2}$ (Cumming et al., 2006).

5.3.1 Observational Signatures

Many Urca pairs appear in the neutron star ocean (Deibel et al., 2016), although they have lower neutrino luminosities than deeper pairs in the crust. These pairs cool the ocean by neutrino emission near the depths inferred for superburst ignition. In this section, we model the ocean temperature with and without Urca pairs to determine their impact on unstable carbon ignition. The flux entering the ocean from the crust is $F = Q_b \dot{m}$. The flux entering the ocean must be higher than supplied by crustal heating for models to ignite at observed depths. For example, as shown in Cumming et al. (2006), there must be $Q_b \approx 0.25(\dot{m}/0.3 \dot{m}_{\text{Edd}})^{-1}$ for carbon ignition at $y = 10^{12} \text{ g cm}^{-2}$.

We calculate the neutron star ocean's thermal evolution using the open source code dStar (Brown, 2015) which solves the general relativistic heat diffusion equation using the MESA numerical library (Paxton et al., 2011, 2013, 2015). The model has a neutron star mass $M = 1.4 M_{\odot}$, neutron star radius $R = 10 \text{ km}$, and core temperature $T_{\text{core}} = 3 \times 10^7 \text{ K}$. The neutron star accretes until the ocean temperature reaches steady state.

Runaway thermonuclear burning of carbon occurs when the local heating rate from carbon fusion ϵ_{C} and the local cooling rate ϵ_{cool} satisfy the condition $d\epsilon_{\text{C}}/dT > d\epsilon_{\text{cool}}/dT$. For the local heating rate from carbon burning, we use the $^{12}\text{C}+^{12}\text{C}$ reaction rate given by Caughlan & Fowler (1988) with screening by Ogata et al. (1993). The local cooling rate is given by $\epsilon_{\text{cool}} = \rho KT/y^2$ (Fujimoto et al., 1981). The unstable carbon ignition curve in an iron ocean with $X_{\text{C}} = 0.2$ is shown in Figure 5.9.

We run a neutron star model with a local accretion rate $\dot{m} = 0.3 \dot{m}_{\text{Edd}}$, where $\dot{m}_{\text{Edd}} \approx 8.8 \times 10^4 \text{ g cm}^{-2} \text{ s}^{-1}$. The heat flux entering the ocean from the crust is $F = Q_b \dot{m}$ at the location of the ocean-crust boundary where $\Gamma = 175$ (Farouki & Hamaguchi, 1993). We use $Q_b = 0.25 \text{ MeV}$ per accreted nucleon to give ignition at $y = 10^{12} \text{ g cm}^{-2}$ following the relation $Q_b \approx$

$0.25(\dot{m}/0.3 \dot{m}_{\text{Edd}})^{-1}$ (Cumming et al., 2006).

In Figure 5.9 we show the ocean temperature profile with and without Urca pairs for our model. In an ocean without Urca pairs, superburst ignition occurs at $y_{\text{ign}} \approx 1.0 \times 10^{12} \text{ g cm}^{-2}$. When Urca pairs are located at $y > y_{\text{ign}}$ at $y = 1.2 \times 10^{13} \text{ g cm}^{-2}$ the superburst ignition depth increases (see panel (a) of Figure 5.9). For an Urca pair with $L_{34} = 10$ ($L_{34} = 100$) the superburst ignites at a column $y = 1.2 \times 10^{12} \text{ g cm}^{-2}$ ($y = 1.2 \times 10^{12} \text{ g cm}^{-2}$).

When Urca pairs are located at $y < y_{\text{ign}}$ the superburst ignition depth increases. In panel (c) of Figure 5.9, are ocean temperature profiles for an Urca shell located at $y = 1.2 \times 10^{10} \text{ g cm}^{-2}$. For Urca pairs with $X \cdot L_{34} = 10$ ($X \cdot L_{34} = 100$) the superburst ignites at a column $y_{\text{ign}} = 1.1 \times 10^{12} \text{ g cm}^{-2}$ ($y_{\text{ign}} = 1.9 \times 10^{12} \text{ g cm}^{-2}$).

To determine if cooling from ocean Urca pairs may alter the cooling superburst light curve, we model superburst cooling following the approach of Cumming & Macbeth (2004). In this approach, unstable carbon burning deposits heat at the carbon ignition depth on a timescale shorter than a thermal diffusion time. The heat deposition raises the oceans temperature to $T \gg 10^9 \text{ K}$ and sets a steep temperature profile that acts as the initial temperature profile for the subsequent cooling superburst light curve. The average energy input from superburst burning is $E_{18} \equiv E_{\text{nuc}}/(10^{18} \text{ ergs g}^{-1})$ and superburst cooling light curves are typically well fit with $E_{18} \approx 0.2$. The initial temperature profile is a power law $T \propto y^\alpha$ in column depth and column depth can be approximated as $y = P/g \approx 3.6 \times 10^{12} \text{ g cm}^{-2} \rho_9^{4/3} (Y_e/0.4)^{4/3}$, where $\rho_9 \equiv \rho/(10^9 \text{ g cm}^{-3})$, and superbursts are typically well fit with $\alpha \approx 0.25$.

We examine superburst cooling light curves for two ignition depths $y_{\text{ign}} = 3.6 \times 10^{11}$ and $3.6 \times 10^{12} \text{ g cm}^{-2}$. We include ocean Urca pairs at $y = 0.4 y_{\text{ign}}$ with the values $X \cdot L_{34} = 100, 1000$ for both ignition depths. The results of these models can be seen in Figure 5.10. Urca cooling in the ocean only begins to affect the cooling light curve when $X \cdot L_{34} \gtrsim 100$, when the neutrino

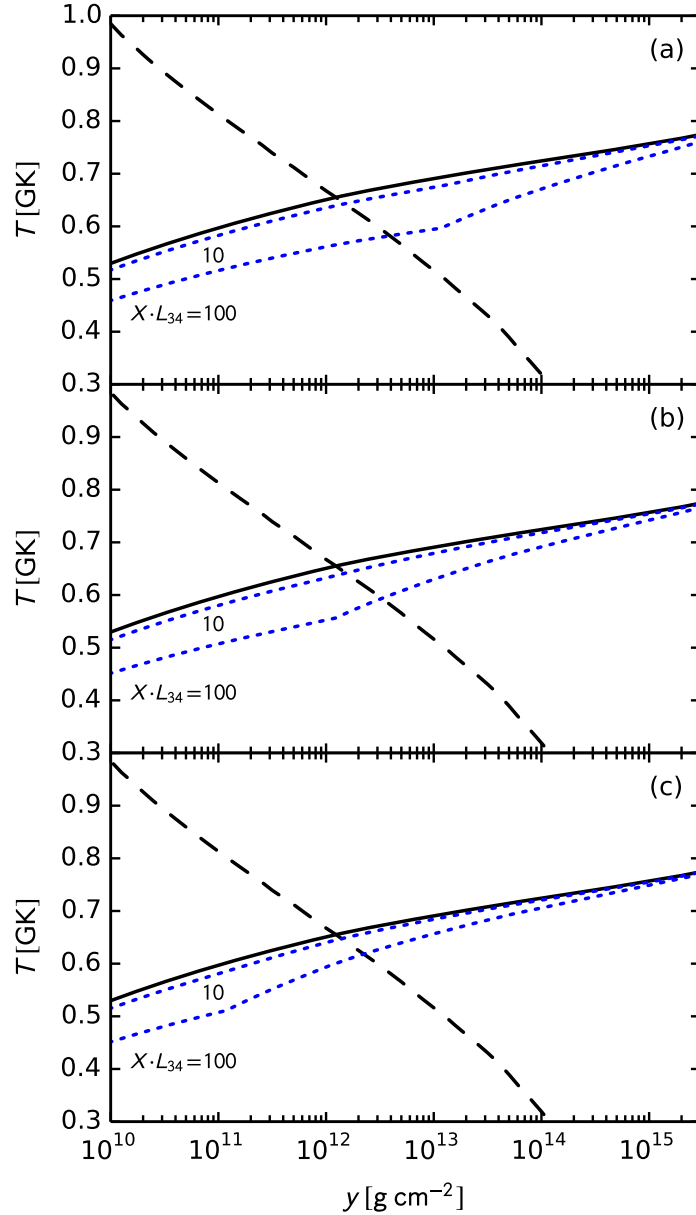


Figure 5.9: Temperature in the ocean as a function of column depth for a neutron star model with: $\dot{m} = 0.3 \dot{m}_{\text{Edd}}$, $M = 1.4 M_{\odot}$, $R = 10 \text{ km}$, and core temperature $T_{\text{core}} = 3 \times 10^7 \text{ K}$. The dashed-black curves indicate the ignition of unstable carbon burning in a mixed iron-carbon ocean with $X_{\text{Fe}} = 0.8$ and $X_{\text{C}} = 0.2$. The solid-black curves indicate ocean's without Urca cooling layers. In each panel, the lower dotted-blue curve is for $L_{34} = 100$ and the upper dotted-blue curve is for $L_{34} = 10$, for Urca pairs located at: *Panel (a)*: $y = 1.2 \times 10^{13} \text{ g cm}^{-2}$, *Panel (b)*: $y = 1.2 \times 10^{12} \text{ g cm}^{-2}$, and *Panel (c)*: $y = 1.2 \times 10^{10} \text{ g cm}^{-2}$.

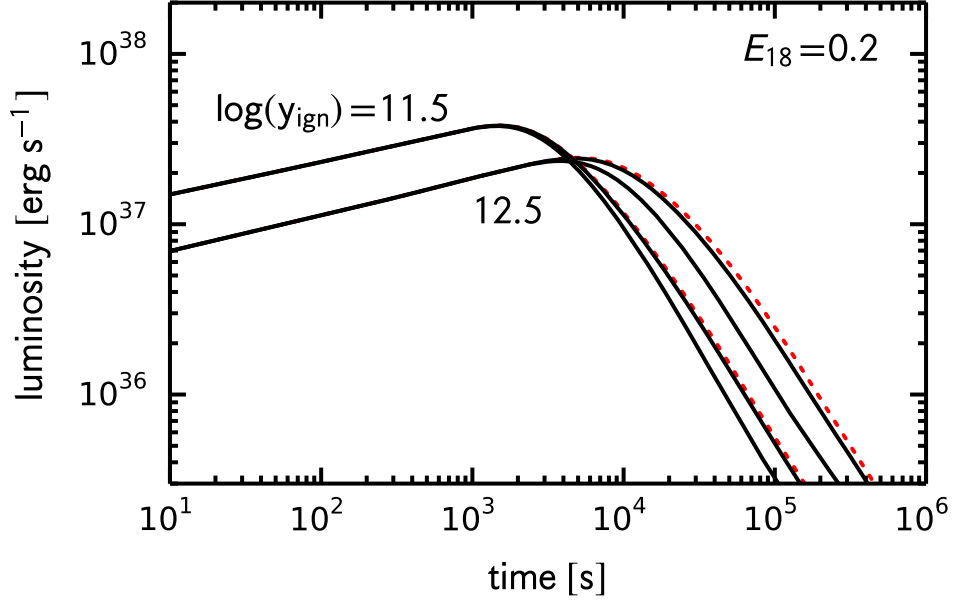


Figure 5.10: Cooling light curves for superbursts with $E_{18} = 0.2$, $\alpha = 0.25$, $g_{14} = 1.6$, and ignition depths $y_{\text{ign}} = 3.2 \times 10^{11} \text{ g cm}^{-2}$ and $y_{\text{ign}} = 3.2 \times 10^{12} \text{ g cm}^{-2}$. The red dotted curves are models without Urca cooling. The solid curves are for a cooling source at $y = 0.4 y_{\text{ign}}$ with $X \cdot L_{34} = 100, 1000$.

luminosity from the Urca pair L_ν becomes comparable to the superburst peak luminosity L_{peak} . At realistic abundances of ocean pairs from X-ray burst and superburst ashes, however, all ocean pairs at these depths have $X \cdot L_{34} \ll 1$ and $L_\nu \ll L_{\text{peak}}$. Therefore, we predict that ocean Urca pairs do not noticeably change superburst cooling light curves.

At large enough abundances ocean Urca pairs have the potential to cool the ocean and increase carbon ignition depths. At the abundances calculated from X-ray burst and superburst nuclear burning (Schatz et al., 2014), however, ocean pairs have weak neutrino luminosities ($X \cdot L_{34} \ll 1$) and do not impact carbon ignition depths. Furthermore, the neutrino luminosities of ocean Urca pairs located at $y \lesssim y_{\text{ign}}$ are too weak to cause an early decline of the superburst light curve. That is, ocean pairs have no effect on the cooling light curve because their neutrino luminosities are small relative to the superburst peak luminosity ($L_\nu \ll L_{\text{peak}}$) even in the hot post-superburst ocean near $T \gtrsim 10^9 \text{ K}$.

Our results suggest that the cooling thermal component of the February 2001 superburst in 4U 1636-536 (Wijnands, 2001; Strohmayer & Markwardt, 2002; Keek et al., 2014a,b) is likely not caused by Urca cooling in the ocean. The cooling light curve declines much faster after the superburst peak than model predictions (with uncertainties about the spectral model used to fit the data, see discussion in Keek et al. 2015). Because the light curve declines after the superburst peak, Urca cooling would need to be near the carbon ignition depth to explain the cooling trend (Keek et al., 2015). For the ignition depth near that of the superburst in 4U 1636-536 ($y_{\text{ign}} \approx 2 \times 10^{11} \text{ g cm}^{-2}$), only Urca cooling pairs present at depths $y \lesssim y_{\text{ign}}$ will impact cooling predictions; however, these ocean pairs are typically weak with $X \cdot L_{34} \ll 1$ and do not effect cooling light curve predictions. Indeed, Urca cooling in the ocean only marginally effects light curve predictions even for $X \cdot L_{34} = 1000$, as can be seen in Figure 5.10.

The shallow ignition depth in 4U 1636-536 near $y_{\text{ign}} \approx 2 \times 10^{11} \text{ g cm}^{-2}$ (Keek et al., 2015) provides constraints on the strength of extra heating and the composition of the crust in this source. A shallow heating source $Q_{\text{shallow}} \approx 9 \text{ MeV}$ per accreted nucleon is the minimum strength required to ignite carbon at this depth in a crust composed of X-ray burst ashes; if composed of superburst ashes the minimum heating strength is $Q_{\text{shallow}} \approx 15 \text{ MeV}$ per accreted nucleon. A weaker shallow heat source is consistent with neutron star transients that have similar accretion rates between $\dot{m} \sim 0.1\text{--}0.3 \dot{m}_{\text{Edd}}$, for instance MXB 1659-29 requires $\approx 1 \text{ MeV}$ per accreted nucleon (Brown & Cumming, 2009). Moreover, superburst ignition models find that several type-I X-ray bursts occur during the intervals between the more energetic superbursts (Keek et al., 2012). It is likely that the crust in 4U 1636-536 is composed primarily of X-ray burst ashes, which accumulate in the crust over the course of $\sim 100\text{--}1000$ years in the more frequent type-I X-ray bursts, and cooling from Urca pairs in these ashes prevails over cooling from pairs in the less abundant superburst ashes.

By contrast, extra heating may be deposited shallower than most crust Urca pairs $y \lesssim 2 \times$

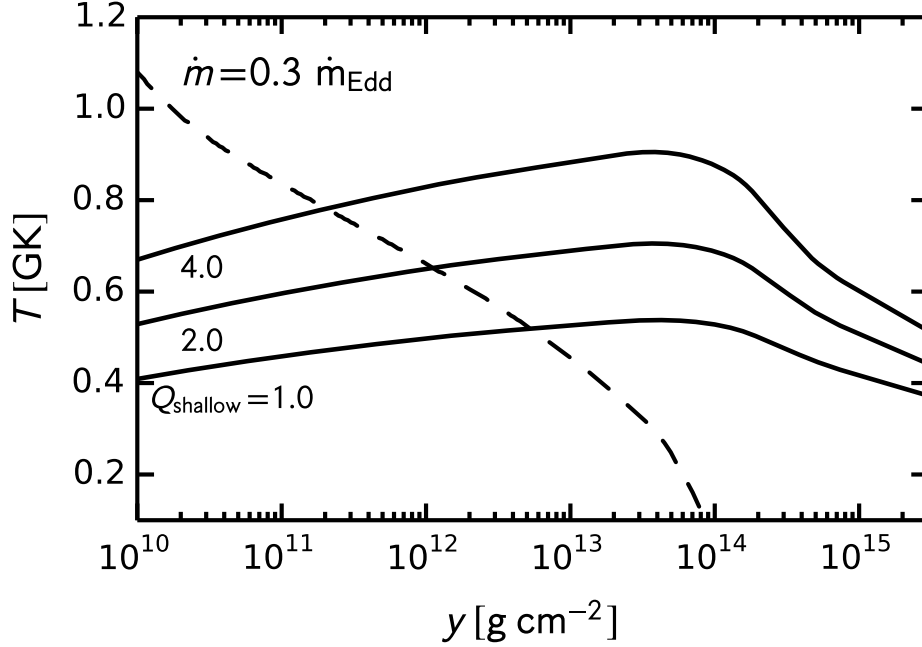


Figure 5.11: Steady state ocean temperature as a function of column depth for a neutron star model with: $\dot{m} = 0.3 \dot{m}_{\text{Edd}}$, $M = 1.4 M_{\odot}$, $R = 10 \text{ km}$, and core temperature $T_{\text{core}} = 3 \times 10^7 \text{ K}$. Solid black curves are steady state temperature profiles for the heating strengths $Q_{\text{shallow}} = 1, 2, 4$. The dashed black curve indicates the ignition of unstable carbon burning in a mixed iron-carbon ocean with $X_{\text{Fe}} = 0.8$ and $X_{\text{C}} = 0.2$.

$10^{14} \text{ g cm}^{-2}$ as is the case in neutron star transients with extra shallow heating; for example, KS 1731-260 and MXB 1659-29 (Brown & Cumming, 2009), and MAXI J0556-332 (Deibel et al., 2015). When deposited at shallower depths, an extra heating strength of $Q_{\text{shallow}} \approx 4 \text{ MeV}$ per accreted nucleon is required to have carbon ignition at depths consistent with the superburst ignition depth in 4U 1636-536, as can be seen in Figure 5.11. In this case, no constraints on crust composition are possible because crust Urca pairs do not alter the temperature in the superburst ignition region. It may be interesting to search for transients that show superbursts during an accretion outburst because the quiescent cooling may potentially indicate the existence of extra heating and its depth. A comparison of the strength and depth of extra heating with the inferred superburst ignition depth will then allow constraints on the crust composition.

The nuclear properties of neutron-rich nuclei are important input for determining the strength

of Urca cooling. Although the Q_{EC} values for nuclei in the ocean are determined from mass measurements to within $\approx 1\%$ (Audi et al., 2012), ft -values and excited state energies are more uncertain. Shell model calculations of all odd- A nuclei in rp -process burning ashes are needed to determine excited state energies and transition strengths to higher accuracy. Furthermore, experimentally determined ft -values and mass measurements of neutron-rich nuclei, for instance at the *Facility for Rare-Isotope Beams* (FRIB), will allow more accurate determinations of Urca pair neutrino luminosities and thereby improve constraints on the interior of superbursting neutron stars.

Chapter 6

Conclusion

This dissertation explores the neutron star interior by reconciling numerical models of the neutron star's outer layers with neutron star observations. In particular, observations of magnetar giant flares and cooling neutron star transients can be used to reveal the properties of dense matter in the neutron star interior that would otherwise be difficult to observe in a terrestrial laboratory. We build a numerical model of the neutron star's outer layers to simulate phenomena in these layers. We then model and analyze a variety of neutron star observations to draw new constraints relevant for nuclear theory and future astrophysical modeling of neutron stars.

In Chapter 2, we outline the current understanding of the microphysics of the neutron star's outermost layers. This numerical model is the foundation for all subsequent investigations of the interior physics. The model uses theoretical mass models that are fit to experimental nuclear data to compute the equilibrium composition of the neutron star's ocean and crust. The composition is needed to compute oscillation modes of the crust in Chapter 3. Because the composition and low-density equation of state set the thermal transport properties of the outer layers, our model can then be used to investigate the thermal evolution of neutron star transients in Chapter 4.

In Chapter 3, we examined crust oscillation modes in highly magnetized neutron stars by adding a magnetic field to our numerical model of the neutron star crust. The frequencies of crust torsional oscillations are a compelling match to observed quasi-periodic oscillations in the tails of magnetar giant flares. Crust oscillation frequencies are uniquely set by the magnetar's mass and radius, as well as the crust composition. Only one mass and radius combination can produce

the observed oscillation frequencies in a given giant flare. Furthermore, if observed quasi-periodic oscillations are indeed oscillating crust modes, then models of crust oscillations may reveal the properties of the densest regions of the neutron star’s crust near the crust-core transition—a density regime where constraints on the nuclear symmetry energy are difficult to obtain.

In Chapter 4, we investigate the quiescent light curves of neutron star X-ray transients. Though some transients are known to require extra heating during their accretion outbursts to match observed quiescent temperatures, such as KS 1731-260 and MXB 1659-29 (Brown & Cumming, 2009), we find that the hottest transient MAXI J0556-332 requires a surprisingly large amount of heat deposition during outburst. The quiescent temperature of MAXI J0556-332 requires $\gtrsim 6$ MeV per accreted nucleon of heat be deposited during outburst; a factor of 6 larger than previously observed shallow heating in other sources. Interestingly, superburst models require extra heating in the ocean and shallow crust to provide a heat flux into the envelope sufficient to ignite carbon at depths consistent with observed light curves (Keek et al., 2008; in’t Zand et al., 2012; Zamfir et al., 2014). Furthermore, the extra heating is required for superburst models to match observed superburst recurrence times (Cumming & Bildsten, 2001; Strohmayer & Brown, 2002b). The source of the extra heating, however, remains unknown, and should be the focus of future work. A plausible source of the extra heating may be the rotational energy reservoir in the accretion flow. The Keplerian energy of the accretion flow is ~ 80 MeV per accreted nucleon (at the inner-most stable circular orbit) and the viscous dissipation of rotational energy may occur in an accreted spreading boundary layer (Inogamov & Sunyaev, 1999, 2010; Philippov et al., 2016).

The late time cooling of neutron star transients should also be investigated further. In Section 4.4, we discuss the late time cooling observations of the neutron star transient MXB 1659-29. The neutron star appears to resume cooling around ≈ 2500 d which may be indicative of a layer of normal neutrons with a long thermal time that forms as a consequence of the low thermal conduc-

tivity of nuclear pasta. The normal neutron layer requires that the 1S_0 neutron singlet pairing gap closes in the crust before the crust-core transition. As a result, constraints on the neutron singlet pairing gap model are possible through fitting various gap models to the late time light curve of MXB 1659-29. In particular, the transition density to normal neutrons can be determined, though the late time cooling will be insensitive to the energy of the gap itself. In a similar manner, theoretical singlet pairing gap models can be examined to determine which of the existing models best fits the late time cooling observations.

We also outline an observational test to answer an open question in neutron star transient observations (Section 4.3). Observed quasi-periodic oscillations in the transient neutron star Z-sources, such as Sco X-1, are of unknown origin. Curiously, some observed frequencies are close to the neutron star ocean's thermal g -mode frequencies. We show that as the ocean heats up during an accretion outburst the ocean's thermal g -mode frequencies increase and when accretion halts, the predicted g -mode frequencies decrease as the ocean cools. Furthermore, we predict that observed oscillation frequencies should be larger in the hottest neutron star transients that require anomalous shallow heating, for example, MAXI J0556-332. These predictions can be tested by further X-ray observations of neutron star Z-sources along the normal branch.

In Chapter 5 we discuss the recent discovery of Urca cooling in nuclear reaction network calculations of the accreted crust. Schatz et al. (2014) found nuclear pairs that undergo cycles of e^- -capture / β^- -decay appear in accreted material compressed into the neutron star's crust. Urca cycling pairs cool the neutron star crust and can counteract heating from accretion-driven nuclear reactions. We find that Urca cooling impacts quiescent light curve predictions of neutron star transients (Deibel et al., 2015; Meisel & Deibel, 2017), and Urca cooling is unlikely to be present in MAXI J0556-332. We expand upon Schatz et al. (2014) and find that Urca cycling nuclei pairs appear in the ocean at lower densities as well (Deibel et al., 2016). Although it is unlikely that

ocean Urca pairs cool the ocean sufficiently to alter carbon ignition depths in superbursts, we find that Urca pairs located in the deeper crust potentially alter ignition depths. Urca pairs in the crust prevent crustal heating from entering the overlying ocean and carbon ignition occurs deeper than it would otherwise.

APPENDICES

Appendix A: Local Stability of Non-equilibrium Nuclear Reactions

In the inner crust, an compressed nucleus will undergo non-equilibrium reactions in the degenerate electron and quasi-free neutron gases therein. For example, a nucleus with proton number Z and mass number A will undergo an electron capture in an electron gas with chemical potential μ_e , when

$$Z\mu_e > B(Z, A) - Nm_n - Z(m_p + m_e) - B(Z-1, A) + (A-Z+1)m_n + (Z-1)(m_p + m_e) + (Z-1)\mu_e, \quad (1)$$

or

$$\mu_e > B(Z, A) - B(Z-1, A) - \Delta, \quad (2)$$

where $B(Z, A)$ is the binding energy of the nucleus and $\Delta = m_n - m_p - m_e$ is the binding energy of the neutron. The same conditions for other possible reactions are:

$$\beta \text{ decay : } \mu_e > -B(Z, N) + B(Z+1, A) + \Delta \quad (3)$$

$$\text{Neutron capture : } \mu_n < B(Z, A) - B(Z, A+1) \quad (4)$$

$$\text{Neutron emission : } \mu_n > -B(Z, A) + B(Z, A-1) \quad (5)$$

Combining the capture inequalities and the emission inequalities gives,

$$\mu_e + \mu_n < 2B(Z, A) - B(Z-1, A) - B(Z, A+1) + \Delta, \quad (6)$$

$$\mu_e + \mu_n > -2B(Z, A) + B(Z+1, A) + B(Z, A-1) + \Delta, \quad (7)$$

Now combine these inequalities to remove chemical potentials,

$$\frac{1}{4} [B(Z + 1, A) + B(Z, A - 1) + B(Z - 1, A) + B(Z, A + 1)] < B(Z, A) , \quad (8)$$

which looks like the nucleus binding energy has to be larger than the average of the binding energies of the surrounding nuclei in order for the nucleus to be stable against non-equilibrium reactions. This is identically expressed as the condition for local stability,

$$\frac{\partial^2 B}{\partial Z^2} + \frac{\partial^2 B}{\partial A^2} < 0 ; \quad \nabla^2 < 0 . \quad (9)$$

Appendix B: Thermal Diffusion

Here we derive the fully general relativistic thermal evolution equation for the neutron star crust (Equation 2.25) following the approach of Thorne (1977). We begin with Equation (11d) of Thorne (1977),

$$\frac{1}{\mathcal{R}^2} \frac{\partial(L\mathcal{R}^2)}{\partial M} = \varepsilon_{nuc} - \varepsilon_\nu - \frac{1}{\mathcal{R}} \frac{\partial \Pi}{\partial t} + \frac{1}{\mathcal{R}} \frac{P}{\rho^2} \frac{\partial \rho}{\partial t}, \quad (10)$$

where $\mathcal{R} = \exp(\Phi/c^2)$ is the gravitational redshift and Φ is the gravitational potential of the neutron star. the compression term is negligible. Given that $C_p = \partial \Pi / \partial T$ for degenerate matter, Equation 10 can be rewritten as

$$\frac{1}{\mathcal{R}^2} \frac{\partial(L\mathcal{R}^2)}{\partial M} = \varepsilon_{nuc} - \varepsilon_\nu - \frac{1}{\mathcal{R}} \left(C_p \frac{\partial T}{\partial t} \right), \quad (11)$$

The LHS of Equation 11 is found by starting with Equation (11h) of Thorne (1977) ,

$$\frac{\partial \ln T}{\partial M_r} = \nabla_{\text{rad}} \frac{\partial \ln P}{\partial M_r}, \quad (12)$$

and Equation (9a) Thorne (1977) ,

$$\nabla_{\text{rad}} = \frac{3}{64\pi} \frac{\kappa L_r P}{GM_r \sigma T^4} \frac{1}{\mathcal{H} \mathcal{G} \mathcal{V}} + \left(1 - \frac{\varepsilon}{\mathcal{H}} \right), \quad (13)$$

where the correction factors are: \mathcal{H} enthalpy, \mathcal{G} gravitational-acceleration, \mathcal{V} volume, and ε energy.

Plugging Equation 13 into Equation 12 gives

$$\frac{1}{T} \frac{\partial T}{\partial M_r} = \left[\frac{3}{64\pi} \frac{\kappa L_r P}{GM_r \sigma T^4} \frac{1}{\mathcal{H} \mathcal{G} \mathcal{V}} + \left(1 - \frac{\varepsilon}{\mathcal{H}} \right) \right] \frac{\partial \ln P}{\partial M_r}. \quad (14)$$

Using Equation (11i) from Thorne (1977) we have the relation

$$\frac{\partial \ln P}{\partial M_r} = \frac{1}{P} \frac{\partial P}{\partial M_r} = \frac{1}{P} \left(-\frac{GM_r}{4\pi r^4} \mathcal{G}\mathcal{H}\mathcal{V} \right). \quad (15)$$

Inserting Equation 15 into Equation 14 and noting that $\mathcal{H} - \varepsilon = P/(\rho c^2)$, gives

$$\frac{1}{T} \frac{\partial T}{\partial M_r} = -\frac{3}{64\pi} \frac{\kappa L_r}{acT^4} \frac{1}{4\pi r^4} - \frac{GM_r \mathcal{G}\mathcal{V}}{4\pi r^4 \rho c^2}, \quad (16)$$

and using the relation

$$\frac{GM_r \mathcal{G}\mathcal{V}}{4\pi r^4 \rho c^2} = \frac{\partial \Phi / c^2}{\partial M_r}, \quad (17)$$

we can express Equation 16 as

$$\frac{1}{T} \frac{\partial T}{\partial M_r} + \frac{1}{c^2} \frac{\partial \Phi}{\partial M_r} = -\frac{3}{64\pi} \frac{\kappa L_r}{acT^4} \frac{1}{4\pi r^4}. \quad (18)$$

Multiplying by $4T^4$ and solving for L_r gives,

$$L_r = -\frac{4ac}{3\kappa} (4\pi r^2)^2 e^{-4\Phi} \frac{\partial}{\partial M_r} (e^{4\Phi} T^4). \quad (19)$$

Multiplying both sides by $\frac{1}{\mathcal{R}^2} \frac{\partial}{\partial M_r} \mathcal{R}^2$,

$$\frac{1}{\mathcal{R}^2} \frac{\partial (L_r \mathcal{R}^2)}{\partial M_r} = \frac{1}{\mathcal{R}^2} \frac{\partial}{\partial M_r} \left\{ -\mathcal{R}^2 \frac{4ac}{3\kappa} (4\pi r^2)^2 e^{-4\Phi} \frac{\partial}{\partial M_r} (e^{4\Phi} T^4) \right\} \quad (20)$$

and we have recovered the LHS of Equation 11. Plugging Equation 20 into Equation 11 and

simplifying, gives

$$\mathcal{R}^{-1}C_p \frac{dT}{dt} = -\frac{1}{\mathcal{R}^2} \frac{\partial}{\partial M_r} \left\{ -\mathcal{R}^2 \frac{ac}{3\kappa} (4\pi r^2)^2 e^{-4\Phi} \frac{d}{dM_r} (e^{4\Phi} T^4) \right\} + \varepsilon_{nuc} - \varepsilon_\nu, \quad (21)$$

The derivative could also be done with respect to the radial coordinate because

$$\frac{\partial r}{\partial M_r} = (4\pi r^2 \rho \mathcal{V})^{-1}, \quad (22)$$

and it can be easily shown that the diffusion equation in terms of the radial coordinate is

$$\frac{dT}{dt} = \frac{1}{C(r, T)} \left(\frac{\partial}{\partial r} \left\{ \bar{K}(r, T) \frac{\partial}{\partial r} (\mathcal{R}^4 T^4) \right\} + \varepsilon_{nuc} - \varepsilon_\nu \right), \quad (23)$$

where

$$C(r, T) = \frac{3C_p r^2 \mathcal{V} \mathcal{R}}{ac}, \quad (24)$$

and

$$\bar{K}(r, T) = \frac{r^2}{\kappa \mathcal{R}^2}. \quad (25)$$

Appendix C: Axial Perturbations

Here we formulate a version of the torsional perturbation equation appropriate for a highly magnetized neutron star. The ad-hoc form of the perturbation equation will include general relativistic corrections appropriate for the large neutron star gravity and a finite Alfvén velocity to account for a large magnetic field in a magnetar. We begin by following the derivation of axial perturbations from Samuelsson & Andersson (2007) in the Cowling approximation (Cowling, 1941) (i.e., we ignore changes in the gravitational potential over the thin crust). The perturbation equation is

$$\xi'' + \frac{d}{dr} \left\{ \ln \left[r^4 e^{\nu-\lambda} (\varepsilon + p_t) v_r^2 \right] \right\} \xi' + \frac{e^{2\lambda}}{v_r^2} \left[e^{-2\nu} \omega^2 - \frac{v_t^2 (\ell - 1) (\ell + 2)}{r^2} \right] \xi = 0, \quad (26)$$

where ε is the energy density, ρ is the rest mass energy density, r is the radial coordinate, ω is the angular frequency, and $e^{2\lambda} \approx e^{-2\nu} \approx (1 - 2M/(Rc^2))^{-1}$ in the thin crust. Note that the argument of the logarithm can be made unitless with the appropriate combination of \hbar and c . We will take the isotropic limit $p_t = p$ and $v_r^2 = v_t^2 = v_s^2 = \mu/\rho$. Evaluating the first coefficient,

$$\begin{aligned} \frac{d}{dr} \left\{ \ln \left[r^4 e^{\nu-\lambda} (\varepsilon + p_t) v_r^2 \right] \right\} &= \left[r^4 e^{\nu-\lambda} (\varepsilon + p) v_s^2 \right]^{-1} \left[\frac{d}{dr} \{ r^4 \} (e^{\nu-\lambda} (\varepsilon + p) v_s^2) \right. \\ &+ \frac{d}{dr} \{ e^{\nu-\lambda} \} (r^4 (\varepsilon + p) v_s^2) + \frac{d}{dr} \{ \varepsilon + p \} (r^4 e^{\nu-\lambda} v_s^2) + \left. \frac{d}{dr} \{ v_s^2 \} (r^4 e^{\nu-\lambda} (\varepsilon + p)) \right], \end{aligned} \quad (27)$$

where the result is written to illustrate clearly that the product rule is being used on four functions.

Evaluating each term individually,

$$\begin{aligned} \frac{d}{dr} \{ r^4 \} &= 4r^3, \\ \frac{d}{dr} \{ e^{\nu-\lambda} \} &= \frac{d}{dr} \left\{ 1 - \frac{2M(r)}{r} \right\} = -2 \left(\frac{dM(r)}{dr} \frac{1}{r} - \frac{M(r)}{r^2} \right) = \frac{2}{r} \left(\frac{M(r)}{r} - \frac{dM(r)}{dr} \right), \\ \frac{d}{dr} \{ \varepsilon + p \} &= \frac{d\varepsilon}{dr} + \frac{dp}{dr}, \end{aligned}$$

$$\frac{d}{dr} \left\{ v_s^2 \right\} = \frac{d}{dr} \left\{ \frac{\mu}{\rho} \right\} = \frac{d\mu}{dr} \frac{1}{\rho} - \frac{\mu}{\rho^2} \frac{d\rho}{dr} = \frac{1}{\rho} \left(\frac{d\mu}{dr} - v_s^2 \frac{d\rho}{dr} \right),$$

where we assume $dB/dr = 0$, (the magnetic field is not changing with depth in the star). Putting together all of the pieces in the first coefficient,

$$A = \left[r^4 \left(1 - 2 \frac{M(r)}{r} \right) (\varepsilon + p) v_s^2 \right]^{-1} \left[4r^3 (e^{\nu-\lambda} (\varepsilon + p) v_s^2) \right] \quad (28)$$

$$+ \left(\frac{2}{r} \left(\frac{M(r)}{r} - \frac{dM(r)}{dr} \right) \right) (r^4 (\varepsilon + p) v_s^2) + \left(\frac{d\varepsilon}{dr} + \frac{dp}{dr} \right) (r^4 e^{\nu-\lambda} v_s^2) \quad (29)$$

$$+ \left(\frac{1}{\rho} \left(\frac{d\mu}{dr} - v_s^2 \frac{d\rho}{dr} \right) \right) (r^4 e^{\nu-\lambda} (\varepsilon + p)) \quad (30)$$

The differential equation then becomes,

$$\left(1 + \frac{v_A^2}{v_s^2} \right) \xi'' + A \xi' + \left(1 - 2 \frac{M(r)}{r} \right)^{-1} \frac{1}{v_s^2} \left[\left(1 - 2 \frac{M(r)}{r} \right)^{-1} (1 + v_A^2) \omega^2 - \frac{v_s^2 (l-1)(l+2)}{r^2} \right] \xi = 0, \quad (31)$$

$$\left(1 + \frac{v_A^2}{v_s^2} \right) \xi'' + A \xi' + \left\{ \frac{e^{2\lambda}}{v_s^2} \left[e^{2\lambda} (1 + v_A^2) \omega^2 - \frac{v_s^2 (l-1)(l+2)}{r^2} \right] \right\} \xi = 0. \quad (32)$$

This is the expression used in Deibel et al. (2014). The Newtonian expression in Piro (2005) can be recovered in the limit $e^{2\lambda} \rightarrow 1$.

REFERENCES

REFERENCES

- Andersson, N. 1998, *ApJ*, 502, 708
- Andersson, N., Glampedakis, K., Ho, W. C. G., & Espinoza, C. M. 2012, *Physical Review Letters*, 109, 241103
- Andersson, N., Jones, D. I., & Ho, W. C. G. 2014, *MNRAS*, 442, 1786
- Audi, G., Wang, M., Wapastra, A. H., Kondev, F. G., MacCormick, M., Xu, X., & Pfeiffer, B. 2012, *Chinese Physics C*, 36, 2
- Baade, W., & Zwicky, F. 1934, *Proceedings of the National Academy of Science*, 20, 259
- Bahcall, J. N., & Wolf, R. A. 1965, *Physical Review*, 140, 1452
- Bahramian, A., Heinke, C. O., Wijnands, R., & Degenaar, N. 2016, *The Astronomer's Telegram*, 8699
- Baiko, D. A., & Yakovlev, D. G. 1995, *Astronomy Letters*, 21, 702
- . 1996, *Astronomy Letters*, 22, 708
- Barat, C., et al. 1983, *Astron. & Astrophys.*, 126, 400
- Bardeen, J. M., & Petterson, J. A. 1975, *ApJ*, 195, L65
- Baym, G., Bethe, H. A., & Pethick, C. J. 1971a, *Nuclear Physics A*, 175, 225
- Baym, G., & Chin, S. A. 1976, *Nuclear Physics A*, 262, 527
- Baym, G., Pethick, C., & Pines, D. 1969, *Nature*, 224, 673
- Baym, G., Pethick, C., & Sutherland, P. 1971b, *ApJ*, 170, 299
- Belloni, T., Parolin, I., & Casella, P. 2004, *A&A*, 423, 969
- Bildsten, L., & Brown, E. F. 1997, *ApJ*, 477, 897
- Bildsten, L., & Cumming, A. 1998, *ApJ*, 506, 842
- Bildsten, L., & Cutler, C. 1995, *ApJ*, 449, 800
- Bildsten, L., Ushomirsky, G., & Cutler, C. 1996, *ApJ*, 460, 827

- Bisnovatyi-Kogan, G. S., & Chechetkin, V. M. 1979, Soviet Physics Uspekhi, 22, 89
- Brehm, J. J. 1989, Introduction to the Structure of Matter (Wiley)
- Broderick, A., Prakash, M., & Lattimer, J. M. 2000, ApJ, 537, 351
- Brown, B. A. 2013, Physical Review Letters, 111, 232502
- Brown, B. A., Clement, R. R. C., Schatz, H., Volya, A., & Richter, W. A. 2002, Phys. Rev. C, 65, 045802
- Brown, E. F. 2000, ApJ, 531, 988
- . 2015, dStar: Neutron star thermal evolution code, Astrophysics Source Code Library
- Brown, E. F., & Bildsten, L. 1998, ApJ, 496, 915
- Brown, E. F., Bildsten, L., & Chang, P. 2002, ApJ, 574, 920
- Brown, E. F., & Cumming, A. 2009, ApJ, 698, 1020
- Cackett, E. M., Brown, E. F., Cumming, A., Degenaar, N., Fridriksson, J. K., Homan, J., Miller, J. M., & Wijnands, R. 2013, ApJ, 774, 131
- Cackett, E. M., Wijnands, R., Miller, J. M., Brown, E. F., & Degenaar, N. 2008, ApJ, 687, L87
- Casella, P., Belloni, T., & Stella, L. 2006, A&A, 446, 579
- Caughlan, G. R., & Fowler, W. A. 1988, Atomic Data and Nuclear Data Tables, 40, 283
- Chabanat, E., Bonche, P., Haensel, P., Meyer, J., & Schaeffer, R. 1995, Phys. Scripta, T56, 231
- Chadwick, J. 1932, Nature, 129, 312
- Chamel, N. 2005, Nuclear Physics A, 747, 109
- . 2012, Phys. Rev. C, 85, 035801
- Chamel, N. 2013, Phys. Rev. Lett., 110, 011101
- Chamel, N., Page, D., & Reddy, S. 2013a, Phys. Rev. C, 87, 035803
- . 2013b, Phys. Rev. C, 87, 035803
- Chen, J. M. C., Clark, J. W., Davé, R. D., & Khodel, V. V. 1993, Nuclear Physics A, 555, 59

Cooper, R. L., Steiner, A. W., & Brown, E. F. 2009, *ApJ*, 702, 660

Cowling, T. G. 1941, *MNRAS*, 101, 367

Cumming, A., & Bildsten, L. 2001, *ApJ*, 559, L127

Cumming, A., & Macbeth, J. 2004, *ApJ*, 603, L37

Cumming, A., Macbeth, J., in 't Zand, J. J. M., & Page, D. 2006, *ApJ*, 646, 429

Cyburt, R. H., et al. 2010, *ApJS*, 189, 240

Degenaar, N., Brown, E. F., & Wijnands, R. 2011, *MNRAS*, 418, L152

Degenaar, N., & Wijnands, R. 2011, *MNRAS*, 414, L50

Degenaar, N., et al. 2009, *MNRAS*, 396, L26

—. 2013, *ApJ*, 775, 48

—. 2014, *ApJ*, 791, 47

—. 2015, *MNRAS*, 451, 2071

Deibel, A. 2016, *ApJ*, 832, 44

Deibel, A., Cumming, A., Brown, E. F., & Page, D. 2015, *ApJ*, 809, L31

Deibel, A., Cumming, A., Brown, E. F., & Reddy, S. 2017, *ApJ*, 839, 95

Deibel, A., Meisel, Z., Schatz, H., Brown, E. F., & Cumming, A. 2016, *ApJ*, 831, 13

Deibel, A. T., Steiner, A. W., & Brown, E. F. 2014, *Phys. Rev. C*, 90, 025802

Dieperink, A. E. L., & van Isacker, P. 2009, *European Physical Journal A*, 42, 269

Dubus, G., Kern, B., Esin, A. A., Rutledge, R. E., & Martin, C. 2004, *MNRAS*, 347, 1217

Duncan, R. C. 1998, *Astrophys. J. Lett.*, 498, L45

Eichler, D., & Cheng, A. F. 1989, *ApJ*, 336, 360

Farouki, R. T., & Hamaguchi, S. 1993, *Phys. Rev. E*, 47, 4330

Flowers, E., & Itoh, N. 1976, *ApJ*, 206, 218

- Fridriksson, J. K., Homan, J., & Remillard, R. A. 2015, *ApJ*, 809, 52
- Fridriksson, J. K., et al. 2010, *ApJ*, 714, 270
- . 2011, *ApJ*, 736, 162
- Fujimoto, M. Y., Hanawa, T., & Miyaji, S. 1981, *ApJ*, 247, 267
- Gamow, G. 1941, *Physical Review*, 59, 617
- Gamow, G., & Schoenberg, M. 1940, *Physical Review*, 58, 1117
- . 1941, *Physical Review*, 59, 539
- Gandolfi, S., Illarionov, A. Y., Fantoni, S., Pederiva, F., & Schmidt, K. E. 2008, *Physical Review Letters*, 101, 132501
- Gezerlis, A., & Carlson, J. 2010, *Phys. Rev. C*, 81, 025803
- . 2011, ArXiv e-prints
- Giacconi, R., Gursky, H., Paolini, F. R., & Rossi, B. B. 1962, *Physical Review Letters*, 9, 439
- Glampedakis, K., Samuelsson, L., & Andersson, N. 2006, *Mon. Not. Royal Astron. Soc.*, 371, L74
- Gudmundsson, E. H., Pethick, C. J., & Epstein, R. I. 1982, *ApJ*, 259, L19
- . 1983, *ApJ*, 272, 286
- Guillot, S., Servillat, M., Webb, N. A., & Rutledge, R. E. 2013, *ApJ*, 772, 7
- Gupta, S., Brown, E. F., Schatz, H., Möller, P., & Kratz, K.-L. 2007, *ApJ*, 662, 1188
- Gupta, S. S., Kawano, T., & Möller, P. 2008, *Phys. Rev. Lett.*, 101, 231101
- Haensel, P., & Zdunik, J. L. 1990, *A&A*, 227, 431
- . 2003, *A&A*, 404, L33
- . 2008, *A&A*, 480, 459
- Hairer, E., Norsett, S. P., & Wanner, G. 1993, *Solving Ordinary Differential Equations I. Nonstiff problems*, 2nd edn., Springer Series in Computational Mathematics (Springer-Verlag)
- Hashimoto, M., Seki, H., & Yamada, M. 1984, *Progress of Theoretical Physics*, 71, 320

- Hasinger, G., & van der Klis, M. 1989, *A&A*, 225, 79
- Hasinger, G., van der Klis, M., Ebisawa, K., Dotani, T., & Mitsuda, K. 1990, *A&A*, 235, 131
- Heney, L., & L'Ecuyer, J. 1969, *ApJ*, 156, 549
- Hertz, P., Vaughan, B., Wood, K. S., Norris, J. P., Mitsuda, K., Michelson, P. F., & Dotani, T. 1992, *ApJ*, 396, 201
- Hewish, A., Bell, S. J., Pilkington, J. D. H., Scott, P. F., & Collins, R. A. 1968, *Nature*, 217, 709
- Ho, W. C. G., Espinoza, C. M., Antonopoulou, D., & Andersson, N. 2015, *Science Advances*, 1, e1500578
- Homan, J., Fridriksson, J. K., Wijnands, R., Cackett, E. M., Degenaar, N., Linares, M., Lin, D., & Remillard, R. A. 2014, *ApJ*, 795, 131
- Homan, J., Linares, M., van den Berg, M., & Fridriksson, J. 2011, *The Astronomer's Telegram*, 3650, 1
- Homan, J., et al. 2007, *ApJ*, 656, 420
- . 2010, *ApJ*, 719, 201
- Horowitz, C. J., & Berry, D. K. 2008, *Phys. Rev. C*, 78, 035806
- . 2009, *Phys. Rev. C*, 79, 065803
- Horowitz, C. J., Berry, D. K., Briggs, C. M., Caplan, M. E., Cumming, A., & Schneider, A. S. 2015, *Physical Review Letters*, 114, 031102
- Horowitz, C. J., Pérez-García, M. A., Carriere, J., Berry, D. K., & Piekarewicz, J. 2004a, *Phys. Rev. C*, 70, 065806
- Horowitz, C. J., Pérez-García, M. A., & Piekarewicz, J. 2004b, *Phys. Rev. C*, 69, 045804
- Horowitz, C. J., Schneider, A. S., & Berry, D. K. 2010, *Physical Review Letters*, 104, 231101
- Iida, K., & Oyamatsu, K. 2014, *European Physical Journal A*, 50, 42
- Inogamov, N. A., & Sunyaev, R. A. 1999, *Astronomy Letters*, 25, 269
- . 2010, *Astronomy Letters*, 36, 848
- in't Zand, J. J. M., Homan, J., Keek, L., & Palmer, D. M. 2012, *A&A*, 547, A47

Israel, G. L., et al. 2005, *Astrophys. J. Lett.*, 628, L53

Itoh, N., & Kohyama, Y. 1993, *ApJ*, 404, 268

Jin, R., & Kong, A. K. H. 2016, *The Astronomer's Telegram*, 8530

Jonker, P. G., van der Klis, M., Homan, J., Méndez, M., Lewin, W. H. G., Wijnands, R., & Zhang, W. 2002, *MNRAS*, 333, 665

Keek, L., Ballantyne, D. R., Kuulkers, E., & Strohmayer, T. E. 2014a, *ApJ*, 789, 121

—. 2014b, *ApJ*, 797, L23

Keek, L., Cumming, A., Wolf, Z., Ballantyne, D. R., Suleimanov, V. F., Kuulkers, E., & Strohmayer, T. E. 2015, *MNRAS*, 454, 3559

Keek, L., & Heger, A. 2011, *ApJ*, 743, 189

Keek, L., Heger, A., & in't Zand, J. J. M. 2012, *ApJ*, 752, 150

Keek, L., in't Zand, J. J. M., Kuulkers, E., Cumming, A., Brown, E. F., & Suzuki, M. 2008, *A&A*, 479, 177

Kuulkers, E., van der Klis, M., Oosterbroek, T., Asai, K., Dotani, T., van Paradijs, J., & Lewin, W. H. G. 1994, *A&A*, 289, 795

Lai, D., & Shapiro, S. L. 1991, *Astrophys. J.*, 383, 745

Lau, K. Y. 2012, PhD thesis, Michigan State University

Lee, U. 2014, *MNRAS*, 442, 3037

Lense, J., & Thirring, H. 1918, *Physikalische Zeitschrift*, 19, 156

Levin, Y. 2006, *Mon. Not. Royal Astron. Soc.*, 368, L35

Lewin, W. H. G., & van der Klis, M. 2006, *Compact Stellar X-ray Sources*

Lin, D., Remillard, R. A., & Homan, J. 2009, *ApJ*, 696, 1257

Link, B. 2012, *Mon. Not. Royal Astron. Soc.*, 422, 1640

Mahmoodifar, S., & Strohmayer, T. 2013, *ApJ*, 773, 140

Maruyama, T., Niita, K., Oyamatsu, K., Maruyama, T., Chiba, S., & Iwamoto, A. 1998, *Phys. Rev. C*, 57, 655

Matsumura, T., et al. 2011, *The Astronomer's Telegram*, 3102, 1

McDermott, P. N., van Horn, H. M., & Hansen, C. J. 1988, *ApJ*, 325, 725

McDermott, P. N., van Horn, H. M., & Scholl, J. F. 1983, *ApJ*, 268, 837

Medin, Z., & Cumming, A. 2011, *ApJ*, 730, 97

—. 2014, *ApJ*, 783, L3

—. 2015, *ApJ*, 802, 29

Meisel, Z., & Deibel, A. 2017, *The Astrophysical Journal*, 837, 73

Meisel, Z., et al. 2015, *Phys. Rev. Lett.*, 115, 162501

Mereghetti, S. 2008, *A&A Rev.*, 15, 225

Migdal, A. B. 1959, *Nucl. Phys. A*, 13, 655

Myers, W. D., & Swiatecki, W. J. 1969, *Annals of Physics*, 55, 395

Nandi, R., Chatterjee, D., & Bandyopadhyay, D. 2012, *arXiv:1207.3247*

Negoro, H., et al. 2015, *The Astronomer's Telegram*, 7943, 1

—. 2016, *The Astronomer's Telegram*, 8513

Newton, W., Gearheart, M., & Li, B.-A. 2013, *ApJS*, 204, 9

Ogata, S., Ichimaru, S., & van Horn, H. M. 1993, *ApJ*, 417, 265

Oppenheimer, J. R., & Volkoff, G. M. 1939, *Physical Review*, 55, 374

Oyamatsu, K., & Iida, K. 2007, *Phys. Rev. C*, 75, 015801

Page, D., & Reddy, S. 2012, *ArXiv e-prints*

—. 2013, *ArXiv e-prints*

Paxton, B., Bildsten, L., Dotter, A., Herwig, F., Lesaffre, P., & Timmes, F. 2011, *ApJS*, 192, 3

Paxton, B., et al. 2013, *ApJS*, 208, 4

—. 2015, *ApJS*, 220, 15

- Pethick, C. J., & Potekhin, A. Y. 1998, *Physics Letters B*, 427, 7
- Pethick, C. J., & Ravenhall, D. G. 1995, *Annual Review of Nuclear and Particle Science*, 45, 429
- Pethick, C. J., Ravenhall, D. G., & Lorenz, C. P. 1995, *Nuclear Physics A*, 584, 675
- Philippov, A. A., Rafikov, R. R., & Stone, J. M. 2016, *ApJ*, 817, 62
- Pines, D., & Alpar, A. 1984, in *Birth and Evolution of Neutron Stars: Issues Raised by Millisecond Pulsars*, ed. S. P. Reynolds & D. R. Stinebring, 161
- Piro, A. L. 2005, *Astrophys. J. Lett.*, 634, L153
- Piro, A. L., & Bildsten, L. 2005, *ApJ*, 619, 1054
- Pons, J. A., Viganò, D., & Rea, N. 2013, *Nature Physics*, 9, 431
- Potekhin, A. Y., Baiko, D. A., Haensel, P., & Yakovlev, D. G. 1999, *A&A*, 346, 345
- Potekhin, A. Y., & Chabrier, G. 2000, *Phys. Rev. E*, 62, 8554
- Potekhin, A. Y., Chabrier, G., & Yakovlev, D. G. 1997, *A&A*, 323, 415
- Press, W. H., Teukolsky, S. A., Vetterling, W. T., & Flannery, B. P. 2007, *Numerical recipes in FORTRAN. The art of scientific computing*, ed. Press, W. H., Teukolsky, S. A., Vetterling, W. T., & Flannery, B. P.
- Priedhorsky, W., Hasinger, G., Lewin, W. H. G., Middleditch, J., Parmar, A., Stella, L., & White, N. 1986, *ApJ*, 306, L91
- Rabi, I. I. 1928, *Zeitschrift fur Physik*, 49, 507
- Ravenhall, D. G., Pethick, C. J., & Wilson, J. R. 1983, *Physical Review Letters*, 50, 2066
- Roggero, A., & Reddy, S. 2016, *ArXiv e-prints*
- Ruderman, M. A. 1968, *Nature*, 218, 1128
- Russell, D. M., & Lewis, F. 2016, *The Astronomer's Telegram*, 8517
- Rutherford, E. 1920, *Nature*, 105, 500
- Rutledge, R. E., Bildsten, L., Brown, E. F., Pavlov, G. G., Zavlin, V. E., & Ushomirsky, G. 2002, *ApJ*, 580, 413
- Samuelsson, L., & Andersson, N. 2007, *Mon. Not. Royal Astron. Soc.*, 374, 256

- Sato, K. 1979, *Progress of Theoretical Physics*, 62, 957
- Schatz, H., Bildsten, L., Cumming, A., & Ouellette, M. 2003, *Nuclear Physics A*, 718, 247
- Schatz, H., Bildsten, L., Cumming, A., & Wiescher, M. 1999, *ApJ*, 524, 1014
- Schatz, H., et al. 1998, *Phys. Rep.*, 294
- . 2001, *Physical Review Letters*, 86, 3471
- . 2014, *Nature*, 505, 62
- Schneider, A. S., Horowitz, C. J., Hughto, J., & Berry, D. K. 2013, *Phys. Rev. C*, 88, 065807
- Schumaker, B. L., & Thorne, K. S. 1983, *Mon. Not. Royal Astron. Soc.*, 203, 457
- Schwartz, S. J., et al. 2005, *ApJ*, 627, L129
- Schwenk, A., Friman, B., & Brown, G. E. 2003, *Nuclear Physics A*, 713, 191
- Shapiro, S. L., & Teukolsky, S. A. 1983, *Black holes, white dwarfs, and neutron stars: The physics of compact objects*
- Shternin, P. S., Yakovlev, D. G., Haensel, P., & Potekhin, A. Y. 2007, *MNRAS*, 382, L43
- Singh, B., Rodriguez, J. L., Wong, S. S. M., & Tuli, J. K. 1998, *Nuclear Data Sheets*, 84, 487
- Skyrme, T. 1959, *Nucl. Phys. A*, 9, 615
- Sotani, H., Iida, K., & Oyamatsu, K. 2015, *ArXiv e-prints*
- Sotani, H., Nakazato, K., Iida, K., & Oyamatsu, K. 2012, *Phys. Rev. Lett.*, 108, 201101
- . 2013a, *MNRAS*, 428, L21
- . 2013b, *MNRAS*, 434, 2060
- Steiner, A. W. 2008, *Phys. Rev. C*, 77, 035805
- . 2012, *Phys. Rev. C*, 85, 055804
- Steiner, A. W., Lattimer, J. M., & Brown, E. F. 2010, *ApJ*, 722, 33
- Steiner, A. W., Lattimer, J. M., & Brown, E. F. 2013, *Astrophys. J. Lett.*, 5
- Steiner, A. W., Prakash, M., Lattimer, J. M., & Ellis, P. J. 2005, *Phys. Rep.*, 411, 325

Steiner, A. W., & Watts, A. L. 2009, *Phys. Rev. Lett.*, 103, 181101

Strohmayer, T., & Mahmoodifar, S. 2014, *ApJ*, 784, 72

Strohmayer, T., van Horn, H. M., Ogata, S., Iyetomi, H., & Ichimaru, S. 1991, *Astrophys. J.*, 375, 679

Strohmayer, T. E., & Brown, E. F. 2002a, *ApJ*, 566, 1045

—. 2002b, *ApJ*, 566, 1045

Strohmayer, T. E., & Markwardt, C. B. 2002, *ApJ*, 577, 337

Strohmayer, T. E., & Watts, A. L. 2005, *Astrophys. J. Lett.*, 632, L111

—. 2006, *Astrophys. J.*, 653, 593

Sugizaki, M., et al. 2013, *PASJ*, 65, 58

Sunyaev, R., & Kwant Team. 1989, *IAU Circ.*, 4839

Taam, R. E., & Picklum, R. E. 1978, *ApJ*, 224, 210

Taam, R. E., Woosley, S. E., & Lamb, D. Q. 1996, *ApJ*, 459, 271

Thompson, C., & Duncan, R. C. 1995, *MNRAS*, 275, 255

Thorne, K. S. 1977, *ApJ*, 212, 825

Titarchuk, L., Seifina, E., & Shrader, C. 2014, *ApJ*, 789, 98

Tolman, R. C. 1934, *Relativity, Thermodynamics, and Cosmology*

Tsuruta, S., & Cameron, A. G. W. 1970, *Ap&SS*, 7, 374

Tuli, J. K. 2011, *Nuclear Data Sheets*

Turlione, A., Aguilera, D. N., & Pons, J. A. 2015, *A&A*, 577, A5

Ushomirsky, G., & Rutledge, R. E. 2001, *MNRAS*, 325, 1157

van der Klis, M. 1989, *ARA&A*, 27, 517

van der Klis, M., Swank, J. H., Zhang, W., Jahoda, K., Morgan, E. H., Lewin, W. H. G., Vaughan, B., & van Paradijs, J. 1996, *ApJ*, 469, L1

- van Hoven, M., & Levin, Y. 2012, MNRAS, 420, 3035
- Ventura, J., & Potekhin, A. 2001, in *The Neutron Star - Black Hole Connection*, ed. C. Kouveliotou, J. Ventura, & E. van den Heuvel, 393
- Wallace, R. K., & Woosley, S. E. 1981, ApJS, 45, 389
- Wambach, J., Ainsworth, T. L., & Pines, D. 1993, Nuclear Physics A, 555, 128
- Watanabe, G., Sato, K., Yasuoka, K., & Ebisuzaki, T. 2003, Phys. Rev. C, 68, 035806
- Watts, A. L., & Strohmayer, T. E. 2006, Astrophys. J. Lett., 637, L117
- Wigner, E. 1934, Physical Review, 46, 1002
- Wijnands, R. 2001, ApJ, 554, L59
- Wijnands, R., Guainazzi, M., van der Klis, M., & Méndez, M. 2002, ApJ, 573, L45
- Wijnands, R., Homan, J., Miller, J. M., & Lewin, W. H. G. 2004, ApJ, 606, L61
- Wijnands, R., Miller, J. M., Markwardt, C., Lewin, W. H. G., & van der Klis, M. 2001, ApJ, 560, L159
- Wijnands, R., Nowak, M., Miller, J. M., Homan, J., Wachter, S., & Lewin, W. H. G. 2003, ApJ, 594, 952
- Wijnands, R., van der Klis, M., & Rijkhorst, E.-J. 1999, ApJ, 512, L39
- Wijnands, R. A. D., van der Klis, M., Kuulkers, E., Asai, K., & Hasinger, G. 1997, A&A, 323, 399
- Woosley, S. E., & Taam, R. E. 1976, Nature, 263, 101
- Woosley, S. E., et al. 2004, ApJS, 151, 75
- Yakovlev, D. G., Kaminker, A. D., Gnedin, O. Y., & Haensel, P. 2001, Phys. Rep., 354, 1
- Yakovlev, D. G., & Urpin, V. A. 1980, Soviet Ast., 24, 303
- Zamfir, M., Cumming, A., & Niquette, C. 2014, MNRAS, 445, 3278